SCUOLA DI DOTTORATO
UNIVERSITÀ DEGLI STUDI DI MILANO-BICOCCA

Department of Earth and Environmental Sciences

PhD program in Chemical, Geological and Environmental Sciences Cycle XXXVIII

Curriculum in Chemical sciences

Derivatization and characterization of polysaccharides to be used for the functionalization of biomaterials

Surname: Nizzolo Name: Sofia

Registration number: 896468

Tutor: Prof. Davide Ballabio

Supervisors: Prof. Laura Russo, Dott.ssa Sabrina Bertini

Coordinator: Prof. Giovanni Malusà

ACADEMIC YEAR 2024/2025

I. LIST OF CONTENTS

II. LIST OF FIGURES

Chapter 1

Chapter 2

Chapter 3

Chapter 4

Chapter 5

III. LIST OF TABLES

Chapter 1

Chapter 2

Chapter 3

Chapter 4

Chapter 5

IV. LIST OF EQUATIONS

V. LIST OF ABBREVATIONS

AFM	Atomic force miscoscopy
APTT	Activated partial thromboplastin time
AT	Antithrombin
ATBD	Antithrombin-binding domain
CD	Circular dichroism
COSY	Correlation spectroscopy
CQAs	Critical quality attributes
CRD	Carbohydrate recognition domain
CS	Chondroitin sulphate
DS	Delivery system
DDS	Drug delivery systems
DLS	Dynamic light scattering
DP	Viscosimeter
DS	Degree of substitution
ECM	Extracellular matrix
ELS	Electrophoretic light scattering
EMA	European medicines agency
ESI	Electrospray ionization
FDA	Food and drug administartion
FID	Free induction decay
FT	Fourier transform
GAG	Glycosaminoglycan
Gal-3	Galectin3

GlcA	Glucuronic acid
GlcAc	N-acetylated glucosamine
GlcN	Glucosamine
GlcNS	N-sulphated glucosamine
GPC	Gel permeation chromatography
HA	Sodium hyaluronate
HIT	Heparin-induced thrombocytopenia
HMBC	Heteronuclear multiple bond correlation
HMW	High molecular weight
HP–SEC	High-Performance size exclusion chromatography
TDA	Triple detector array
HS	Heparan sulphate
HSQC	Heteronuclear single- quantum correlation
HSQC-DEPT	Distortion Enhancement by Polarization Transfer
HYAL	Hyaluronidase
IdoA	Uronic acid
IdoA2S	2-O-sulfo- l-iduronic acid
IP	Inlet pressure
IPF	Idiopathic pulmonary fibrosis
IR	Infrared spectroscopy
ITC	Isothermal titration microcalorimetry
K_D	Dissociation constant
L/P	Ligand/Protein
LAC-NH_2	1-amino-1-deoxy lactitol
LALS	Low-angle light scattering

LBDDS	Lipid based drug delivery system
LMW	Low molecular weight
LMWH	Low molecular weight heparin
LNP	Lipid nanoparticle
LS	Light scattering
MGA	4-O-methyl-glucuronic acid
Mn	Number-average molecular weight
Mp	Peak- average molecular weight or Zeta- average
Mw	Molecular weight
Mz	Molecular weight distribution
NA	Non acetylated
NC	Nanocarrier
NMR	Nuclear magnetic resonance
NS	Non sulphated
NTA	Nanoparticle tracking analysis
OHA	Oligomers of HA
OHY	Oligomers of HYLACH
PCS	Photo correlation spectroscopy
PDA	Photodiode array
PDI	Polydispersity index
PF4	Platelet Factor 4
PLR	Protein/ligand ratios
PPS	Pentosan polysulphate
RALS	Right-angle light scattering
Rg	Radius of gyration

Rh	Radius of hydration
RHAMM	Receptor for Hyaluronate-Mediated Motility
RI	Refractive index
RT	Room temperature
SEC	Size exclusion chromatography
SEM	Scanning transmission microscopy
std dev	Standard deviation
TEM	Transmission electron microscope
TOCSY	Total correlation spectroscopy
TDS	Trisulphated disaccharides
UFH	Unfractionated heparin
UV	Ultraviolet
Xyl	Xylitose
Zp	Zeta potential
δ	Chemical shift
η	Intrinsic viscosity

VI. CONFERENCES

- XIX Convegno-Scuola sulla Chimica dei Carboidrati (XIX CSCC 2025), Pontignano, Italy. Oral presentation: Lipid Nanoparticles: encapsulation of Heparin" S. Nizzolo, M. Gianelli, V. Ravaglia, E. Yates, M. Piazzoni, L. Russo, M. Stagi, F. Zanoni, S. Zanzoni, M. Guerrini, S. Bertini
- UK Proteoglycan meeting (UKPG2025, 2025) manchester UK. Oral presentation: Lipid Nanoparticles: encapsulation of polysaccharides" S. Nizzolo, M. Gianelli, V. Ravaglia, F. Zanoni, E. Yates, M. Stagi, S. Zanzoni, M. Guerrini, S. Bertini
- 31st Symposium on Glycosaminoglycans, (2024) Villa Vigoni, Italy. Oral presentation: Lipid Nanoparticles: encapsulation of polysaccharides" S. Nizzolo, M. Gianelli, V. Ravaglia, F. Zanoni, C.Cosentino, M. Guerrini, S. Bertini
- Elementi di futuro (SCI2024, 2024), Milano, Italy. Oral presentation. "Lipid Nanoparticles: encapsulation of Polysaccharides" S. Nizzolo, M. Gianelli, V. Ravaglia, F. Zanoni, C.Cosentino, M. Guerrini, S. Bertini
- XVIII Convegno-Scuola sulla Chimica dei Carboidrati (XVIII CSCC 2023), Pontignano, Italy. Oral presentation:" Chemical Modifications and structural characterization of Hyaluronic Acid " S.Nizzolo, E. Espostito, S. Elli, T. Sisto, M. Ni, G. Bianchini, M. Guerrini, S. Bertini,
- VLAG 17th Summer Course Glycosciences 2023, Wageningen, Netherlands. Poster: "Gelatin functionalization with sulfated glycosaminoglicans and its characterizations." S.Nizzolo, M. Tilloca, F. Cadamuro, S. Gussoni, L. Russo, S. Bertini

VII. ABSTRACT

This PhD project was funded by the Istituto di Ricerche chimiche e biochimiche G. Ronzoni.

Polysaccharides are a heterogeneous group of naturally occurring polymers which have a wide range of applications, including pharmaceutical, medical device, food and cosmetic fields. In pharmaceutical field they are widely used as anticoagulant, anticancer, anti-inflammatory, antiviral, and antibacterial activities.

For pharmaceutical purpose, polysaccharides can also be covalently linked to other active molecules through a process called conjugation, or modified with functional groups, in order to target selected biological activities, and to improve their pharmacokinetic and pharmacodynamic characteristics.

The structural characterisation of polysaccharides is often challenging due to their complexity which arises from a combination of varying molecular weight and sequence. These properties result from diverse monosaccharide composition, including the formation of cyclic rings, variable linkage positions and potential branching, as well as variations in stereochemistry of the glycosidic linkages. This complexity is further compounded by the occurrence of naturally occurring functional groups, or groups that have been synthetically introduced, for which there is rarely a high degree of regioselectivity.

In biological systems, polysaccharides interact and form complexes with a wide range of other molecules, including proteins, lipids, nucleic acids, as well as other carbohydrates. In animals, these substances fulfil a pivotal function in a multitude of biological processes, including inflammation, cell to cell interactions, cellular growth, angiogenesis and signal transduction. Their ability to interact, and the extent of the selectivity of these interactions, can nevertheless be influenced by attempting to control some of these structural variables. This provides the opportunity of selecting or introducing improved characteristics, or equally, eliminating or minimising those properties or activities that are unwanted or undesirable. While polysaccharides are already established in many industrial, pharmaceutical and medical fields, their diversity and the vast extent of their derivatives, represent a huge reservoir of potentially active, but as yet largely unexplored, structures for future applications. This thesis sets out to investigate potential routes by which some of these potential activities might be achieved.

Sodium hyaluronate (HA) is a naturally occurring, linear, anionic polysaccharide belonging to the glycosaminoglycan (GAG) family. It is composed of repeating disaccharide units of D-glucuronic acid and N-acetylglucosamine linked via β(1,4) and β(1,3) glycosidic bonds. Its molecular weight (Mw) can reach up to 10^7 Da, and it exhibits both structural and hydration functions, owing to its ability to form water retaining and transparent gels. It also plays key roles in cellular activities that include cell regulation, migration and adhesion, cell communication, signal transduction, and

wound healing. Due to its biocompatibility, HA is widely in the pharmaceutical, medical device and cosmetic industries, although its half-life in the body is relatively short, typically less than24h, due to action of endogenous hyaluronidase (HYAL) enzyme. Chemical modification of the polysaccharide can both enhance its biological properties and decrease the rate of its hydrolysis.

HA can also be modified to target particular proteins. An example was the attachment of a β-D-galactose-containing moiety,1-amino-1-deoxy-lactitol (LAC-NH_2), to generate a new biopolymer named HYLACH®. The presence of the lactose residue enabled the interaction and the sequestration of galectin-3 (Gal-3). Gal-3 is a 30 kDa β-galactoside-binding protein, belonging the lectin family, involved in several physiological and pathological processes, including idiopathic pulmonary fibrosis (IPF) which is a chronic life-threatening disease, characterized by the formation of fibrotic scar tissue in the lungs, leading to respiratory failure and death. Gal-3 is overexpressed in myofibroblast proliferation, fibrogenesis, tissue repair and inflammation, making it a critical target in fibrotic disease pathways.

The molecular weight distribution of HYLACH® was in the range 85 to 290 kDa, dependent on the staring material. The degree of substitution, determined by a bidimensional NMR method, was found to vary between 14% and 44%, depending on the synthetic conditions. Interaction studies, performed with isothermal titration calorimetry and circular dichroism, with Gal-3 protein demonstrated affinity of HYLACH® oligomers towards Gal-3.

These findings highlight the safety and biocompatibility of HYLACH® and support its potential therapeutic application in IPF.

The second part of the thesis was focused on the study of the interaction phenomena between the pentosan polysulphate (PPS) and platelet factor 4 (PF4). PPS is a semisynthetic, highly sulphated polysaccharide, that exhibits a structure analogous to that of heparin, and, like heparin, it interacts with PF4. PPS is the active ingredient of Elmiron, a drug approved by both the FDA and EMA for the treatment of interstitial cystitis and bladder pain syndrome. PPS also exhibits anticoagulant, antiviral, and anti-inflammatory properties.

Although being a relatively rare problem, PPS is also associated with clinical manifestations of heparin-induced thrombocytopenia (HIT), an immune-mediated adverse reaction characterized by an immune response to aggregates of PF4 and heparin.

The formation of the PF4/PPS aggregates was investigated using physico-chemical and biological analyses, and these interactions were compared to those induced by heparin. Complex formation was assessed using a combination of orthogonal analytical techniques including dynamic light scattering, zeta potential, atomic force microscopy, isothermal titration calorimetry, and enzyme immunoassay. As expected, the size and Zeta potential at the neutralization point of PPS/PF4 complexes depended on molar ratios of the ligand. The effect of PPS complexes with PF4 was intermediate between those formed by PF4 with UFH and LMWH. However, immunoassay

demonstrated that PPS provoked interactions with PF4 comparable to those of heparin, highlighting the necessity of further investigation before parenteral administration of PPS.

The final topic of the project focused on the encapsulation of polysaccharides into lipid nanoparticles (LNPs). These drug delivery systems, representing the most recent nanocarriers to have been approved for the administration of the Pfizer-BioNTech and Moderna vaccines, are characterised by low toxicity, biocompatibility, protection of the active content from moisture, pH, and enzyme activity, and the ability to encapsulate both hydrophobic and hydrophilic molecules. These particles have the capacity to be directed towards target tissues, allowing the release of active content at specific sites. This has applications in the treatment of several diseases, such as tumours, mucopolysaccharidosis, IPF. Polysaccharides such as HA and heparin are particularly susceptible to degradation by endogenous enzymes. In their usual form, their high Mw and charge may compromise their ability to reach target sites efficiently and, owing to their poor oral bioavailability, they can often only be administered through invasive routes. Encapsulation within LNPs promises to overcome these limitations by protecting the polysaccharides from enzymatic degradation, enhance their biodistribution, and reduce their side effects.

LNPs were produced with a microfluidic system, to allow precise control on their size, and to ensure high homogeneity and excellent reproducibility. The lipid formulation used consisted of Dlin-MC3-DMA: cholesterol: 1,2-distearoyl-sn-glycero-3-phosphocholine (DSPC): DMG-PEG2000. LNPs were produced using different polysaccharides, such as HA, PPS and heparin, and were characterized using manifold analytical techniques, including transmission electron microscopy, nanoparticle tracking analysis and dynamic light scattering. All the formulations were characterized by sizes <120 nm and low polydispersity, except for HA-LNPs. Hep-LNPs were purified using size exclusion chromatography, and the encapsulation efficiency was 80%. Cell studies, performed at the university of Liverpool, demonstrated that fluorescent heparin encapsulated in LNPs is able to cross the cell membranes, demonstrating the potential of this system for intracellular delivery.

Chapter 1
GENERAL INTRODUCTION

1.1. Carbohydrates

Carbohydrates are the most abundant class of natural organic compounds on Earth. They serve a variety of functions in living organisms, including providing a structural support, storing energy and mediating cellular signalling. Interest in these polymers has grown in recent years due to their potential applications in the biomedical and pharmaceutical fields. These name of these compounds originates from their general formula, $(CH_2O)_n$, where *n* is equal to three or greater. Carbohydrates are generally classified according to their molecular size, which corresponds to the number of "sugar" units, in monosaccharides, oligosaccharides and polysaccharides.

1.1.1. Monosaccharides

Monosaccharides are the simplest building blocks units of carbohydrates. They are colourless, soluble in water and aqueous solution, and insoluble in non-polar solvents. The simplest monosaccharide is glyceraldehyde, represented by the formula $C_3H_6O_3$. This molecule contains three carbon atoms, and it is classified as a triose. Monosaccharides can be classified into two main categories, according to the functional groups presents on the molecule:

1. **Aldoses**: characterised by the presence of an aldehyde group (-CHO), examples include glucose, which is a primary energy source in living organisms, and galactose, which plays a key role in the formation of glycoproteins and glycolipids.
2. **Ketoses**: characterised by the presence of a ketone group (C=O), examples include fructose, commonly found in fruits and honey, and ribulose, which participates in photosynthesis.

Due to their nature the structure of the monosaccharides comprises a series of stereoisomers.
The structure of an aldose (glucose) and a ketose (fructose) is shown in *Figure 1-1*.
This figure shows the *Fischer projections*, which are two-dimensional schematic representations of the atoms in open chair form in carbohydrates, described as the intersection of horizontal and verticals lines. This description allows the straightforward identification of the chirality of each chiral atom.
In a Fisher projection, the aldehyde or the ketone groups are always positioned at the top, while the hydroxyl and hydrogen groups, attached to each carbon, are shown on the right or left. From a Fischer projection, it is also possible to describe the absolute configurations **D-** and **L**. The D-form, in which the hydroxyl group farthest from the carbonyl group of the sugar is represented as

pointing to the right in the Fisher projection, is more common in most sugars. Its stereoisomer, characterised by a left-oriented -OH group, indicates an L configuration.

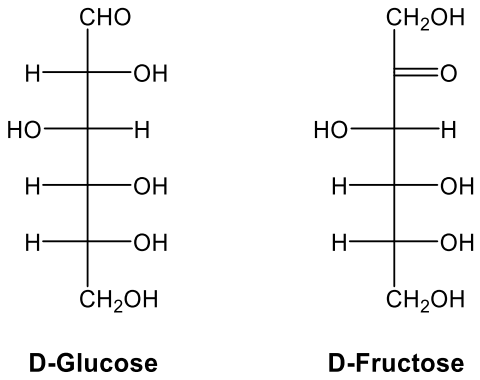

Figure 1-1: ***Example of aldose and ketose.*** *Left) Fischer projection of the aldose monosaccharide D-glucose, right) Fischer projection of the ketose monosaccharide D-fructose*

Approximately twenty monosaccharides exist in nature, while around fifty have been artificially synthetised. Monosaccharides served not only as energy sources, but also as building blocks for more complex carbohydrates such as oligosaccharides and polysaccharides.

Monosaccharides can cyclise through the formation of a hemiacetal bond. Most of these cyclic structures contains five- or six-membered structures, and are referred to as furanose and pyranose, respectively.

Furthermore, these monosaccharides can adopt different configurations in solutions, which exists in equilibrium with each other. For example, glucose can assume the four distinct configurations reported in *Figure 1-2*.

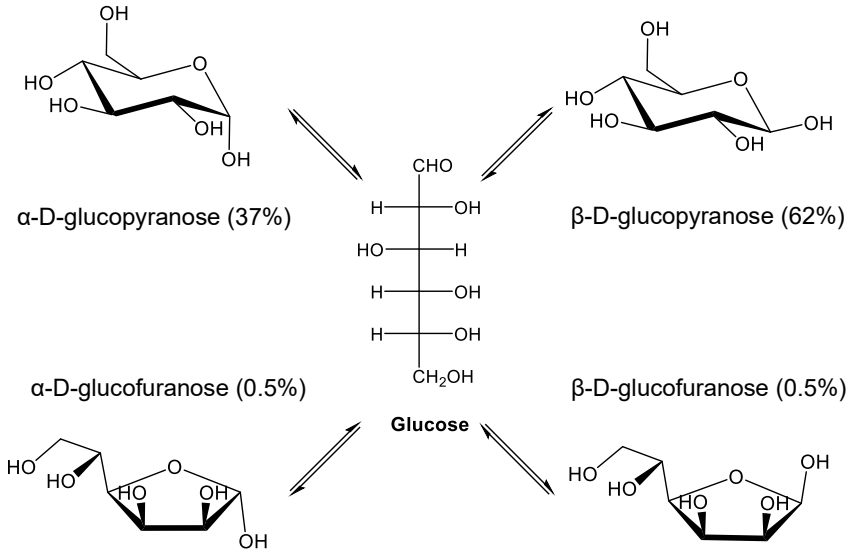

Figure 1- 2: ***Configurations of the form of D-Glucose in equilibrium in water solution.*** *The structures are reported with their relative percentage of pyranose and furanose structures.*

1.1.2. Oligosaccharides

The condensation of two monosaccharides leads to the formation of a disaccharide, (*Figure 1-3*). The most common disaccharide is sucrose, commonly known as table sugar, which is formed through the linkage, called **glycosidic bond**, between one glucose molecule and one fructose molecule.

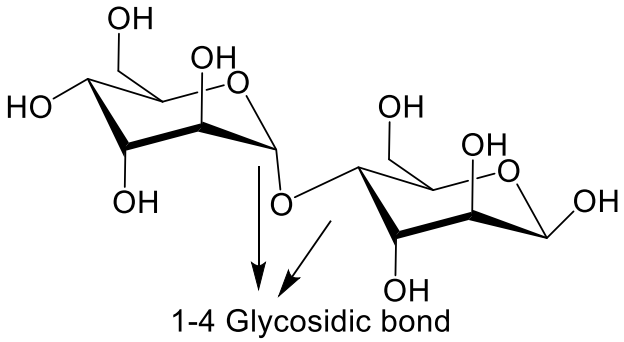

*Figure 1-3**: Disaccharide structure.** The glycosidic bond which links the two monosaccharide is evidenced by two arrows.*

In nature, glycosidic bonds are formed when a hydroxyl group from one monosaccharide reacts with the hydroxyl carbon of another, eliminating one molecule of water, in an enzymatically catalysed condensation reaction. In the chemistry laboratory, the hydroxyl group of the acceptor monosaccharide reacts with the anomeric carbon of the donor sugar. These glycosidic bonds, which define both the configuration at C-1 of the former donor sugar (beta-D, alpha-L, etc) and the linkage positions (1,3, 1,4 or 1,6), influencing the overall conformation of the resulting molecule. Ultimately, these structures features determine many of the macroscopic properties oligo- and polysaccharides. [1]

1.1.3. Polysaccharides

While three or more monosaccharides are linked together, they form oligosaccharides, typically consist of three to ten monosaccharides unites. Polysaccharides, on the other hand, are natural polymers composed of more than ten monosaccharides linked together by glycosidic bonds, with molecular weights (Mw) ranging from tens of thousands to several million. [2]

These essential macromolecules constitute the most abundant class of biopolymers on Earth, and they present and active roles in various biological processes, including embryonic development, cell communication, bacterial and viral recognition, tumour metastasis and other physiological processes such as protection, adhesion, and immune modulation. [3]

For many decades, polysaccharides have been employed in a wide range of industrial applications, including medical device, pharmaceutical, biomaterials, food, energy and textiles. [4] In recent years, this macromolecules have attracted growing interest, particularly for biomedical

applications, owning to their biocompatibility, biodegradability, low toxicity, and potential therapeutic properties. [5]

The biological activities of polysaccharides are strongly influenced by their chemical structure and chain conformations. Polysaccharides are generally classified based on their structure as either homo- or hetero-polysaccharide. A homo-polysaccharide is a polymer in which only one type of repeating unit is present, while a hetero-polysaccharide is defined as a polymer composed of two or more different type of monosaccharides. Additionally, the polysaccharides can be either branched or unbranched. [3] Polysaccharides can also be classified based on their superficial charge as: neutral, if they do not have any net charge on their surface; anionic, if they present a net negative charge related to the presence of acid functional group, like carboxyl (-COOH), sulphate ($-SO_3H$) and phosphate ($-PO_4^{3-}$) groups; and cationic if they carry a positive charge due to the presence of an amine ($-NH_3$) group.

1.1.3.1. Sources of bioactive polysaccharides

In nature, polysaccharides are found in almost every living organism, including plants, fungi, bacteria, algae, and animals, where they are synthetised to serve numerous biological functions, such as energetic storage and structural support. *Table 1.1* provides example of various sources of common polysaccharides.

Plant polysaccharides perform two main functions: storage and structure. [6]

- Storage polysaccharides, such as starch, which served as energy reserves.
- Structural polysaccharides, including cellulose, xylans and pectin, which provided flexibility and rigidity.

Algae are also rich in polysaccharides, with their content ranging from 4% to 76% of the organism's dry weight depending on the species. Algae are capable of synthesising a variety of macromolecules, including agar, carrageenan and alginate. In certain species of green algae, lignin, cellulose and hemicellulose have also been identified. [6]

Fungi produce both linear and branched polysaccharides in their cell walls, including pullulan, elsinan, and β-glucans. [6]

Bacteria produce polysaccharides which are characterised by rheological, gelling and stabilising properties. In addition, they may possess also antitumor, anti-inflammatory and antimicrobial activities.

They could be produced extracellularly or intracellularly, according to the substrate and the type of bacteria used. Commun example of the polysaccharide produced by bacteria are dextran, gellan, xanthan, and sodium hyaluronate (HA). [6]

Animals produce polysaccharides for structural, storage and energy purposes. In addition, polysaccharides derived from animals are typically biodegradable, non-toxic, non-antigenic and

biocompatible. Key components of animal polysaccharides are glycosaminoglycans (GAGs), including heparin and HA. Other notable animal polysaccharides include chitin and chitosan. [6]

Table 1- 1: ***Sources of common polysaccharides.*** *Table adapted from Díaz-Montes*. [6]

Sources	Polysaccharide Examples
Plant polysaccharide	Cellulose Glucuronoxylan
Animal polysaccharide	Heparin Chondroitin sulphated Sodium hyaluronate
Microbial polysaccharide	Dextran Sodium hyaluronate Pullulan Xathan
Algae polysaccharide	Alginate Carrageenan

1.2. Some important polysaccharides

1.1.1. Sodium hyaluronate (HA)

Sodium hyaluronate is a heterogeneous, non-sulphated polysaccharide discovered by K. Meyer and J. W. Palmer in 1934. It belongs to the class of GAGs and is a linear anionic polymer composed of repeating disaccharide units of **D-glucuronic acid** and **N-acetylglucosamine** linked via **β(1,4)** and **β(1,3)** glycosidic bonds (*Figure 1-4*). [7]

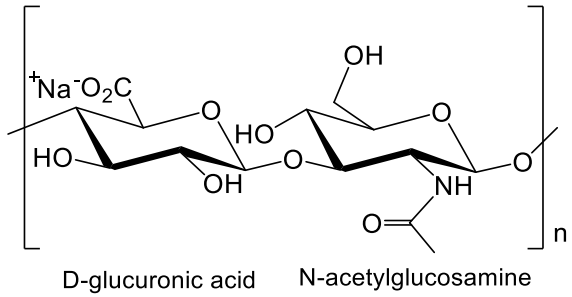

Figure 1- 4: ***Sodium hyaluronate (HA) repeating disaccharide structure***

Sodium hyaluronate is found in vertebrates as well as in many bacteria. In humans, it is one of the components of the extracellular matrix (ECM), where it serves both structural and functional roles. It is particularly abundant in the synovial fluid of joints, the dermis of the skin, and the vitreous body of the eye. [7], [8]

This polysaccharide was commonly extracted from sources such as rooster combs, shark skin, human umbilical cords, and bovine vitreous humour. The concentration of HA varies significantly across tissues, for example rooster combs contain approximately 7.50 mg/mL of HA, whereas human umbilical cords contain about 4.1 mg/mL. [9]

Recently, high-purity HA has been produced through biotechnological methods using bacterial expression systems, including species such as *Lactococcus* and *Streptococcus*. These biotechnological approaches offer an alternative to animal-derived sources, yielding HA with consistently high purity. [6]

The Mw of HA depends on its sources and can reach up to 10^6 Da. This parameter is critical in determining its biological functions, affecting viscosity, water retention capability and interactions with cellular receptors. [10]

The structural and hydration roles of HA are attributed to its ability to retain large amounts of water. [7] In addition, HA is involved in important cellular processes such as regulation, migration and adhesion, and supports the growth of eosinophils, macrophages and epithelial cells. It is also participates in cell communication, ECM organization, wound healing, scar formation and signal transduction, through interactions with receptors such as the cluster of differentiation-44 (CD44) and the receptor for hyaluronate-mediated motility (RHAMM). [11] Only HA oligosaccharides,

with a Mw below 10 kDa, are involved in stimulating fibroblast proliferation and promoting angiogenesis.

All the properties mentioned above, combined with its safety, biodegradability and non-toxicity, make HA a highly versatile molecule widely used in the pharmaceutical, medical device and cosmetic industries. Its use in healthcare was estimated to be worth approximately 7.3 US billion in 2024, and its value is in continuous growing. [12]

High molecular weight (HMW) HA is extensively employed in the pharmaceutical fields for wound healing, due to its ability to preserve tissue integrity and promote repair. It is also commonly used as a lubricant and visco-supplement for in joint therapies and dermal filling applications, owing to its excellent viscoelastic properties. In contrast, low molecular weight (LMW) HA, typically below 10 kDa, is frequently used in cosmetics, as its smaller size enable deeper penetration into the skin layers, enhancing hydration and skin elasticity. [10]

HA, however, is characterised by a relatively short half-life, typically less than 24 hours, due to its degradation by enzymes like hyaluronidase (HYAL) or internalisation by CD44 cell receptors. [13]

One useful feature of HA is its functional groups, which enable various chemical modifications, in order to introduce desirable properties such as enhanced biological activities, reduced of the rate of hydrolysis or prolonged circulation times.

There are three primary sites for HA modification: the hydroxyl groups, the N-acetyl groups, and the carboxylic groups. These functional groups enable two main types of modifications: **conjugation**, in which molecules are covalently attached to HA, and **crosslinking**, which forms a network structure to alter its physical and mechanical properties, as illustrated in *Figure 1-5*. [14]

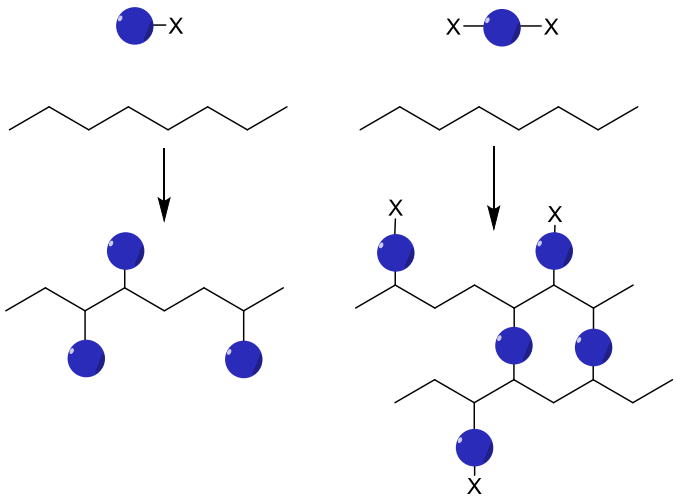

*Figure 1- 5**: HA modifications: chemical conjugation and cross-linking.** Imagine adapted from Schanté et al.* [14]

Alongside native HA, cross-linked and functionalised HA are also being used more frequently, accounting for 30% and 10% of the market respectively.[12]

1.1.2. Heparin

Heparin is a natural sulphated GAGs, a class that also includes polysaccharides such as chondroitin sulphate (CS), dermatan sulphate (DS), keratan sulphate and sodium hyaluronate.
Heparin was identified for the first time by Jay McLean and William Henry Howell in 1916, [15] and it is one of the oldest and most widely used anticoagulant and antithrombotic drugs, with nearly 90 years of clinical application. [15]
The use of heparin as anticoagulant began in 1935, shortly after its discovery. [16] Despite, the detailed elucidation of its structure started later, in the 1960s and 1970s, due to its complex nature. [17] This progress was made possible by advances in analytical techniques, such as nuclear magnetic resonance (NMR), as well as the development of milder acid hydrolysis methods and sample fractionation. [17]
Heparin is the most highly sulphated GAG found in nature, and it is produced in mast cells of connective tissue, especially in the intestine, lungs, and liver in humans and other mammals, as well as in other vertebrates and invertebrates.
Currently, this polysaccharide is mainly obtained from animals, and the only heparin approved by the FDA for clinical applications comes from porcine mucosa. Specifically, about 300 mg of heparin can be obtained from the intestinal mucosa of a 130 kg adult pig. [15] -[19]
Heparin structure consists of a linear, unbranched polysaccharide that typically adopts a helical conformation, with a Mw ranging from 3000 Da to 30000 Da. [18] It is composed by repeating disaccharide units of a uronic acid (either β-D-glucuronic acid or α-L-iduronic acid) and α-D-glucosamine linked by (1→4) glycosidic bonds. These units exhibit variable sulfation patterns at the N and O positions, as well as in the presence of N-acetyl groups of uronic acid (IdoA) and glucosamine (GlcNS), contributing to its structural heterogeneity. [19] The GlcN residue is predominantly in the N-sulphated form (GlcNS), with N-acetylated (GlcNAc) form less common, and residues with a free amino group (GlcN) are rare; IdoA residues and GlcN residues are O-sulphated at positions 2 and 6, respectively. More rarely, GlcN is sulphated at position 3. [19]
Figure 1-6 shown the major heparin residues, consisting of 2-O-sulphated α-L-iduronic acid (IdoA2S) and N-, 6-O-disulphated glucosamine (GlcNS6S), which form the trisulphated disaccharides. [17], [20], [21]
Heparin structure is additionally characterised by different sulfation patterns, which are irregularly distributed along the heparin chain, as well as by variable chain lengths. These patterns create regions with different charge densities referred to as N-acetylated (NAc) and N-sulphated (NS) domains. The NS domains (highly sulphated) are mainly concentrated near the reducing end

of the chain. Mixed domains consisting of both N-acetylated and N-sulphated regions (NAc/NS) may also be present.

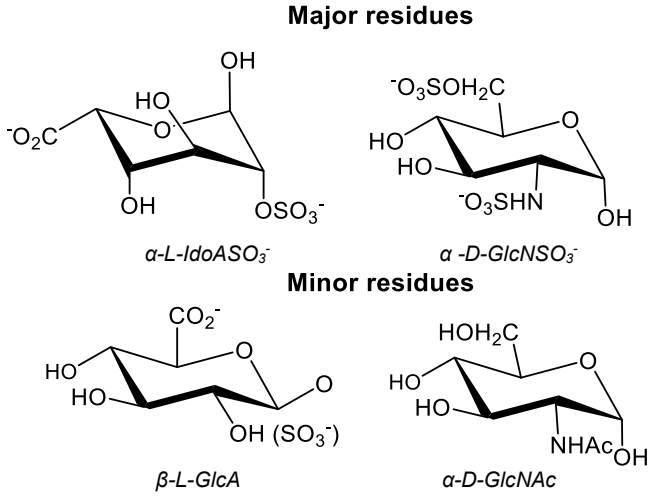

Figure 1- 6: ***Heparin monosaccharide residues.*** *On top are reported the major residues which represent the trisulphated disaccharides (TDS, IdoA2S-GlcNS6S), on the bottom are represented the minor residues, the less common forms are shown in brackets.*

The anticoagulant activity of heparin is primarily related to its interaction with the antithrombin (AT) III, a serine protease inhibitor regulates key coagulation factors (Xa and IIa), and the stabilisation of the inhibitor/enzyme complex.

In detail, the pentasaccharide sequence AGA*IA, (αDGlcNAc/ NS(6S)- βDGlcA- αDGlcNS(3S,6S)- αLIdoA- αDGlcNS(6S), shown in *Figure 1-7*), which is present in certain heparin chains, binds to a specific site on antithrombin known as the AT-binding domain (AT-BD), inducing conformational changes in ATIII. These structural modifications lead to the exposure of a reactive loop that enhances the inhibition activity of AT towards thrombin and other coagulation proteases (Xa and IIa). [22]

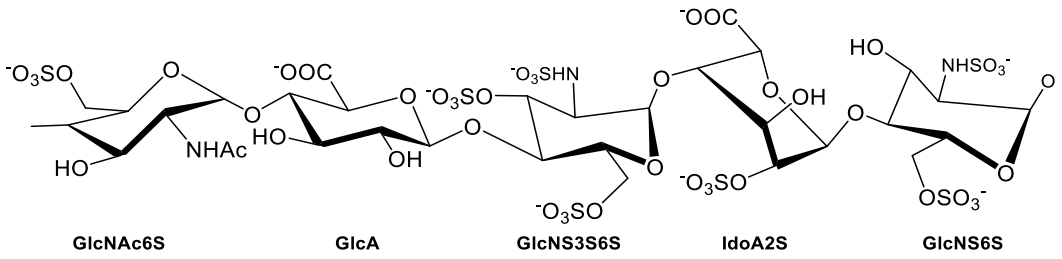

Figure 1- 7: ***Heparin binding pentasaccharide (AGA*IA).*** *This specific pentasaccharide sequence is responsible for its anticoagulant activity. Structure identified by Thunberg et al.*[23]

The thrombin and Xa inactivation follow similar mechanisms. The main difference between between the two interactions, is that factor Xa can be directly inactivated by the heparin pentasaccharide, through a specific protein/protein (AT-Xa) interaction, whereas thrombin binds non-specifically to the same heparin molecule that is already bound to AT. This implies that the

heparin chain must consist of at least 13 monosaccharide units, from the non-reducing end of the pentasaccharide, in order to bind to thrombin. *Figure 1-8* illustrate the mechanism by which heparin prevents blood clot formation.

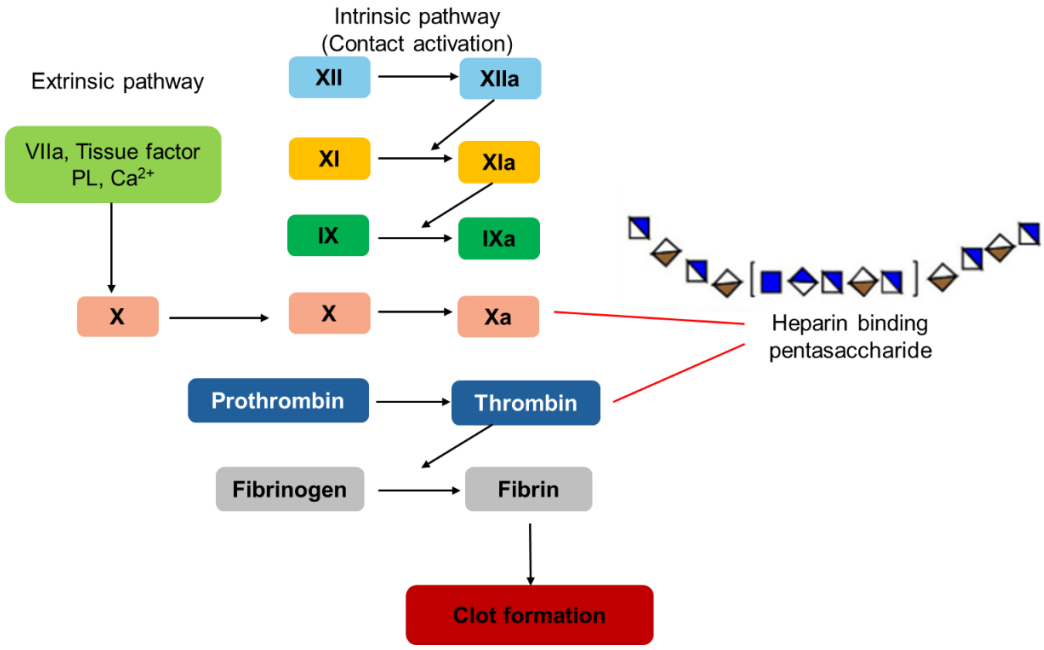

Figure 1- 8: ***The mechanisms of heparin within the coagulation cascade.*** *Figure adapted from Hao et al.* [18]

In addition to its anticoagulant activity, heparin plays a significant role in the immune defense mechanism and due to its highly sulphated structure, it interacts and regulates the action of hundreds of proteins involved in physiological and pathological processes, included pathogen infection, angiogenesis, allergic response, cell differentiation and growth inflammation and homeostasis. [18] Heparin exhibits a structural similarity to the cell surface GAG, heparan sulphate (HS), which is characterised by a generally longer molecular structure and reduced sulphation levels. HS functions as a receptor for extracellular proteins., including growth factors, chemokines, and cytokines. It also regulates the function of several proteins such as acute phase proteins and complement proteins. Owing to its abundance and relatively low cost, allied to their close structural similarities, heparin and its derivatives are widely used as experimental tools to investigate HS-related biological activities. The potential pharmaceutical applications of heparin include its use in:

1. **Anticancer therapy**. Clinical studies have shown that the administration of heparin to cancer patients can increase their chances of survival. Although its mechanism of action is not yet fully understood, it is hypostatised than its anticancer properties depend on its interfering with cancer cell adhesion, migration, and angiogenesis, by modulating the activity of tumour necrosis factor. [15]

2. **Treatment of viral and infectious diseases**. Heparin inhibits pathogen adhesion to cell surfaces. [24] Several studies have reported that heparin and its derivative can be used as inhibitors of the *herpes simplex* virus and *merozoite*. [18]
3. **Allergic and Anti-inflammatory disorders**. Heparin possesses anti-inflammatory properties, due to its ability to inhibit the activation of the neutrophil and the release of inflammatory mediators. Additionally, heparin facilitate the production of bradykinin, a hormone that influences cell swelling, anaphylactic and inflammatory symptoms. [23]

Despite its many potential pharmaceutical applications, heparin can cause non-haemorrhagic complications, such as osteopenia, hypoantithrombinemia and heparin-induced thrombocytopenia (HIT). HIT results from the direct interaction between heparin and platelets, leading to platelet aggregation and an immune response. This complication necessitate careful and continuous monitoring of patients. [25] To reduce these risks, modified forms of heparin, known as low molecular weight heparins (LMWHs), were developed and introduced to the market.

LMWHs are characterised by a Mw ranging from 2.5 to 8 kDa. They are typically achieved by size fractionation or, more commonly, by the chemical or enzymatic depolymerisation of unfractionated heparin (UFH). These chemical or enzymatic methods employed include treatment with nitrous acid, degradation with heparin lyase I, radical-catalysed peroxidative cleavage, or γ-ray irradiation. [26]

Both UFH and LMWH are characterised, however, by poor absorption profiles. Their relatively large molecular weight (compared to typical small molecules drugs), strong negative charge and hydrophilic nature result in low skin permeability and poor oral bioavailability. Consequently, both require invasive parenteral administration, typically via subcutaneous or intravenous injection. [27] [28] [29]

They also have short circulation times and are rapidly cleared. UFH has a half-life of approximately 1–2 hours, while LMWH exhibits an extended half-life of around 5 hours, both require continuous or repeated infusions. [30]

1.1.3. Pentosan polysulphate (PPS)

Pentosan polysulphate (PPS) is a semi-synthetic highly sulphated polysaccharide, whose chemical structure is relatively similar to heparin and other GAGs. It is produced through a semi-synthetic process involving exhaustive and non-selective O-sulfation of 4-methyl glucuronoxylans derived from beechwood. [31], [32]

The PPS backbone consists of repeating β-D-xylopyranose (Xyl) units connected by (1–4) linkages. This linear polyxylose chain is interspersed with 4-O-methyl-glucuronic acid (MGA) units, linked α(1-2) to the xylose molecules. The degree of branching varies depending on the

source material. This variability results in a complex mixture of sulphated polysaccharides with an average Mw of approximately 6 kDa and a high polydispersity index (about 1.6). [31],[33]
Detailed studies of the PPS mixture have demonstrated that all the internal xylose and MGA residues were sulphated at the 2-O and 3-O positions. [31] Minor species, observed at the reducing end have been attributed to process-related impurities, and includes 2,3-unsaturated xylose, methylated xylose, and pyridinium-complexed xylose residues. The overall PPS structure, including both major and minor residues, is illustrated in *Figure 1-9*.

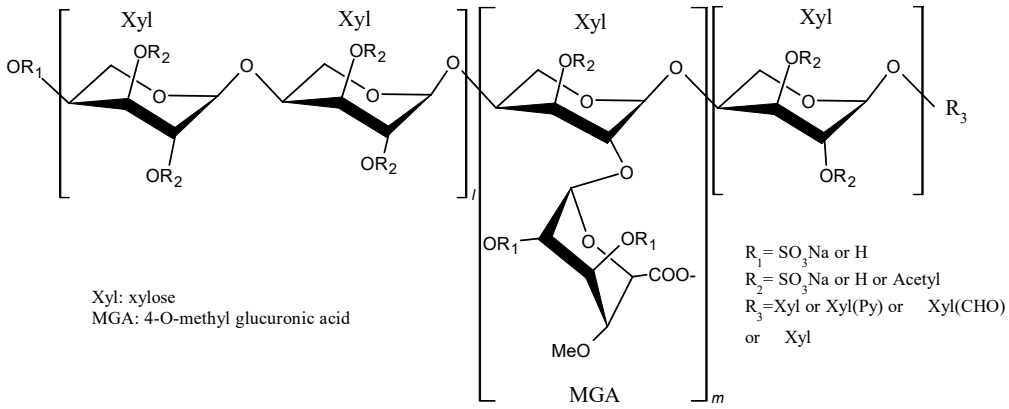

Figure 1- 9: ***PPS prevalent structure.*** [31]

Pentosan is a biologically active polysaccharide, which is used as an active ingredient in several pharmaceutical products. PPS is frequently utilised to enhance joint hydration and lubrication, as well as to prevent the osteoarthritis in animals.
Like heparin, PPS has been shown to exhibit both anticoagulant and anti-fibrinolytic activities. However, its anticoagulant activity is approximately 15 times weaker than that of heparin. [34]
Furthermore, PPS is the active ingredient in **Elmiron®**, an FDA approved drug used for the treatment of interstitial cystitis or bladder pain syndrome, a chronic condition characterized by abdominal and perineal pain, accompanied by severe urinary urgency and frequency. [35],[36],[37]
The exact mechanism of action is not fully understood. However, it is hypostatised that PPS helps to repair or replace the damaged components of the GAG layer in the bladder, increasing the protection and reducing bladder inflammation. It may also exhibit anti-inflammatory effects, inhibiting the release of histamine and reducing the activation of mast cells in connective and mucosal tissues. [31],[38]
Additionally, PPS has been investigated for various other medical applications, including its capacity to control hepcidin expression,[39] serve as an antiviral agent against HIV[40] and SARS-CoV-2, [41] and manage mucopolysaccharidosis. [42] Its diverse range of therapeutic effects highlights its potential for broader clinical use.
Oral administration of PPS is characterised by low bioavailability, typically less than 3%, with peak plasma levels reached approximately two hours after administration. [43]

Moreover, cases of maculopathy were first reported in patients undergoing long-term PPS treatment in 2018. This condition was characterized by symptoms such as prolonged dark adaptation and difficulty reading, leading to significant visual dysfunction.[44]

1.3. Modification of carbohydrates

Modifications of the polysaccharides are often necessary to achieve desired properties, modulate the behaviour of polysaccharides and increase their bioactivity.

The modification of compounds through chemical, physical, or biological methods enables the generation of a wide range of derivatives, *Figure 1-10*. [45], [46]

2. *Chemical modification*

A common strategy for the chemical modification of carbohydrates involves the introduction of functional groups, including alkylation, sulphation, carboxymethylation, phosphorylation, acetylation, polymerisation and others, on the hydroxyl, carboxyl, or amino groups.

Other type of chemical modification involves the linkage of a polysaccharide to an active molecule, such as a small drug, a protein, a peptide, or another polysaccharide, in a process called conjugation. Conjugation can be direct, or it can require the presence of a spacer, or linker, between the polysaccharide and the active molecule.

Chemical modifications are often used to improve the pharmacokinetics and pharmacodynamics of a drug by influencing parameters such as viscosity and water solubility. These methods are also used in drug delivery systems (DDS), tissue engineering and bioadhesive applications. [11]

3. *Physical modification*

Physical modifications are often used to reduce the lengths of the polysaccharide backbone, generating fragments or oligomers with lower Mw. This approach preserves the chemical structure of the polysaccharide, with modifications occurring primarily at the chains' length level. This class of modification involves techniques such as ultrasonic disruption, radiation-induced processes and microwave irradiation. [46]

4. *Biological modification*

Biological modifications of polysaccharides involve the use of enzymes, to allow a controlled degradation of the native polymer with high specificity and selectivity. This results in the formation of oligomers with a uniform distribution.

This approach, however, can only be applied to specific types of natural polysaccharide. Additionally, the capacity of the enzyme to modify or degrade polysaccharides could be affected by the chemical modification of the macromolecules. Despite these limitations, these enzymatic methods are widely used to depolymerise high molecular weight polysaccharides, in order to reduce their Mw and simplify their characterization.

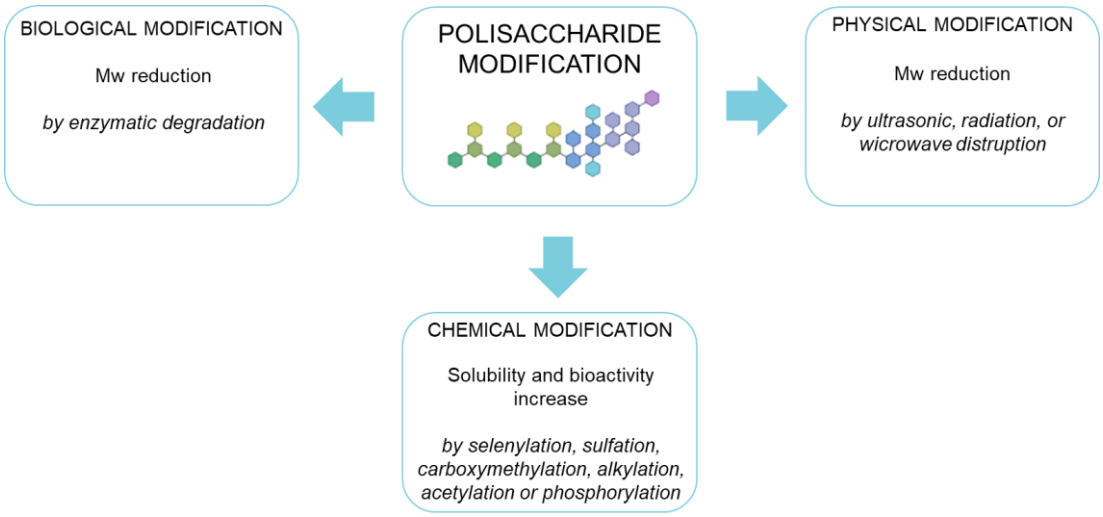

Figure 1- 10: ***Polysaccharide modifications.*** *Sources adapted from Li S. et al.*[46]

During polysaccharide modification, it is crucial to evaluate two parameters:

- **Degree of substitution (DS)**, which indicates the extent of derivatization by a measuring the average number of substitutions per monomer unit.
- **Degree of polymerization (DP)**, which indicates the average length of the polysaccharide chain, expressed in the repeating monomer units. [45]

1.4. Characterization

The structural characterisation of polysaccharides is often challenging due to their molecular complexity and polydispersity. This complexity arises from the diverse composition of the monosaccharides, variations in glycosidic bond linkage patterns, branching position and configuration, the presence of different functional groups, and the distribution of molecular weights. [1] Additionally, chemical modifications and crosslinking increase this complexity. Despite the significant importance of polysaccharides and their derivatives in the pharmaceutical and medical industry, regulatory bodies guidelines focus mainly on native macromolecules. No guidelines have been defined for functionalised materials. A notable example is HA, for which, despite the increasing demand for crosslinked and modified HA on the market, [12] the European Pharmacopoeia only provide guidelines for the characterisation of native HA, [47] employing techniques such as infrared (IR) spectroscopy and intrinsic viscosity. These methods are inadequate for accurately determining purity and degree of derivatisation.

A comprehensive and exhaustive structure characterisation of the structure of polysaccharides often requires several and orthogonal techniques. Some of the most common methods are:

- *Size Exclusion Chromatography (SEC),* which separates molecules based on their hydrodynamic radius, enabling the determination of molecular weight distribution.

- *Nuclear magnetic resonance (NMR)*, which is based on nuclear spin coupling with magnetic fields and provides structural and dynamic information.
- *Mass spectroscopy*, which measures the mass to charge ratio (m/z) of ions, allowing the identification of the molecular structures and chemical composition.
- *Infrared Spectroscopy (IR)*, which used short range vibration to identify functional groups presents within the molecules.
- *UV-visible spectroscopy*, which exploits the absorption of ultraviolet and visible light by chromophores present within the sample, enabling qualitative analysis and, in some case, the determination of the concentration of the compound.

1.5. Interactions

Carbohydrates play a crucial role in numerous biological processes, including inflammation, cell-cell interactions, cellular growth, angiogenesis and signal transduction. The structure features, composition and functional groups of carbohydrates enable them to interact and form complexes with biologically relevant molecules, such as proteins, lipids, nucleic acids and other carbohydrates. [48], [49]

A variety of techniques have been developed to study and investigate interactions between polysaccharides and proteins. Among the most common methods, there are microcalorimetry, fluorescence intensity, absorbance intensity, surface plasmon resonance, and the enzyme-linked immuno assay (ELISA). [50] NMR spectroscopy, X-Ray diffraction and cryo-electron microscopy are often used for the determination of the structure of the carbohydrate-protein complexes. [51]

Recently, new techniques have emerged for investigating of these complexes, such as photo correlation spectroscopy for determining size distribution, electrophoretic light scattering for evaluating surface charge, and atomic force microscopy for measuring the complexes.

Most of these interactions exhibit, however, low-affinity association. Together with the low solubility of proteins, this greatly complicates the measurement of ligand binding.

1.6. Lipid based drug delivery system

Despite the biological activities of polysaccharides and their potential applications in the pharmaceutical industries, only a limited number of carbohydrate-based therapeutics are currently available on the market.

This limitation is related to the low absorption rate of polysaccharides, due to by their susceptibility to enzymatic degradation, high clearance rates in the body, and poor bioavailability. This issue is particularly evident in intestinal absorption, where molecules with a molecular weight higher than 500 Da are unable to cross biological membrane. [52]

The encapsulation of bioactive polysaccharides in drug delivery systems (DDSs) can enhance their stability, bioavailability and circulation times. Furthermore, such systems can reduce the side effects of the cargo and enable a controlled release at specific sites.

In recent years, there has been a significant development of several drug delivery systems, including lipid-based drug delivery systems (LBDDS), microparticles, dendrimers, gold nanoparticles, and niosomes (non-ionic surfactant vesicles capable of encapsulating both hydrophilic and lipophilic drugs). [53], [54] Among these approaches, LBDDS have emerged as the most attractive and versatile carriers thanks to their high biocompatibility, high biodegradability, ability to transport both hydrophilic and hydrophobic drugs and targeting ability. Furthermore, LBDDS are the first nanoparticles drug delivery system approved in clinical use. A schematic representation of the most common LBDDS is reported in *Figure 1.11*.

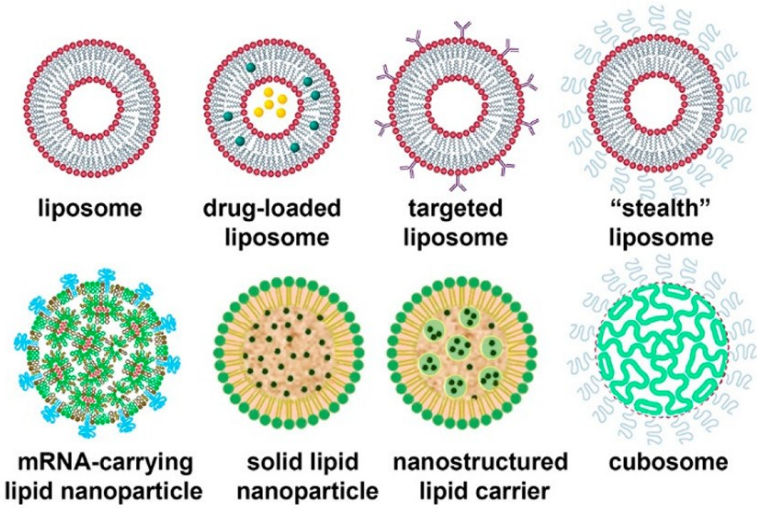

*Figure 1- 11:**Main categories of LBDDS**. Preprint form Tenchow et al (2021).60*

The simplest and earliest LBDDS are liposomes, which were discovered in the 1965 by Bangham. [55] They consist of lipid aggregates with a spherical, vesicle-like structure, that form spontaneously in an aqueous environment. Since their discovery, the potential of liposomes and

their use as a promising therapeutic delivery platform gained increasing interest. This growing interest has led to continuous and progressive advancements in their formulation.

1.6.1. Uses of LBDDS

Thanks to their versatility, LBDDS are employed across a wide range of fields, including pharmaceuticals, cosmetics, food and agriculture. In the cosmetics fields, LBDDS are employed to enhance the permeation of active molecules into the superficial layer of the skin, increase the chemical and physical stability of the formulation, enhance water resistance and enable a slow release of the content of active ingredients.[56]

In the agricultural industry, LBDDS improve the effectiveness of biocides and to ensure the gradual and timely administration of essential nutrients. [57]

In the food and beverage industries, LBDDS are used to protect sensitive additives, including enhancing of flavour, and increasing of colours, or preserve products. [58]

Despite their widespread use, most of the advances and applications in LBDDS technology have occurred in the pharmaceutical field. Starting from the approval of a liposomal formulation containing propofol, called Diprivan, in 1989, for patient sedation, these nanocarriers (NCs) have been used for the administration of numerous other drugs. Epaxal, a lipid base hepatitis A vaccine, was approved in the 1993, followed by approval of Doxyl in 1995, the first anticancer formulation containing doxorubicin encapsulated in a PEGylated liposome, designed for the treatment of ovarian cancer. LBDDS are also used in fungicides, a commercial example is Fungizone, and in analgesics like DepoDur. [59] In 2002, Rapamune become the first orally administered LBDDS immunosuppressant approved for clinical use. More recently, continuous progresses in formulation of LBDDS, enable to the development of NCs for RNA and gene therapy delivery. The first approved siRNA-based drug is Onpattro (Patisiran), designed for the treatment of polyneuropathy. The unique feature of this drug is its innovative formulation based on lipid nanoparticles (**LNPs).** The same formulations were later employed for the delivery of mRNA-based COVID-19 vaccines.[59]

1.6.2. Lipid nanoparticles composition

Lipid nanoparticles, the most effective delivery systems for nucleic acid-based therapies, are composed of a complex combination of different type of lipids, each presenting a specific and distinct function. Typically, LNP formulations include polyethylene glycol (PEG)-conjugated lipid, helper lipids and ionizable cationic lipid. [59]

The use of ionisable cationic lipids in LNPs is a relatively recent development. Initially, permanently cationic lipids, with a permanent positive charge, were used. Studies demonstrated

that the presence of quaternary amine groups, which confers the cationic moiety to the molecule, was linked to toxicity issues. [60][61]
Safer alternatives have been developed in the form of ionisable cationic lipids, which only acquire a positive charged under acid conditions. This minimises adverse effects and reduces cytotoxicity. Among these, DLin-MC3-DMA has emerged as a key component in advancing LNP technology and ultimately contributed to the clinical approval of Patisiran in 2018. [61]

1.6.3. LBDDS production methods

The methods used to produce LNPs influence key parameters relevant to their commercial approval and mechanism of action, including their physical and chemical properties, their encapsulation efficiency, their stability and their size distribution. Consequently, the choice of a production method is a fundamental factor in determining the potential applications of the final products.
Significant progresses have been made in the productions of the LBBDs, particularly regarding formulation control. Early production methods were based on mechanical dispersion techniques, such as sonication, lipid film hydration, micro-emulsification and membrane extrusion. These relatively inexpensive, however, they suffer from limited over formulation parameters, resulting in variable reproducibility, high polydispersity, and suboptimal encapsulation efficiency.
More recent advances have involved the development of sophisticated and more complicated and higher cost techniques, such as macrofluidic system, T junction and microfluidic system.
The first two approaches provide improved encapsulation efficiency, size control and greater homogeneity. However, they still present challenges in terms of reproducible, and their output is in the order of millilitres scale. [62]
Microfluidics, on the other hands allows one to achieve excellent size control, high encapsulation efficiency, but also great homogeneity and repeatability. These instruments permit the production of variable volumes, ranging from μL to L, they are easily scalable, and they enable the reduction of sample consumption.[63]

1.6.4. LBDDS characterization

The FDA has issued the guidance "*Liposome Drug Products: Chemistry, Manufacturing, and Controls; Human Pharmacokinetics and Bioavailability; and Labeling Documentation*" to provide recommendations for the production and characterization of liposomal drug products. [64][65]
This guidance defines the critical quality attributes (CQAs) of LBDDS, focusing more on liposomal formulations, including particles size, polydispersity index, zeta potential,

encapsulation efficiency, physical stability and release of the content. Additionally, it outlined the characterization and stability studies of the starting materials, lipids and drug substances. The CQAs criteria are schematically reported in *Figure 1-12*. [66]

Among the various analytical techniques employed, dynamic light scattering (DLS) is used to assess size distribution and polydispersity. Electrophoretic light scattering is used to determine the surface charge, expressed as the zeta potential. Imaging techniques, such as transmission electron microscopy (TEM), scanning electron microscopy (SEM) and atomic force microscopy (AFM) are often employed to investigate nanoparticles morphology. Nanoparticles tracking analysis (NTA) is used mostly to determine the concentration of the particles in solution, in addition to providing size distribution. [66]

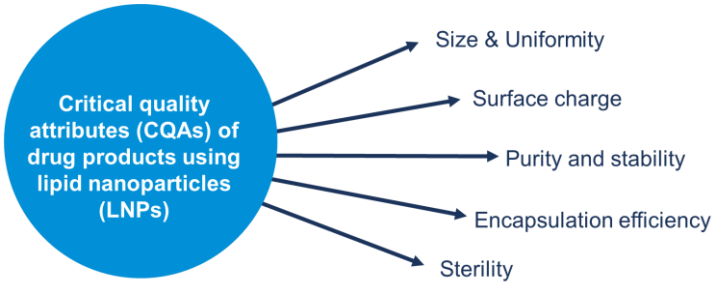

Figure 1- 12: ***CQAs of LBDDS.*** *Adapted from Fan et al.* [66]

Chapter 2

TECHNICAL INTRODUCTION

2.1. Chromatography

Chromatography is a routine technique used to separate, purify or analyse complex mixtures. Chromatography techniques involve the use of:

- A stationary phase, generally a solid phase.
- A mobile phase, which can be either a liquid or a gas.

Chromatography enables the separation of different components within a mixture based on their specific physicochemical properties. Depending on the structure and composition of the sample, different chromatographic approaches can be employed, including ion exchange chromatography, gel permeation chromatography and affinity chromatography. [67]

In particular, size exclusion chromatography (SEC) is widely used for preparing molecular fractions of complex samples, desalination, buffer exchange, and estimating molar mass.[68]

2.2. Size exclusion chromatography (SEC)

Polysaccharides are defined as complex mixtures of polymers with variable chain lengths and, consequently different molecular weights. For this reason, it is important to describe the molecular weight of a polysaccharide as a distribution of molecular weights (MWD).

The MWD can be determined using size-exclusion chromatography (SEC), a liquid chromatographic technique that separates macromolecules based on their molecular size and consequently on their hydrodynamic radius (Rh). This technique is also referred to as gel permeation chromatography (GPC), gel filtration chromatography, steric exclusion chromatography and exclusion chromatography. A schematic representation of the mechanism of a SEC technique is shown in *Figure 2-1*.

Figure 2-1 illustrates an ideal separation of a mixture of three components with different size. After injection, the mixture enters in the head of the column. Thanks to the presence of a liquid mobile phase, which flows through the column at a constant and controlled rate, the polymer mixture enters the column, or stationary phase.

This stationary phase is packed with a porous material of defined pore size. Larger molecules, due to their higher size, are unable to penetrate in the polymer network and remain within the interstitial space of the stationary phase. As a result, they flow more rapidly through the column

and elute first. In contrast, smaller molecules are able to penetrate more deeper into the polymer matrix, slowing down their passage and delay their elution. [69]

Consequently, the largest molecules are eluted first, followed by medium-sized molecules, and finally, the smallest one. Separation is achieved based on their differing retention volumes. Typically, a detector is positioned at the end of the column and record their elution. All SEC separations occur within a defined range of retention volumes, between Vo and Vt. Vo refers to the total exclusion volume, while Vt corresponds to the volume which is the sum of the interstitial volume and pore volume.[69]

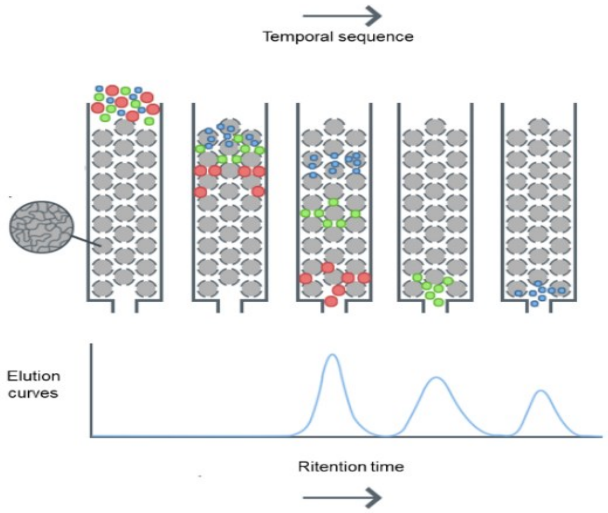

*Figure 2- 1**: SEC separation of three macromolecular sizes.** The chromatographic separation of three macromolecules at different size are shown as snapshots over time (upper, from left to right). The elution curves profile also shown (lower), illustrating their separation based on retention times, largest molecules eluting earlier (to the left of the chromatogram).*

2.2.3. Chromatographic conditions

Chromatographic SEC elution is dependent on several factors including 1) system temperature; 2) mobile phase; 3) columns type; 4) flow rate.

A selection of these parameters is essential for achieving effective polymer separation

- *Mobile phase:* It must completely dissolve the polymer, it must possess low viscosity to maintain normal system pressure, and it must not interact with the stationary phase or with polymer molecules. The mobile phase may consist of either an organic or an aqueous solvent.
- *Stationary phase*: The packing material should not interact chemically with the sample. It must be fully wetted without swelling and remain stable at operating temperatures. It should also provide an adequate pore volume and size distribution for molecular weight separation. In general, columns may contain monodispersed or mixed-bed particles of different pore size to allow analyses of molecular weights ranging from a few hundred to

several million. Increasing the particle size or extending the length of the columns can improve the separation between two components.

- *Flow rate*: must be selected to provide an optimal balance between good resolution and analysis time. Typically, the flow rate does not exceed 1mL/min.

2.2.4. SEC parameter description:

Polysaccharides consist in a population of molecules characterized by a range of molecular weight, which can be described using various parameters that differ by their counting procedure, but which emphasise distinct aspects of molecular population.

- ***Number-average molecular weight (Mn)***

The number-average molecular weight (Mn) is described by the following formula:

$$Mn = \frac{\Sigma c_i}{\Sigma c_i / M_i} \quad (1)$$

Where M_i is the molecular weight at the ith data point, and c_i is the concentration of at the ith data point. [70] This value is correlated to the flexibility of polymers, and it is function of low Mw material. [71]

- ***Weight-average molecular weight (Mw)***

The weight-average molecular is described by the formula: [70]

$$Mw = \frac{\Sigma M_i c_i}{\Sigma c_i} \quad (2)$$

Mw is correlated, instead with the strength of polymer, and the content of high-Mw chains in the polymers. [71]

- ***Zeta average molecular weight (Mz)***

The zeta average molecular weight is defined by:

$$Mz = \frac{\Sigma {M_i}^2 c_i}{\Sigma M_i c_i} \quad (3)$$

The Mz is strictly correlated to the amount of very high-Mw material. Generally, by definition Mn<Mw<Mz.

- ***Polydispersity index (PDI)***

The polydispersity index measures the width of the MWD curve. Lowest is the PDI, narrowest is the MWD and smaller is the molecular weight range. In a perfectly monodisperse sample, in which all chains have identical lengths (such as a protein), the PDI value is 1, this means that Mn=Mw=Mz. [70][71]

$$PDI = \frac{Mw}{Mn} \qquad (4)$$

Figure 2-2 describes these parameters on the molecular weight distribution.

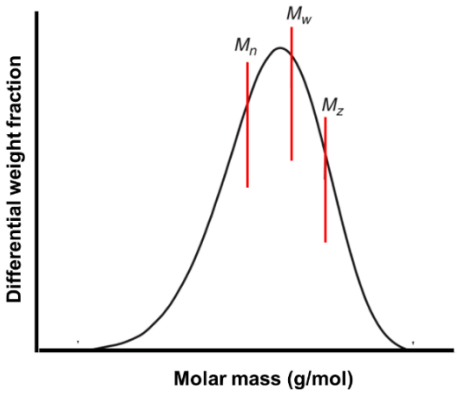

Figure 2- 2: ***Molecular weight distribution and parameters.*** *Adapted from Striegel et al.*[68]

2.2.5. Calibration

In size exclusion chromatography, samples elute according to their molecules size, however, to correlate their elution or retention volume to molecular weight, system calibration is required. There are three main calibration methods:

- ***Direct standard calibration (conventional calibration)***

This method involves the use of narrowly distributed polymer standards to generate a calibration curve for the analysed polymer. Although it is the simplest method, easy to set up, and provide good repeatability and reproducibility, when using one detector (i.e. refractive index, or UV), it has some limitations. It requires multiple standards, with different molecular weights to cover the dynamic range of the column set, which are not always available. In addition, structural changes such as branching, influence the accuracy of this calibration method.

- ***Polydisperse or Broad Standard Calibration***

This method required a broadly distributed polymer standard, with a molecular weight distribution covering the sample's dynamic range. It is particularly useful when narrow standards or molecular weight-sensitive detectors are unavailable.

- ***Universal calibration***

Introduced in 1967 by Benoit, this method allows the absolute molecular weight calibration of samples of different chemical structures using narrow polymer standards. In detail, Benoit demonstrated that the product of the intrinsic viscosity ($[\eta]$) and the Mw is proportional to the elution volume for all the polymers studied.

The intrinsic viscosity represents the specific viscosity of a polymer divided by its concentration, measured in a solution under conditions of infinite dilution. This value can be detectable by a viscosimeter detector.

Molecular weight (M) and $[\eta]$ are in related by the Mark-Houwink equation *5*:

$$[\eta] = KM^a \qquad (5)$$

where K and a represent the Mark-Houwink constants, which are function of the polymer and environment. Although, this method is sensitive and provides information about the Mw and branching of the polymer, it requires information about the sample concentration, and a sample with a Mw in the sample range and involved the use of two detectors (a concentration detector and a viscosimeter detector). [71]

2.2.6. Size exclusion chromatography with triple detector array

In SEC systems, one or more detectors, connected at the end of the columns, detect the elution of the molecules.

A High-Performance Size Exclusion Chromatography (HP-SEC) with a Triple Detector Array (TDA) is an SEC instrument equipped with three detectors: a light scattering detector, a viscometer and either refractometer or UV detector. This instrument enables the distribution of molecular weights, without the need to calibrate the column with different standards at various molecular weights.[72]

A schematic representation of a HP–SEC/TDA is shown in *Figure 2-3*.

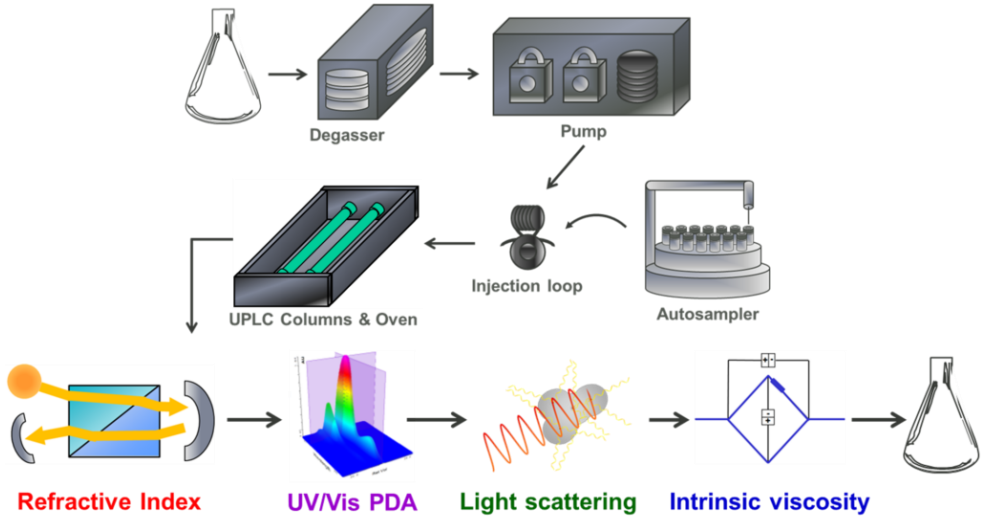

Figure 2- 3: ***Schematic of an HP-SEC-TDA system.*** *Figure reprint from Williams et al.* [73]

The HP-SEC/TDA system consists of a degasser, which removed bubbles from the solution, followed by a pump that allows the flow of the mobile phase into the system. A solution of the sample to be analysed is then injected, either manually or via an autosampler, into the system. This solution then passes through the columns, which enable the elution of the sample according

to its size. It then passes into the detectors, such as the photodiode array (PDA), which includes both RI and UV, as well as a laser and a viscometer. The signal recorded by detectors is called a chromatogram.

The **three detectors** -Refractive Index (RI), Viscometer (DP), and Light Scattering (LS)- work simultaneously to provide multiple information of the sample, including molecular weight distribution (Mw, Mn, Mz, PDI), intrinsic viscosity (η), concentration, hydrodynamic radius (Rh) and Mark-Houwink parameters (a, K).

Although HP-SEC/TDA overcomes the challenges of obtaining suitable reference standards, a single-point calibration using a narrow standard is still required. For the calibration, the standard must have known values for concentration, **dn/dc**, or **dA/dc**, if the UV detector is used, parameters that describes the increase in RI or assorbance as a function of concentration, molecular weight, and intrinsic viscosity in the chosen mobile phase.

These known parameters allow the determination of detector response factors (K) for each detector, using formulae *6,7,8* and *9*.

$$\boldsymbol{RI\ Output\ (mV)} = K_{RI} * \frac{dn}{dc} * concentration * inj.vol. \quad (6)$$

$$\boldsymbol{UV\ Output\ (mV)} = K_{uv} * \frac{dA}{dc} * concentration * inj.vol. \quad (7)$$

$$\boldsymbol{LS\ Output\ (mV)} = K_{LS} * Mw * \left(\frac{dn}{dc}\right)^2 * concentration * inj.vol. \quad (8)$$

$$\boldsymbol{DP\ Output\ (mV)} = K_{visc} * IV * concentration * inj.vol. \quad (9)$$

Where C: concentration of the sample in solution; output: signal peak areas from the detectors; K: instrumental constants; IV: intrinsic viscosity. [74]

2.2.6.1. Differential refractive index (RI)

The RI detector is the most widely used universal detector in SEC to determine polymer concentration, and its response is directly proportional to the sample concentration. It responds to most polymeric samples; however, it is extremely sensitive to temperature fluctuations and requires more stable conditions, typically within 10-15°C above room temperature.

Other types of concentrations detectors are the ultraviolet (UV) and infrared detectors, which are able to detect the presence of functional groups present in the molecules (chromophores). [69]

2.2.6.2.Light scattering (LS)

The intensity of the light scattering signal, is related to the Mw by the Rayleigh equation 10 reported below.

$$\frac{KC}{R(\theta)} = \frac{1}{Mw * P(\theta)} + 2A_2C \qquad (10)$$

Where: R(Θ) : Rayleigh ratio; C: Polymer concentration; Mw: molecular weight; A_2:2nd virial coefficient, P(Θ): particle scattering function.

At low concentrations, equation *10* can be approximated to:

$$R(\theta)|_{\theta \to 0} \sim KCM \qquad (11)$$

To ensure the validity of the relationship, the intensity of the scattered light must ideally be measured at a scattering angle of 0°. Direct measurement at this angle is, however, not possible, instead, the intensity at 0° is estimated by extrapolating data obtained from measurements at other angles.[69], [70], [74]

In general, most GPC systems are based on two different LS detectors.

- ***RALS (Right-angle light scattering) detector***, which is used for the detection of light scattering at a 90° angle. This detector is ideal for small molecules with a radius of gyration below 10–15 nm, which scatter light isotropically. [69]
- ***LALS (Low-Angle Light Scattering) detector***, which measure the scattering of the light at 7°. This detector is used for molecules with a greater radius, higher than 10–15 nm, which exhibit anisotropic scattering, where the intensity varies with angle. [69]

2.2.6.3.Viscometer (DP)

The viscometer detector provides directly information about the intrinsic viscosity, detecting the pressure drops across a capillary between the sample and the mobile phase. Intrinsic viscosity (η) is calculated as:

$$\eta = \frac{DP * \ calibration\ constant}{IP * concentration} \qquad (12)$$

Where DP is the differential pressure and IP is the inlet pressure. [69], [70]

The η is additionally connected by the Mark-Houwink equation (*equation 5*) to the Mw.

2.3. Nuclear Magnetic Resonance (NMR)

NMR spectroscopy is a non-destructive spectroscopic technique widely used for the characterisation of molecules of organic origin. This technique is widely used not only for the analysis and characterisation of both small and large molecules, but also to detect the presence of impurities in a sample, identify functionalisation and study the interactions between small molecules and proteins.[75]

NMR is based on the magnetic properties of atomic nuclei, which thanks to their positive charge, rotate on their own axis, generating a magnetic dipole and producing a magnetic field. [76]

These dipoles are characterised by a quantum spin magnetic number, called I, which depends on the type of atom. For example, the I value of ^{1}H is 1/2, while for ^{2}H is 1. Further examples are carbon atoms, ^{12}C the I is equal to 0, indicating that it is not optically active at NMR, but its isotope 13C has an I value of 1/2.

When active nuclei are placed in an external magnetic field, they tend to align either with or against its directions. This orientation is defined by the magnetic quantum number, denoted *m*, which assumes values from +I to -I.

The energy difference between the spin orientations is related to the strength of the applied magnetic field (B_0) and the gyromagnetic ratio (γ) of the nucleus, to provide a slight excess in the occupancy of the lower over the higher state (described by the Boltzmann distribution). The difference in energy is described by the equation *13*:

$$\Delta E = \gamma \, h \, B_0 / 2\pi \qquad (13)$$

where h is Planck's constant.

When a proton absorbs a photon of electromagnetic energy, it enters a state of resonance, transitioning between the lower and higher energy level to annihilate the population difference. The difference between the two populations is in the order of one part in 10,000. The NMR signals are proportional to this difference, for this reason this technique is considered inherently less sensitive.

In order to resonate, the energy that has been absorbed must equal the energy difference between the two states. A short radiofrequency (RF) waves, of 5–10 μs, can excite all the nuclei in the sample at the same time, from the z-direction into the x-y plane.

When they are excited, the nucleus relaxes and tries to return to their equilibrium state, along the z-axis, releasing energy. The emitted signal, which is generally released in an arc of time between 100 ms and 5s, is called free induction decay (FID). The acquisition of this signal, provide an NMR spectrum in the time domain, which after a Fourier transform can be converted into a frequency-domain spectrum.

Nuclei are not isolated systems, but they are influenced by their chemical environment, which in turn affects their electron density. This enables atoms to resonate at different frequencies. The resulting signal position is dependent from the applied magnetic field. In order to eliminate this dependence, the **chemical shift** (δ), which indicates the variation of the signals position from a standard, such as the trimethylsilane, has been introduced.

δ is influenced by the electronegativity of nuclei. Nuclei close to electronegative atoms are subject to reduced electron density around them, denoted as deshield. furthermore, the bonding electrons influence the shield or deshield of atoms in a phenomenon referred as magnetic anisotropy. This event is observed more with π electrons.

An NMR signal is defined by three main elements: shape, intensity, and width. The shape of the signal is determined by the FT of the FID. The width of the signal depends on relaxation time and the dynamic properties of the molecule. And the intensity of a signal is proportional to the number of nuclei that generate the signal—this is particularly accurate for ^{1}H, for which the relaxation times are often respected. The coupling between two nuclei generates a signal multiplicity, causing signal splitting. The splitting of the signals can be defined as doublet (d, two lines), triplet (t, three lines), and so on. Furthermore, a nucleus can be couplet to several nuclei, generating complexity in the spectra. The separation between the lines is known as the coupling constant (J), and it is independent from the magnetic field applied, but it is dependent on both the type and the number of bonds connecting the coupled nuclei.

For example, in carbohydrates, the determination of J allows the identification of the stereochemistry of the molecules. In β-D-glucose pentaacetate all the hydrogen are arranged in axial position. The measurement of J between H1 and H2 enable the identification of the stereochemistry of the molecule and to distinguish it from the α-D-glucose pentaacetate. This is possible due to the different value of J for the two molecules, which is about 12 Hz in an axial-axial coupling (β-D-glucose), and about 4 Hz in an axial-equatorial coupling (α-D-glucose).

^{1}H and ^{13}C NMR spectra are one-dimensional spectra, where the intensity is plotted against a single frequency axis.

Compared to proton NMR spectroscopy, ^{13}C NMR spectroscopy is much less sensitive due to its low natural abundance (about 1.1% of all carbon atoms) and long acquisition times. However, ^{13}C NMR allow a greater signal dispersion, due to the higher δ which ranges between 0 to 220 ppm and is usually not affected by coupling to other ^{13}C nuclei, since they are so rare, hence, ^{13}C spectra are relatively simple compared to ^{1}H spectra.

The correlation of the signal intensity with two frequency axes (F1 and F2), results in a **two-dimensional (2D)** NMR spectroscopy. 2D experiments can correlates with frequencies of the same type of nucleus (homonuclear), or frequencies of different nuclei (heteronuclear).

COSY (COrrelation SpectroscopY) is a homonuclear 2D NMR experiment, which is used to identify scalar-coupled protons. This technique is primarily used in the case of molecules with

complex structure. The spectrum is typically characterised by the presence diagonal peaks, known as cross-peaks, which are autocorrelated and divide the plot into two symmetrical halves.

TOCSY (TOtal Correlation Spectroscopy) is a homonuclear 2D NMR experiment that provides correlations between all protons present in the same spin system, even if they are not directly coupled.

HSQC (Heteronuclear Single- Quantum Correlation) is a heteronuclear 2D NMR experiment that allows the correlation between two heteroatoms, usually ^{13}C and ^{1}H. In contrast to homonuclear experiments, HSQC does not display the autocorrelation cross-peaks. But its cross-peak corresponds to the coupling between two heteroatoms, one directly bound to each other.

2.4. Ultraviolet and visible spectroscopy

Ultraviolet and visible (UV-Vis) spectroscopy is an absorption technique that involve the use of light, at wavelengths ranging between 190 nm to 900 nm, for the identification and the determination of the concentration of a sample.

After the passage of light through a sample, there is a difference between the incident radiation (I_0). and the transmitted radiation. This difference in the amount of light is called absorbance, and it is dependent from the interaction between the light and the electron of a chromophore.[77]

Specifically, absorbance (A) is practically defined as the logarithm of the inverse of transmittance (T), where T is the ratio of the transmitted intensity to the incident intensity.

$$A = \log\left(\frac{1}{T}\right) \; and \; T = \frac{I}{I_0} \qquad (14)$$

The absorption of the light depends on several factors such as the thickness, the coefficient and the solute concentration, as expressed by the Lamber Beer law, reported in equation *15.* [78]

$$A = \varepsilon C l \qquad (15)$$

Where C is the concentration of the sample, l the path length of the sample cell, and ε the molar extinction coefficient.

Spectrophotometers consist of a light source, a dispersion device (e.g. a grating), that separate the radiation, a sample compartment and a detector, which measure the intensity of the transmitted light. [77], [79] This simple, fast and inexpensive instrument finds application in biological and chemical sciences, where it is used for the identification of molecules in solutions, in the determination of their concentration, and in the study of chemical reactions or their purifications. Additionally, UV–Vis spectroscopy can be coupled with other instruments to enhance their sensitivity.[80]

2.5. Infrared spectroscopy (IR)

Infrared (IR) spectroscopy is an analytical technique that investigates the interaction between infrared light and matter. These interactions induce vibrations in molecular bonds, between quantized energy states. [81]

After exposure to IR light, the components of a sample (which can be modelled as atomic masses joined by a 'spring-like' chemical bonds) absorb energy at specific wavelengths. This leads to vibrations (3N-6, for typical complex molecules of N atoms, ignoring complex overtones) that depend on the molar structure. This process generates a spectrum with distinct peaks, the positions of which enable the identification of the functional groups present in the molecules.

There are various types of IR spectrometers in commerce, despite the most widely used is the FTIR (Fourier Transform Infrared) spectrometer. [82]

IR spectroscopy is a versatile and complementary technique, commonly used to characterise organic compounds. Applications include identifying of unknown samples, demonstrating an occurred derivatization, determining the quality of starting materials, and comparing of different batches. Some of their advantages include high versatility, high sensitivity and resolution, and rapid data acquisition. Additionally, IR spectroscopy is a not disruptive technique that requires only a small amount of sample. Additionally, it can also be applied to insoluble materials or solutions. The IR spectra of carbohydrates exhibit distinct absorption regions that correspond to the various functional groups present in the molecules, as detailed in *Table 2-1*. Generally, the IR spectrum ranges between 4000 cm^{-1} and 400 cm^{-1}, with the range from 950 to 1200 cm^{-1}, identified as the fingerprint region of carbohydrates. [82]

Table 2- 1: ***Characteristic FTIR absorbance positions for common functional groups of polysaccharides Adapted from Khan et al.*** [82]

Wavenumber (cm^{-1})	*Functional groups/vibration mode*	*Intensity*
3500–3000	O–H stretching Broad, strong	Broad, strong
3000–2800	C–H stretching, symmetric,	Sharp, double overlapping with O–H
1630-1600	Asymmetric	Strong
1400	Sharp, occasionally double	Weak
1380	Overlapping with O–H	Weak
1280-900	Finger-print of carbohydrates	Strong

2.6. *Light scattering (LS)*

In addition to the absorption of light by matter, the interaction between the two may lead to phenomenon of scattering. The occurrence of this phenomenon is characterised by the induction of a dipole oscillation in the electron cloud of a molecule by an incident photon, resulting in the release of energy in all directions. Scattering is the basis for analytical techniques included dynamic light scattering and electrophoretic light scattering.

2.6.3. Dynamic light scattering (DLS)

Dynamic light scattering (DLS), also called Photo Correlation Spectroscopy (PCS) is a non-invasive analytical technique which allows the diffusion behaviour of macromolecules in solution to be investigated. [83]

This technique is used to measure the speed, in solution and in gases, of Brownian motion, the random movements of molecules and particles that results from their continuous collision with other molecules of the surrounding medium.

In a DLS experiment a laser beam strikes a cuvette containing the sample, where it encounters molecules in solution that scatter the incident light in all directions. The scattered light is measured by a detector (photon counting device) set at a specific angle (θ). As particles are in continues movements, the intensity of the scattered light fluctuates over times, *Figure 2-4*. [84][85]

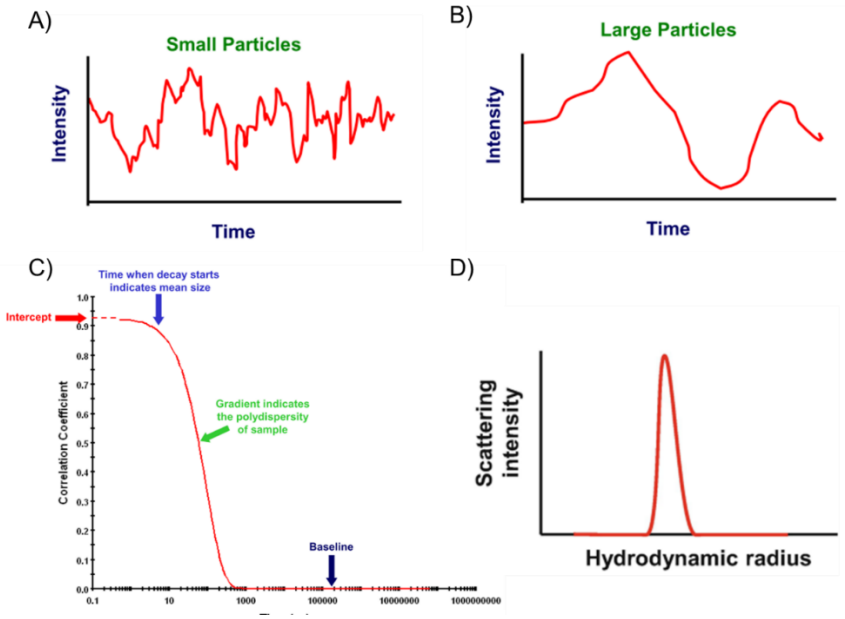

Figure 2- 4: ***Examples of the scattered light of molecules, correlation functions and hydrodynamic radius.*** *(A) scattered light of small particles, (B) scattered light of large particles, (C) correlation function obtained from the digital autocorrelator and (D) hydrodynamic radius achieved after the application of the Stock Einstein equation to the correlations function. Adapted from Malvern [86].*

The Brownian motion is influenced by sample viscosity and temperature, but also by particle size and shape. In particular, it is faster for smaller particles (*Figure 2-4 A*), and slower for macromolecules (*Figure 2-4 B*).

A digital autocorrelator correlates fluctuation in the intensity of the scattered light, acquired in the order of ns or μs. Initially the intensities are similar, indicating strong correlation, however over time the similarity decrease, leading to loss of correlation, (*Figure 2-4 C*). For small particles, characterised by rapid fluctuation in the intensity of the light scattering, the decrease of the correlation function is more rapid, due to their faster movement in solution, while for larger particles, which move slowly, the loss of correlation is slower.

Figure 2-4 C also shows that it is possible to divide the autocorrelation function into three main areas, the first one corresponds to the time in which the particles lost their correlation and depends on their size. The gradient of the correlogram indicates the polydispersity of the sample (PDI), the broader it is, the more polydisperse is the sample. The last part corresponds to the baseline from which is possible to evaluate the presence of different aggregates or large molecules. The PDI value, obtained from the square of the ratio between the standard deviation and the mean, is in the range between 0 to 1. The closer it is to 0, the more the samples are monodispersed. A comparison of DLS and GPC PDI values are reported in *Table 2-2*.

Table 2- 2: ***PDI definition for GPC and DLS***

		Distribution Type			
		Monodisperse		**Polydisperse**	
Parameter	Definition	Uniform	Narrow	Moderate	Broad
PDI from GPC	$\frac{Mw}{Mn}$	1.0	1.0-1.1	1.1-2.0	>2.0
PDI from DLS	$\left(\frac{Std\ Dev}{Mean}\right)^2$	0.0	0.0-0.1	0.1-0.4	>0.4

The Stokes-Einstein equation, *Formula 16* can convert the diffusion coefficient D, which correspond to the velocity of the Brownian motion, into the hydrodynamic radius.

$$d_H = \frac{kT}{3\eta\pi D} \qquad (16)$$

Where d_H: hydrodynamic diameter, k: Boltzmann's constant, T: temperature, η:viscosity and D diffusion coefficient.

The hydrodynamic radius (Rh) is defined as the radius of the hard sphere that diffuse at the same speed as the particle being analysed. This indicates that the Rh corresponds not only to the core particles but also to all the other molecules, such as ions and polymers, which are bound or absorbed to the surface. The shape and the charge of the particle and the ionic strength of the

medium influence the Rh. For example, at high ionic strength, the electrical double layer around the particle is compressed, reducing the apparent size.[85], [86]

DLS could measure particles in the range below 1 nm up to 15 µm and it has numerous applications across various fields. As example, in the biological field, it is used to investigate the homogeneity of proteins, the formation of protein-protein complexes and to study the interaction between protein and molecules. [25], [83]

It is also used for the optimisation of drug delivery system, vaccines, and drug formulations; it found applications also in the paints and ink industries to improve pigments formulations, or in environmental monitoring, where it is used for the evaluation of waste in water treatment. [86], [87]

2.6.4. Electrophoretic light scattering (ELS)

Charged particles in a medium attract ions of the opposite charge to their surface. This creates an inner layer, known as the Stern layer, around the surface. Other counterions are also attracted to the surface, however they are repelled by each other. [88] This allows the generation of a diffuse region, where the concentration of counterions decreases with distance from the particle surface, and it is known as diffuse layer. The electrical double layer, existing around each particle, is represented in *Figure 2-5*.

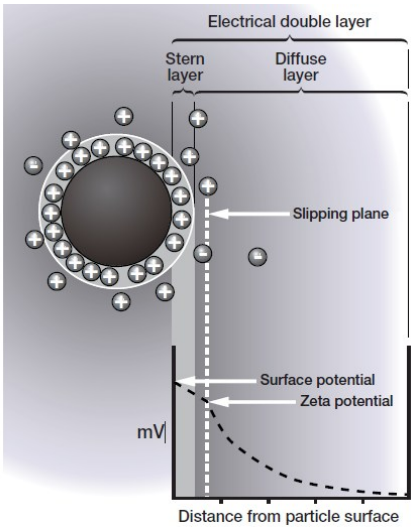

Figure 2- 5: ***Electric double layer structure.*** *Preprint from Malvern. [88]*

When a particle moves, the ions surrounding it within the boundary move with it. This boundary is defined as a slipping plane, and its potential is also known as Zeta potential (Zp or ζ).

The instrument that allows the measurement of the Zp is the electrophoretic light scattering (ELS). ELS is a sensitive technique that measures the movement of charged particles in a liquid under the influence of an electric field, by measuring the frequency shift (Δν) of the scattered light. [89]

When an electric field is applied to a solution, the charged particles and their counterions move to the electrode of the opposite charge, as shown in *Figure 2-6*.

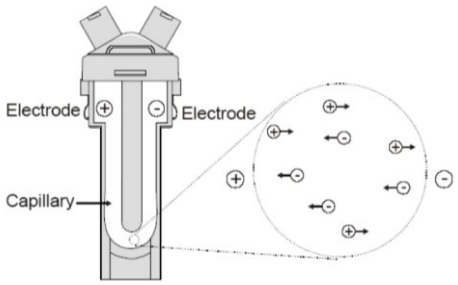

Figure 2- 6: ***The movements of a particle in presence of an electric field.*** *Preprint from Shawn et al.[86]*

ELS measure the electrophoretic mobility (μ_E), which is defined as:

$$\mu_E = \frac{V}{E} \qquad (17)$$

where V is the velocity of the particles and E is the electric field strength.

The μ_E is correlated to the to the Zp, with the Henry equation, (*18*), reported below.

$$\mu_E = \frac{2\varepsilon z F(ka)}{3\eta} \qquad (18)$$

Where: μ_E is the electrophoretic mobility; Z the Zp; ε the dielectric constat; $F(ka)$ the Henry's function (with a being the radius of the particles, and k the Debye-Huckel parameter) and η the viscosity.

The Henry equation indicates that the velocity of the movements of particles depends, not only on the strength of the electric field, but also on the dielectric constant and the viscosity of the medium. Consequently, it is difficult to measure the Zp in salted samples or in organic solvents, which possess a ε lower than water, due to the small mobility of the particles. [89]

ELS provides information about the dispersion, aggregation, and flocculation behaviour of colloidal solution. In general, a high or lower Zp, +30 mV or -30 mV, indicates stable formulation, due to the tendency of the particles to repel each other, while low Zp value can results in aggregation within the solution. [89]

2.7. Nanoparticles tracking analysis (NTA)

Nanoparticles tracking analysis (NTA) is a relatively recent tool, first introduced to the market in 2006, useful for the determination of the size and concentration of particles in solution.[90]
The NTA, like the DLS, used both the Brownian motion and light scattering to determine the particle size distributions of samples.
This technique combines light scattering with a charge-coupled device camera to track the movements of particles and determine their hydrodynamic radius using the Stokes-Einstein equation (*Equation 11*). [91] In detail, a laser illuminates a sample chamber containing particles in solution, and a 20x microscope registers all the scattered light. Then the camera registers video files of moving particles. [90]
NTA have the advantages to be applicable to highly diluted solutions. Additionally, this technique is ideal for small molecules, whereas the DLS possess some limitations, due to its intrinsic sensitivity to larger particles. In fact, the presence of dust and aggregates can influence the DLS size determination. [90]
Several studies in the literature compare NTA and DLS,[91], [92] showing similar results in terms of particle size and polydispersity. DLS remains the preferred routine technique for the determination of size due to its simplicity and efficiency. While NTA is more complex, time consuming and requiring a skilled operator for proper sample preparation and data interpretation. NTA has been widely applied in fields such as exosome and microvesicle analysis, vaccine research and development, protein aggregation studies, and nanocarrier characterization.[90] NTA can also be coupled with a fluorescent detector to allow the observation of fluorescent materials within nanoparticles. [91], [92]

2.8. Isothermal titration microcalorimetry (ITC)

Isothermal titration calorimetry (ITC) is a technique developed by E. Freire and co-workers in 1990. [93] This technique is widely used for studying macromolecular interactions, included protein interactions with metals, small molecules, nucleic acid and carbohydrates or their oligomers. [41], [94] A key advantage of this technique is that it does not require immobilization of the sample, enabling direct and reliable measurement of the binding interactions, while preserving the native state of the system. Additionally, ITC provides thermodynamic data, including binding affinity, stoichiometry, enthalpy, and entropy.
The ITC techniques is based on the measurements of the heat released or absorbed during a titration process. The instruments comprise two different cells, both maintained at a constant temperature: a reference cell, filled with water, and a sample cell containing a protein solution

Figure 2-7A. During an experiment, small and defined aliquots of ligand are injected into the cell containing the protein. When the protein interacts and binds with the ligand, small changes occur in the temperature of the solution relative to the reference cell. A sensor collocated between the two cells, monitors the temperature and detects any temperature variations, sending feedback to the heating system to correct these variations.

These changes in temperature, which occurred after each ligand addition, are registered. An example of the thermogram achieved is reported in *Figure 2-7B.* The presence of positive peaks in the thermogram, such as the one in *Figure 2-7B*, indicates an endothermic process, while downward peaks indicate an exothermic interaction.

In both cases, the signal returns to its starting position after the equilibration of the temperature between the two cells. Successive injections of ligand increase the molar ratio of ligand compared to the protein, saturating gradually the binding site of the protein and consequently decreasing the heat release after each injection. The integration of the area under each peak, allow to recover the heat associated with each injection, which is plotted against the ligand molar ratio in *Figure 2-7C*.[95], [96]

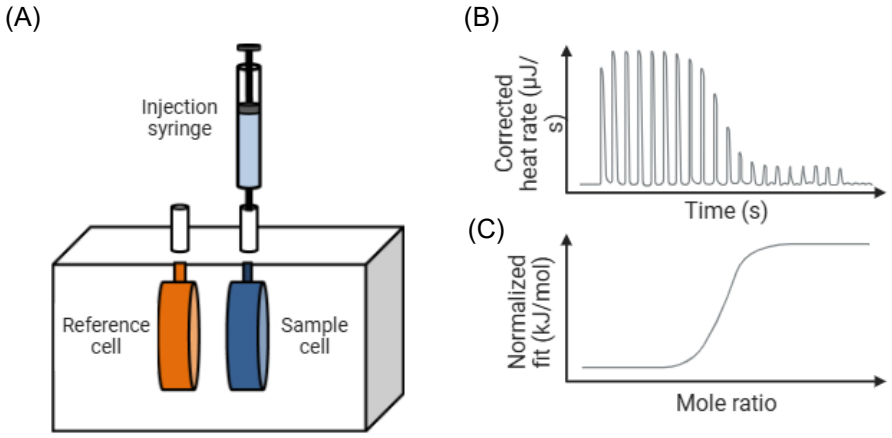

Figure 2- 7: ***Schematic representation of Isothermal titration instruments.*** *(A) A schematic representation of the instrument. (B) The collected raw data registered by the instrument and (C) the resulting elaborated fitting curve, from which is possible to determine the affinity constant (Ka, slope of the curve), ΔH (height of the curve) and stoichiometry (midpoint of the curve).*

The fitting of the curve reported in *Figure 2-7C*, with an opportune binding model, allow the determination of the stoichiometry of the interaction, enthalpy change (ΔH), and affinity constant (Ka). Entropy and Gibbs free energy can be determined from the formula *19*:

$$\Delta G = -RTlnK_a = \Delta H - T\Delta S \qquad (19)$$

where R is the gas constant and T is the absolute temperature.

2.9. *Circular dichroism (CD)*

Circular dichroism (CD) is a spectroscopic technique which can provide information about the chirality of molecular system.

This technique is based on the measure of the differences in the absorbance between the left- and right-circularly polarized light, which is absorbed, in different amounts by any chiral molecules with a chromophore in that frequency range. The differences between the left and right polarized light are expressed in terms of ellipticity (θ).

The CD instrument shares similarities with a UV-Visible spectrophotometer; however, it possesses some additional components such as a polarizer and a photo elastic modulator.

CD spectroscopy has various applications across several fields, included biochemistry, biophysics, medicinal and pharmaceutical chemistry, and organic chemistry. Most of its applications involved, however, protein studies, such as protein folding, stability, and ligand binding. In particular the far-UV (180–240 nm) CD spectroscopy, is used for analysing protein secondary structure. The absorbing groups in this region are the peptide bond, which exhibits two characteristic transitions: a strong $\pi \rightarrow \pi^*$ transition around 190 nm and a broader, negative and weaker $n \rightarrow \pi^*$ transition between 210 and 220 nm, that is sensitive towards hydrogen bond formation (*Figure 2-8*). CD can be used to monitor changes in the protein conformation under various conditions or after interaction with ligands, due to the sensitivity of the secondary structure of proteins to environmental factor such as pH and temperature. [97]

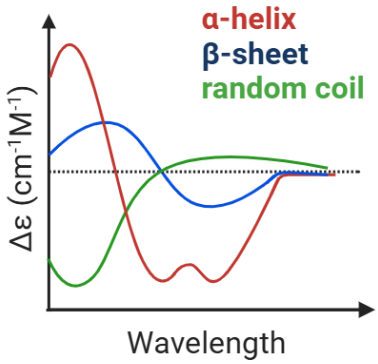

Figure 2- 8: ***Schematic representation of the main differences in the secondary structure in protein****; in green is reported the random coil, in blue the β sheet and in red the α helix.*

2.10. Microfluidic systems

Microfluidic systems are used in numerous applications, including chemical synthesis, diagnosis, crystallisation processes, and most importantly in the production of LBDDS.

In the production of DDS, microfluidic systems, in comparison to conventional liposome formulation methods, reduce and minimise the waste of reagents and organic solvents. They allow to achieve a good reproducibility and encapsulation efficiency, and they these methods also permit to have a greater control over the size of the nanoparticles and their polydispersity.[63] [98]

2.10.1. Impingement jet mixer (IJM)

The impingement jet mixer (IJM), or tea stirrer, is a complex microfluidic technology, which has been used for the production of the mRNA-LNPs (Comirnaty from BioNTech/Pfizer) during the SARS-COV2 pandemic. [98][99]

In this device, two phases, generally an aqueous solution and an organic water-miscible phase, collide rapidly, leading to their mixing. The high-pressure jet generated leads to the formation of droplets, which after the stabilization by surfactants, generate LNPs. [98]

Variations of the mixing parameters (flow rate or sample concentrations) allow to control the properties of the nanoparticles. [100]

The most significant advantages of IJM are its rapidity, reproducibility, ease of use and ease of scale-up.[99]

Chapter 3

HYALURONIC ACID

A novel biomimetic probe for galectin-3 recognition: Chemical synthesis and structural characterization of a β-galactose branched sodium hyaluronate

3.1. Introduction

Galectin-3 (Gal-3) is a β-galactoside-binding protein, that plays a key role in numerous physiological and pathological processes, including idiopathic pulmonary fibrosis (IPF). [101] IPF is a chronic, life-threatening disease, of unknown origin, characterised by the formation of scar tissue in the lungs, which leads to respiratory failure and death within five years after the diagnosis. [102], [103]

Gal-3, encoded by the *LGALS3* gene, belongs to the lectin family, and has a Mw of 26 kDa. It contains a carbohydrate recognition domain (CRD) as well as an N-terminal oligomerization domain. Through the N-terminal domain, Gal-3 can oligomerize to form pentamers. Gal-3 binds β-d-galactose through its CRD, enabling it to interact with β-galactose-terminated glycans or glycoproteins. Thanks to its ability to form pentamers, Gal-3 can crosslink ECM complexes and organise a dynamic lattice. [101]

The roles of Gal-3 are extensive, and it has been implicated in a numerous biological process. Recent studies have shown that Gal-3 expression is associated with myofibroblast proliferation, fibrogenesis, tissue repair, inflammation, and tissue remodelling. In a mouse model of bleomycin-induced fibrosis, Gal-3 was found to be overexpressed. [104] Furthermore, in a Gal-3 knock-out mouse model, a protective effect against bleomycin-induced fibrosis was observed in comparison to wild-type mice. [105] Gal-3 has also been found to be overexpressed in the serum of IPF patients, as well as in broncho-alveolar lavage fluid, and in patients undergoing acute exacerbations. [106]

Given the growing evidence supporting the involvement of Gal-3 in fibrosis and its intrinsic potential as a biomarker in fibrotic disease including IPF, Gal-3 represents a promising candidate for IPF therapy. Two oral drugs are currently approved for the treatment of IPF: Pirfenidone and

Nintedanib. However, the adverse effects associated with these drugs often lead to treatment being discontinued. [106]

To specifically bind to the Gal-3 protein, an HA derivative linked to a β-galactose, was developed. This HA-based polymer, named **HYLACH®**, offers improved biocompatibility compared to the currently available therapeutic options, combined with the ability to sequester Gal-3, thereby modulating fibrosis in lung disease.

HA is a natural biopolymer that provides biocompatibility, biodegradability, and low immunogenicity. It plays a role in tissue hydration and elasticity thanks to its high-water retaining capacity, and viscoelasticity properties. In addition, HA interacts with the cell receptor CD44, triggering biochemical processes including cellular growth, proliferation, migration and adhesion, wound healing, and tumour metastasis.

A wide range of HA-based materials have been synthesised using various chemical methods, in the form of conjugated or cross-linked HA to enhance, modulate and control of its therapeutic action. [8]

Some of the challenges of HA derivatisation include overcoming its limited solubility in organic solvents, and its sensitivity to harsh reaction conditions such as acidic or alkaline environments, or oxidative and thermal stress. Nevertheless, functionalised HA is widely used in several pharmaceutical applications. [107]

Functionalization of HA to generate HYLACH® involves derivatisation with the lactose analogue moieties (D-gal β(1-4)-D-Glc) consisting of 1-amino-1-deoxy-lactitol (**LAC-NH_2**), covalently bound to the carboxylate groups of HA via an amide bond. Functionalising HA in this way with LAC-NH_2 ensures the β-D-configuration of the galactose ring is retained, thereby maintaining the possibility of interaction with Gal-3. HYLACH® has already been reported to attenuate macrophage-induced inflammation and inhibit Gal-3 expression among other ECM proteins, while also exhibiting antioxidant effects. [108] Additionally, HYLACH® has been demonstrated to be superior to HA in reducing the gene and protein expression of fundamental profibrotic molecules. [109]

3.2. Materials and methods

3.2.1. Materials

HA samples, nominal molecular weight average of 90 kDa and 400 kDa were provided by HTL Biotechnology Javene (France). 4-(4,6-dimethoxy-1,3,5-triazin-2-yl)-4methyl morpholinium chloride (DMTMM), α-D-lactose, ammonium hydroxide solution 28-30%, sodium cyanoborohydride ($NaCNBH_4$), ammonium acetate (NH_4OAc), Amberlite® IR-120, hyaluronidase from bovine testes (HYAL), Phosphate Buffered Saline (PBS) and 2-mercaptoethanol (βME) were purchased from Sigma-Aldrich (Milan, Italy) and used without further purification. Deuterium oxide (99.9%) was purchased from CortecNet (Les Ulis, France) and deionized water (conductivity less than 0.1 μS) was prepared with an osmosis inverse system (Culligan, Milan, Italy). Filters (0.22 μm) were purchased from VWR (Milan, Italy). Lyophilized recombinant human galectin-3 was provided by Cell Guidance System (Cambridge, UK, 10 mM sodium phosphate, 50 mM sodium chloride, pH 7.5).

3.2.2. Synthetic procedure

3.2.2.1. Synthesis of 1-amino-1-deoxy-lactitol (LAC-NH_2)

One equivalent of α-D-lactose was solubilized in a saturated 0.05M NH_4OAc/EtOH solution, (18 mg/mL), at 40°C for about 30 min. 130 eq. of 28-30 % aqueous ammonia were added to the mixture, followed by the addition of 3 equivalents of $NaCNBH_3$. The reaction mixture was left under stirring at 90°C. After 8 hours the solvent and the excess of ammonia were evaporated under reduced pressure to provide a white solid residue, which was washed with H_2O and EtOH. The crude product, solubilized in H_2O, was loaded onto an Amberlite IR-120 (H^+) column (20 equivalents of resin compared to amine) and eluted with deionized water until neutral pH to remove all the inorganic salts. During this step, the primary amine product remained anchored to the resin and was liberated during elution with 50 mL of 10 % aqueous ammonia solution and 50 mL of water. The products were detected using a TLC plate, with charring in 10 % (v/v) sulfuric acid/EtOH. The collected product was then air-dried. The resulting residue was treated first with water and subsequently with EtOH until a constant weight was obtained to give a white solid product, with a yield of 90%.

3.2.2.2. Amidation with DMTMM

One equivalent of HA (nominal molecular weight of 90 kDa and 400 kDa) was dissolved in deionized water at a concentration of 8 mg/mL. 4-(4,6-dimethoxy-1,3,5-triazin-2-yl)-4-methylmorpholinium chloride (DMTMM) (1-2.5 eq.) was added as a powder. To this solution, 1-

2.5 eq. of a 1-amino-1-deoxy lactitol dissolved in water (40 mg/mL) was added (pH was measured and brought in a range of 6-7, when necessary, by addition of HCl 1M solution). The reaction was stirred at room temperature for 48 h.[110] The entire reaction mixture was poured into isopropanol (up to a final concentration of 80% (isopropanol/H_2O 8/2, v/v). The white solid was recovered after centrifugation and washed several times with isopropanol. The product was further purified by either dialysis or ion-exchange. For the dialysis method, the crude product was dissolved in a minimal quantity of deionized water and dialyzed (Spectra/Por® 1 dialysis membrane, cut-off 6-8 kDa) in 0.1M NaCl for 24 h, followed by 24h in deionized water. The product was further concentrated to a small volume under reduced pressure and freeze-dried. In the ion-exchange resin method, after precipitation, the crude product was dissolved in deionized water (to a concentration of 10 mg/mL) and gently stirred with Amberlite IR-120 (H+) (30 equivalents of resin per amine) at room temperature for 30 mins. The solution was then filtered through a glass-sintered funnel (porosity G3), and the resulting solution was neutralized by addition of 5% $NaHCO_3$, concentrated and lyophilized.

3.2.2.3. General procedures of enzymatic hydrolysis

HA and HYLACH® samples were solubilized in deionized H_2O, at a concentration of 8 mg/mL, at 37 °C and stirred until completely dissolved. HYAL (10 mg/ml in H_2O) was added for a final HYAL:HA ratio of 1:20 (w/w). To study the kinetics of hydrolysis, different timepoints (30', 1h, 2h, 4h and 24h) were considered. At prefixed timepoints, samples were taken and heated to 100°C for 15 minutes, to allow for HYAL denaturation, and filtered under vacuum (Filter c/o 0.22 μm) OHY and OHA hydrolyzed sample solutions were freeze-dried for NMR, HP-SEC-TDA characterization and for molecular interaction analysis with Gal-3.

3.2.3. Characterization

3.2.3.1. IR spectroscopy

The IR spectra of HA and two HYLACH® samples (HYLACH® 1 and HYLACH® 5) were recorded at room temperature suing an Alpha spectrophotometer (Bruker). The spectra were acquired in the range of 4000-400 cm-1 using the attenuated total refraction (ATR). Resolution was set to 4 cm-1 with 100 sample and background scan. Raw data were processed with OPUS software version 7.0 (Bruker).

3.2.3.2. NMR spectroscopy

Proton NMR spectra were recorded at 313K on a Bruker AVANCE NEO spectrometer operating at a proton frequency of 500MHz (Bruker, Karlsruhe, Germany), equipped with 5 mm TCI

cryoprobe. Carbon spectra were collected using a Bruker AVANCE IIIHD spectrometer operating at a proton frequency of 500 MHz (Bruker, Karlsruhe, Germany), equipped with 5mm BBO probe, at 313K. To prepare the samples, HA and HYLACH® were dissolved in D_2O to achieve a final concentration of approximately 10 mg/mL, while hydrolysed products were dissolved to a final concentration of about 30 mg/mL. The samples were stirred for at least two hours to ensure complete solubilization, before being transferred to 5mm NMR tubes, (Bruker, Karlsruhe, Germany).

^{1}H-NMR were acquired with presaturation of residual HOD, using the Bruker "zgcppr" pulse programme, with the following parameters: number of scans16, relaxation delay 12s, time domain 32k points and a spectral width of 18 ppm with transmitter offset ppm 4.7. Heteronuclear Single Quantum Correlation experiments (HSQC) were acquired using the Bruker hsqcedetgpsisp2.2 pulse program, with GARP4 decoupling. The following acquisition parameters were set: 32 number of scans, 16 dummy scans, relaxation delay 2s, time domain 1k, spectral width 10 ppm (F2) and 160 ppm (F1), transmitter offset ppm 4.7 (F2) and 90 ppm (F1), and number of t1 increments equal to 320. The $^{1}J_{C\text{-}H}$ tune value was set to 150 Hz.

Heteronuclear Multiple Bond Correlation (HMBC) spectra were acquired using the Bruker "hmbcetgpl2nd" pulse programme, with the following parameters: number of scans 32, dummy scan 2, relaxation delay 2s, time domain 2K and number of t1 increments equal to 256, with a long-range coupling of 8 Hz, spectral width 10 ppm (F2) and 160 ppm (F1), transmitter offset ppm 4.7 (F2) and 90 ppm (F1). Heteronuclear Single Quantum Coherence- Distortion Enhancement by Polarization Transfer (multiplicity-edited HSQC) were acquired using Bruker hsqcedetgpsisp2.2 pulse programme, with the following parameters: number of scans 48, dummy scan 16, relaxation delay 2s, time domain points 2K, spectral width 10 ppm (F2) and 160 ppm (F1), transmitter offset ppm 4.7 (F2) and 90 ppm (F1). HSQC and HMBC spectra were acquired using the phase-sensitive mode, by using the proportional phase incrementation.

COSY spectra were acquired using the Bruker "cosygpprqf" pulse programme with water presaturation, with the following parameters: number of scans 20, relaxation times 2s, time domain 20k, t1 increments 256 and spectral width 10 ppm (F2) and 10 ppm (F1), with transmitter offset 4.7 ppm.

The TOCSY spectra were acquire with Bruker "mlevphpr" pulse programme, with the following parameters: number of scans 20, relaxation times 2s, time domain 20k, mixing time 80 ms, spectral width 10 ppm (F2) and 10 ppm (F1), with transmitter offset ppm 4.7.

^{13}C spectra were acquired with Bruker pulse sequence zgig, with the following parameters: number of scans 24k, dummy scans 4, relaxation delay 2s, time domain 33k, and a spectral window of 300 ppm, transmitter offset 90 ppm.

Spectra were processed with Bruker Topspin Software 4.1.1.

3.2.3.3. High performance size exclusion chromatography (HP-SEC/TDA)

The molecular weight distributions were determined by HP-SEC/TDA, widely used for the analysis of polymers, [111] [31] without column calibration. Chromatographic acquisitions were performed on a Viscotek system model TDA305 (Malvern Panalytical. Malvern, UK) equipped with a multi-detector system (Refractive Index (RI), Right and Low Angle Light Scattering (RALS and LALS) and Viscometer (DP)). Sample solutions were obtained solubilizing 20-25 mg in a suitable volume of mobile phase and mixing for 3h. HA or HYLACH® were analysed at a concentration of ~0.5 mg/mL, while hydrolysed products were at a concentration of ~4 mg/mL. Measurements were performed at 40°C, at a flow rate of 0.6mL/min, using 2 x TSKGMPWXL columns 13 μm. 7 mm ID x 30 cm L, in series (Tosoh Bioscience, Japan). A solution of 0.1 M $NaNO_3$ containing 0.05% of NaN_3, prefiltered using a 0.22 μm filter (Millipore Merck, Milan, Italy) was used as mobile phase. The detectors were calibrated with Pullulan standard, with molecular weight, polydispersity index and intrinsic viscosity certified (PolyCAL-Pullulan STD-Malvern Panalytical, UK). Chromatographic profiles were elaborated using OmniSEC software version 4.6.2. For all the samples the refractive index increment (dn/dc) of 0.155, known in literature for HA, was used. [112]

3.2.3.4. Electrospray ionization mass spectroscopy (MS-ESI)

Direct infusion ESI-MS analysis, of LAC-NH_2, was performed on an Impact II ESI-Q-TOF mass spectrometer (Bruker Daltonics, Karlsruhe, Germany). The spectrum was acquired in positive ion mode (capillary voltage -4.5 kV) in the m/z 50 - 1300 mass range. Nitrogen was used as a drying (4L/min) and nebulizing gas (0.4 bar) and the ion transfer capillary was kept at 200°C.

3.2.3.5. Isothermal titration calorimeter (ITC)

Biomolecular interactions were determined by ITC analyses, performed on a MicroCal PEAQ-ITC, (Malvern Panalytical. Malvern, UK), equipped with MicroCal PEAQ-ITC Analysis Software. Gal-3 protein was reconstituted in a solution of PBS and β mercapto-ethanol at a concentration of 10 μM. Ligand solution of LAC-NH_2, galactose, lactose, HA and HYLACH® oligomers (labelled OHA and OHY, respectively) were solubilized in PBS buffer at different concentrations (between 295 to 400 μM). ITC experiments were carried out at 25°C. Two hundred μM of protein solution were loaded on the sample cell, while each ligand solution was loaded in the syringe. Two μL of ligand were injected twenty times, with a delay of 60 s and 150 s between injections, with the stirring rate set to 500 rpm. For each ligand injection, the measured heat released upon complex formation was fitted to a single binding site model using the following equation:

$$Q(i) = \frac{nP_t \Delta HV \left\{ 1 + \frac{X_t}{nP_t} + \frac{1}{nKP_t} - \left[\left(1 + \frac{X_t}{nP_t} + \frac{1}{nKP_t} \right)^2 - \frac{4X_t}{nP_t} \right]^{\frac{1}{2}} \right\}}{2} \quad (20)$$

Where Q(i) is the heat corresponding to the *i*th injection, V is the sample cell volume; ΔH is the enthalpy; [P t] is the cell protein concentration; [Xt] is the syringe ligand concentration, n is the number of binding sites and K is the binding constant.

To estimate the thermodynamic parameters (K_D, ΔH and ΔS), the data were fitted using MicroCal analysis software using the 'One set of sites' interaction model. Blank experiments on the free ligands diluted in PBS and β-mercaptoethanol were recorded and the measured heat subtracted from the reaction heat data.

3.2.3.6. Circular dichroism (CD) spectroscopy

Circular dichroism analyses were performed on a J1500 Circular Dichroism Spectrophotometer, (Jasco, Mary's Court, Easton, USA) and raw data were elaborated with Jasco Spectra Manager Software. Gal-3 protein was prepared as indicated in the ITC experimental method section at a final concentration of 10 μM, and 200 μL were employed for every ligand tested (lactose, LAC-NH_2 and oligomers of HA, HYLACH® 1 and HYLACH® 2). Ligand stock solutions were solubilized in PBS to obtain 2.94 mM concentration. Circular dichroism spectra were collected at 25 °C and recorded using a quartz cell (Hellma UK), with a path length of 1 mm, response time of 1s, scan speed of 20 nm/min, and bandwidth of 0.5 nm, and each spectrum was built from the average of three scans. For each CD measurement, a titration of the ligand into the protein was performed. Far CD-UV spectra (200-250 nm) were recorded for at least eleven ligand/protein molar ratios (L/P), in the range 0 to 8. Spectra of the free ligands were recorded under the same conditions as the blank, and the CD signals were subtracted from the protein-ligand complex signals.

3.3. *Results and discussion*

3.3.1. *LAC-NH_2 synthesis and characterization*

1-amino-1-deoxy lactitol, or LAC-NH_2, was prepared by the reductive amination of lactose, employing the metal hydride/ammonia mediated reductive amination of hemiacetals. [110] The protection-group-free synthesis of primary amine favours a one-step chemo-selective preparation of primary amine LAC-NH_2, as described in *Figure 3-1*.

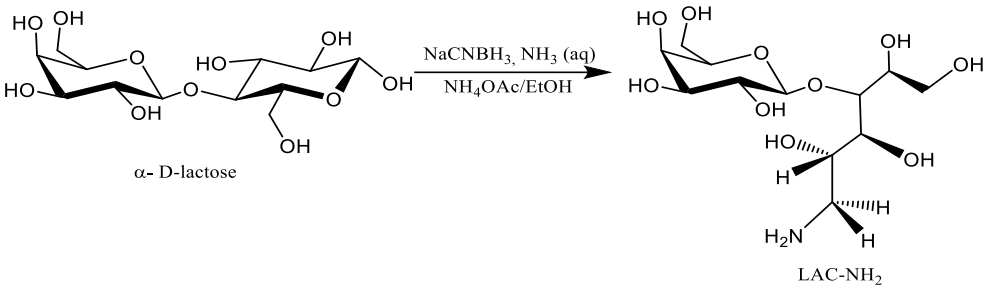

Figure 3- 1: ***LAC-NH_2 synthesis***

The structure of the product was confirmed by homonuclear, and heteronuclear NMR experiments (*Figure 3-2* and *Table 3-2*) and the complete proton and carbon signal assignments are in agreement with the literature. [113]

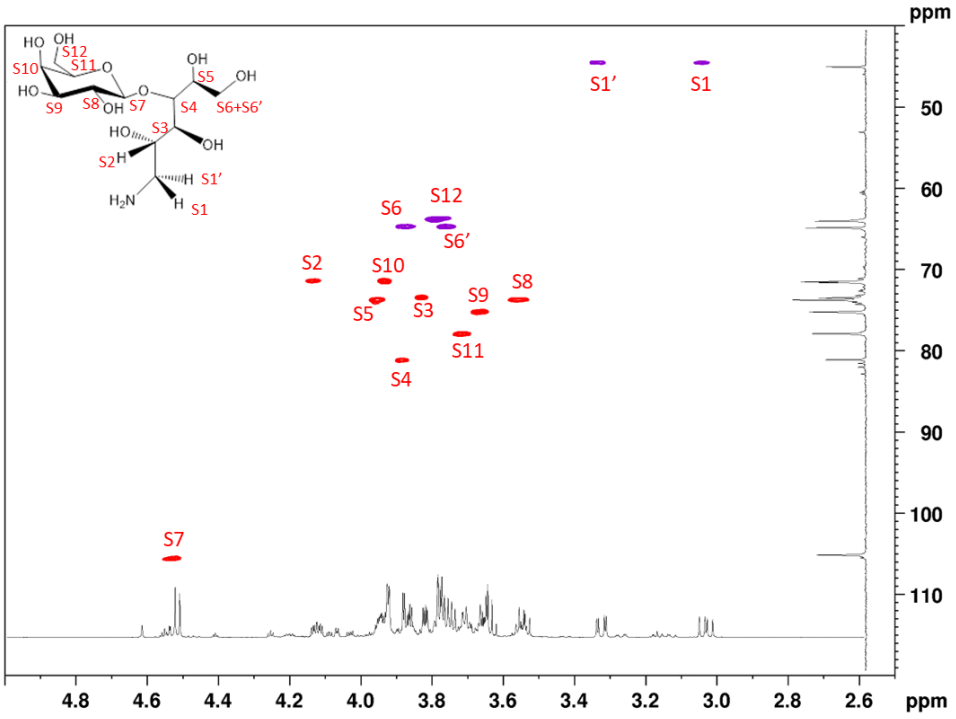

Figure 3- 2: ***HSQC DEPT of LAC-NH_2.*** *Assignment of signals of LAC-NH_2 in the HSQC-DEPT spectra (Red-purple), with proton and carbon spectra.*

Table 3- 1: ***Full assignment of NMR signals (1H, 13C) of LAC-NH2***

Assignment	^{1}H (ppm)	^{13}C (ppm)
S1+S1'	3.38-3.05	44.7
S2	4.15	71.4
S3	3.84	73.4
S4	3.88	81.2
S5	3.96	73.7
S6+S6'	3.89-3.77	64.8
S7	4.53	105.7
S8	3.56	73.8
S9	3.67	75.2
S10	3.94	71.5
S11	3.75	78.0
S12+S12'	3.80	64.1

Further confirmation of the synthesized LAC-NH_2 structure was obtained using mass spectroscopy that shows the presence of a peak at m/z 344 ($M+H^+$), corresponding to the molecular weight of LAC-NH_2 ($C_{12}H_{25}NO_{10}$), as reported in *Figure 3-3*.

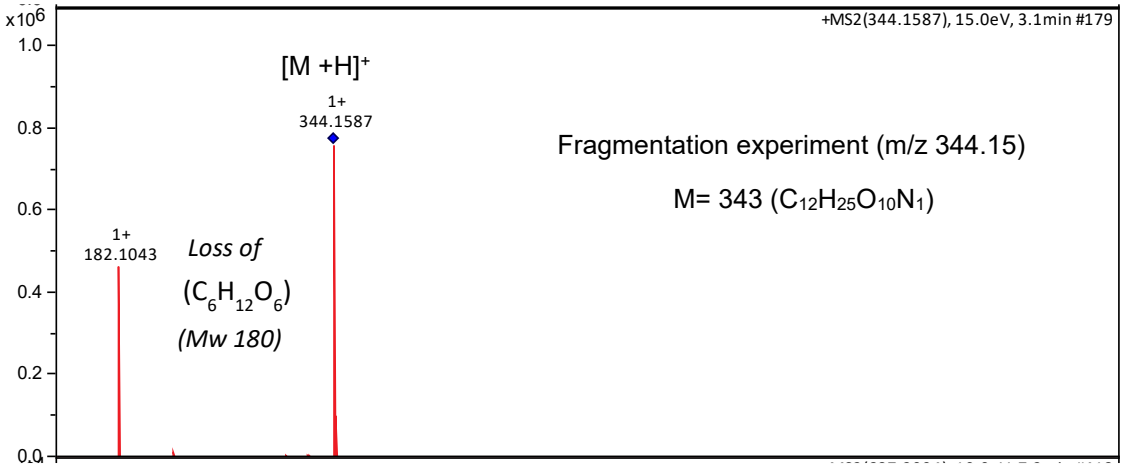

Figure 3- 3: ***Mass spectra (ESI) of LAC-NH2***

3.3.2. HYLACH® synthesis

HYLACH® was obtained by reaction between HA and LAC-NH_2, in which the amino-lactose derivative is covalently conjugated to the HA. This reaction results in the formation of an amide bond between carboxylic groups of the GlcA residue of HA and amine of LAC-NH_2, as illustrated in *Figure 3-4*.

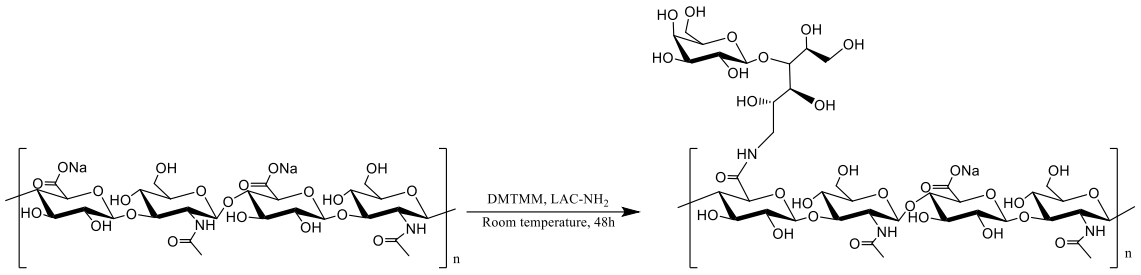

Figure 3- 4: ***Synthesis of HYLACH®***

The synthesis has been performed to obtain compounds with a degree of substitution (DS) between 10% and 40%, which were found to provide better results in preliminary in silico studies. [108] The syntheses were performed in aqueous media, in the presence of a commercially available condensing agent, DMTMM, [114] known to be highly soluble and stable in water for an extended period of time. [115] This allows the formation of an ammonium salt of DMTMM which reacts, by a substitution mechanism, with the carboxylic group of HA to form the active triazine-ester followed by a nucleophilic attack of LAC-NH_2. [8]

To synthesize samples with different DS values in a range considered ideal according to previous biological evaluation [108], various reaction parameters, such as stoichiometry of the triazine condenser (DMTMM) and LAC-NH_2, and pH, were optimized. Reactions were carried out on both the nominal molecular weight 90 kDa and 400 kDa HA, at different scales, from mg to g. A summary of the reaction conditions is reported in Table 3-2. HYLACH® samples were obtained, in quantitative yield, after a purification step involving precipitation in isopropanol (80%), performed following dialysis or ion exchange as described in §3.2.2.2. No significant difference between ion exchange and dialysis methods was observed.

Table 3- 2: ***Reaction conditions for the preparation of HYLACH®.***

HYLACH® Sample	Starting HA (Mw, kDa)	Reaction conditions		
		LAC-NH_2 (eq.)	DMTMM (eq.)	pH
HYLACH® 1	90	0.5	0.5	≈7
HYLACH® 2	90	1.5	1.5	≈7
HYLACH® 3	90	1.5	1.5	>8
HYLACH® 4	400	1.5	1.5	>8
HYLACH® 5	400	2.5	2.5	≈7

3.3.3. IR spectroscopy

Infrared spectroscopy is the method indicated in the EuPh and USP for the characterization of HA, see §1.4. The IR profile of HA and two of the functionalized HA (HYLACH® 5 and HYLACH® 1) are reported in *Figure 3-5*.

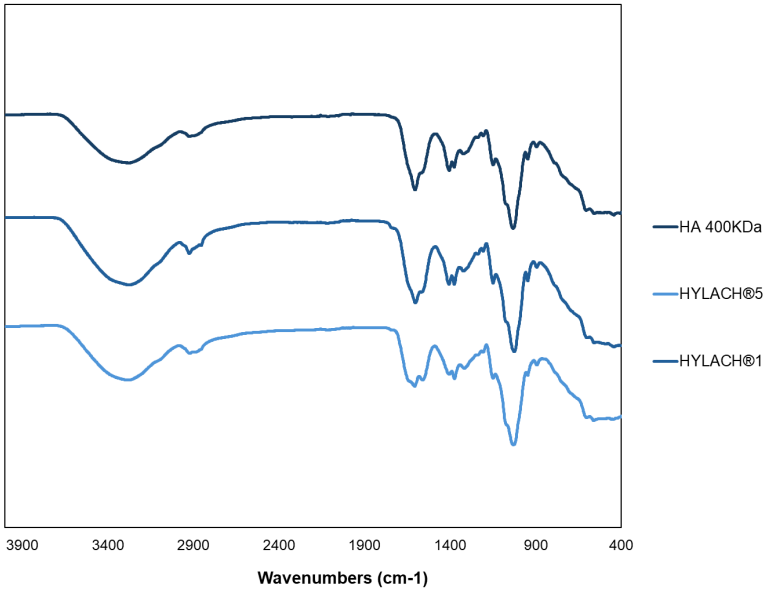

Figure 3- 5: ***IR spectra of HA, HYLACH®1 and HYLACH®5***

The IR spectra are similar, and any significant differences could be observed between the HA and its functionalized samples, particularly in the carbohydrate regions (1280-900 cm^{-1}).

3.3.4. NMR spectroscopy

The characterisation of HYLACH® samples was challenging due to its large and complex structure, requiring advanced NMR techniques. HYLACH® products were analysed using NMR spectroscopy with one-dimensional (^{1}H and ^{13}C) and two-dimensional (homonuclear COSY and heteronuclear multiplicity-edited HSQC and HMBC) experiments. The ^{1}H NMR spectra of HYLACH® revealed the presence of peaks corresponding to LAC-NH_2, but no significant changes in chemical shift were observed following functionalisation. The successful conjugation of HA with LAC-NH_2 was confirmed exclusively by the HMBC experiment, which indicated the formation of an amide bond (*Figure 3-6*). TOCSY and COSY spectra enabled the full assignment of the proton signal at position 2. Through H–H correlations, all other proton signals within the sugar rings and the LAC-NH_2 residue were subsequently assigned (*Figure 3-7*).

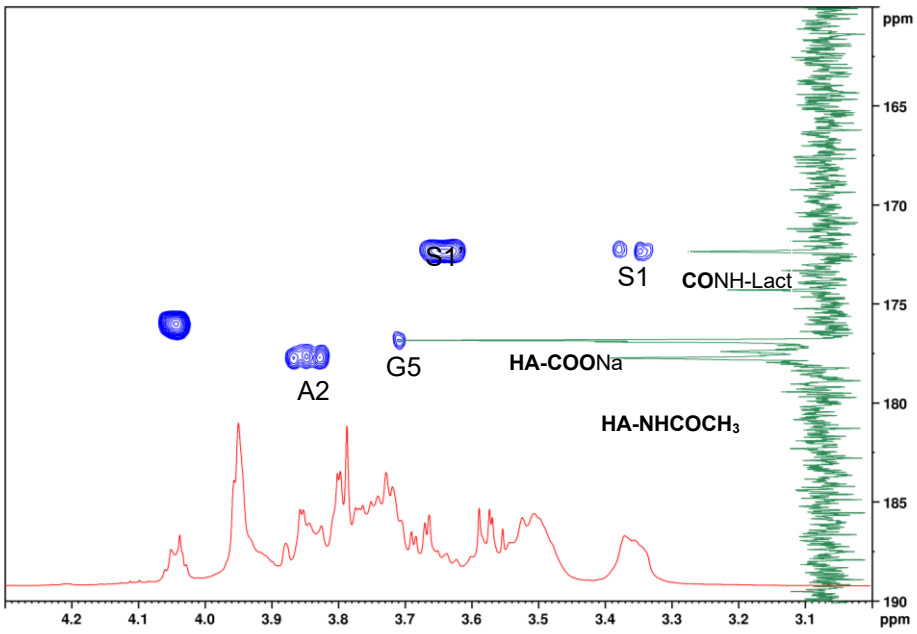

Figure 3- 6: ***HMBC of HYLACH®.*** *In blue is the HMBC spectrum, the ^{1}H spectrum in red and ^{13}C spectrum in green.*

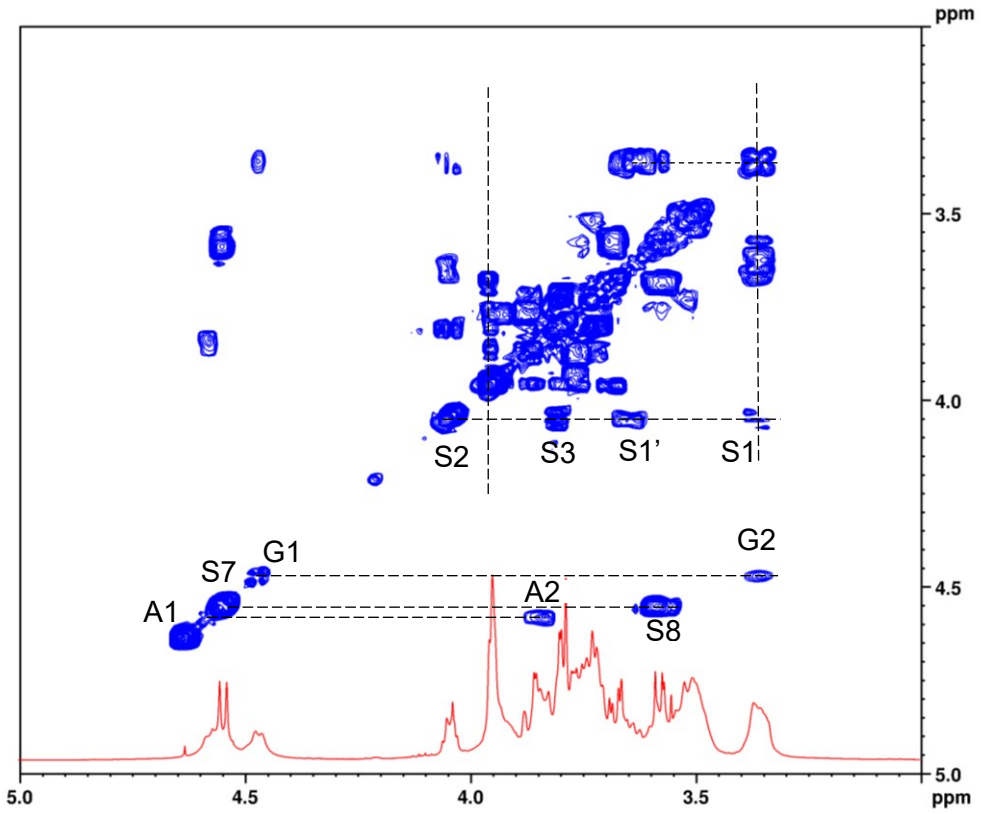

Figure 3- 7: ***COSY and ^{1}H spectra of HYLACH®****. In blue reported the COSY spectrum, the ^{1}H spectrum in red.*

*Figure 3-8 s*hows a typical ^{1}H-^{13}C HSQC spectrum of HYLACH®, while its chemical shift values are listed in *Table 3-4.*

Table 3- 3: ***^{1}H and ^{13}C chemical shift of HYLACH®***

Assignment	^{1}H (ppm)	^{13}C (ppm)
Ac(CH_3)	2.03	25.2
A1	4.57	103.2
A2	3.84	57.1
A3	3.72	85.5
A4	3.52	71.2
A5	3.50	78.2
A6	3.92	63.4
A6’	3.77	63.4
G1	4.47	105.8
G2	3.35	75.2
G3	3.58	76.4
G4	3.74	82.7
G5	3.73	79.1
S1	3.36	44.8
S1’	3.62	44.8
S2	4.04	72.7
S3	3.80	73.1
S4	3.95	82.4
S5	3.94	74.1
S6	3.86	64.8
S6’	3.76	64.8
S7	4.54	105.8
S8	3.57	73.9
S9	3.68	75.4
S10	3.95	71.3
S11	3.72	78.0
S12-S12’	3.79	63.8
CONH	-	172.3
COO^{-}	-	176.8
Ac(CO)	-	177.7

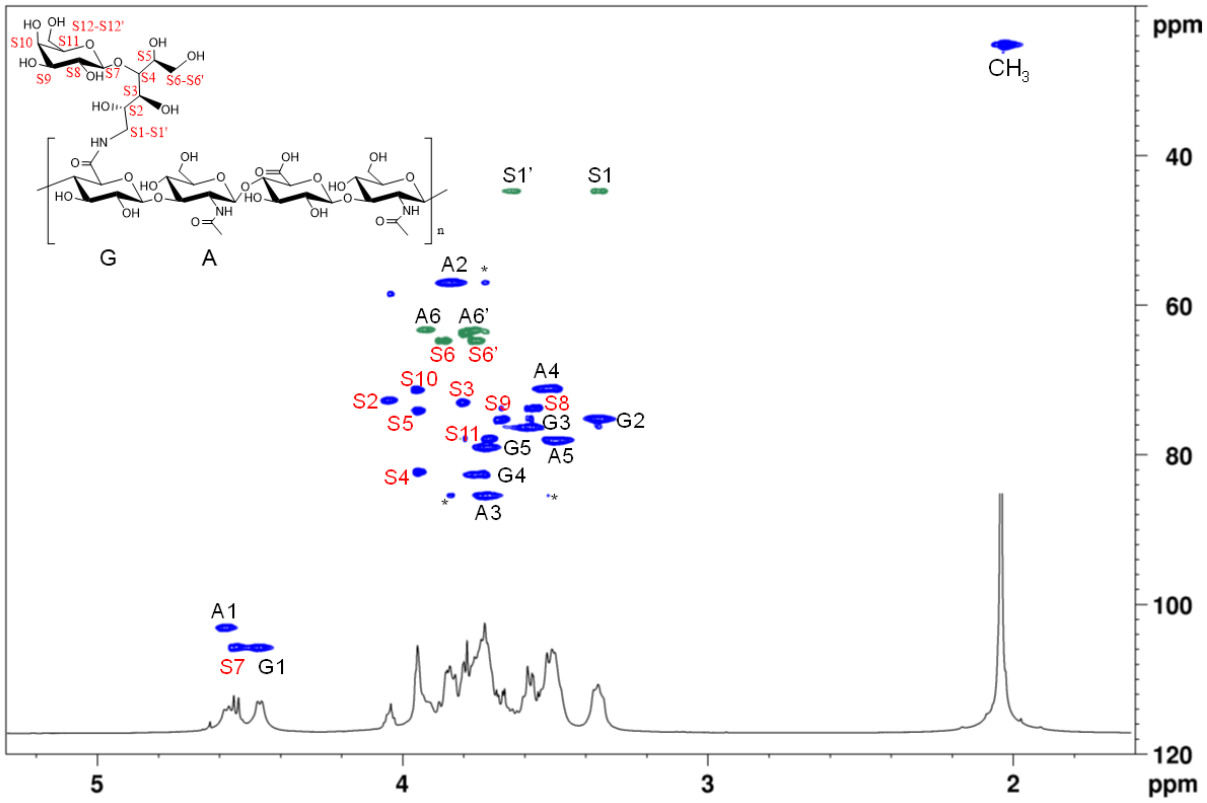

Figure 3- 8: ***Assignment of HYLACH® ^{1}H and ^{13}C NMR signals****. Superimposition of ^{1}H-^{13}C HYLACH® HSQC-edited (CH_2 are reported in green and CH and CH_3 signals in blue) and ^{1}H spectrum.*

3.3.5. Determination of the degree of substitution

The literature reports that ^{1}H NMR spectra are usually used to evaluate the degree of substitution (DS) of functionalized HA, integrating ligand signals with respect to the CH_3 groups of GlcNAc [116] [117]. Due to the complexity of the ^{1}H NMR spectra of the samples and the absence of a clear, well-resolved proton signal corresponding to LAC-NH_2, this method could not be applied to HYLACH®. Additionally, signal integration from other one-dimensional experiments, such as ^{13}C and ^{14}N NMR, proved to be ineffective.

In HSQC experiments, the presence of a well-defined CH signal of S2 of LAC-NH_2 separated from the other signals of the backbone, was observed. Since in the literature, quantitative 2D-HSQC analysis applied to different polysaccharides such as sulodexide,[118] heparin [119] and pentosan polysulphate [31] are reported, the determination of DS of HYLACH® through two-dimensional NMR spectra was attempted. The huge differences in molecular size and mobility between the backbone of polysaccharide and the pendant disaccharide, however, led to different longitudinal relaxation time (T_1) and transverse relaxation times (T_2), especially for ^{13}C nuclei, influencing the integral measurements and subsequent results. This behaviour is more evident for HYLACH® compounds obtained from HA of 400 kDa, in which DS values higher than 100%,

determined by 2D NMR, were found. To overcome this problem, enzymatic depolymerization of the polysaccharide was introduced to reduce molecular weight without affecting the substitution and consequently the motional behaviour difference between the HA oligomers and the amino-lactose branching. Hydrolysis of HA and HYLACH® derivatives were performed with hyaluronidase type I [13], [120]. The mechanism of depolymerization involves the cleavage of β 1→4 glycosidic bonds, leaving intact the amide bond with LAC-NH_2.

The mechanism of hydrolysis is shown in *Figure 3-9*.

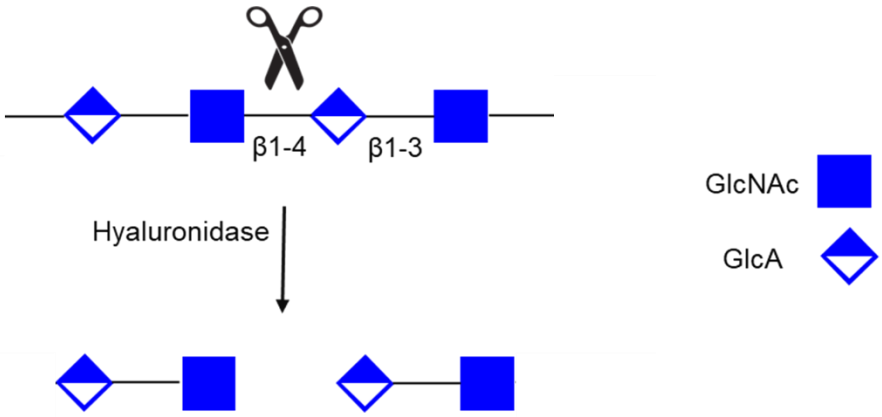

Figure 3- 9: ***Hyaluronidase mechanism of hydrolysis***

As reported in the literature, [121] hydrolysing HA to its constituent disaccharides in a selective manner remains challenging, primarily due to the dual enzymatic activity of hyaluronidase, which exhibits both hydrolytic and transglycosylation functions.

In this study, HA oligomers exhibited an average Mw of approximately 5 kDa after 24 hours of enzymatic depolymerisation at neutral pH and in the absence of salts — conditions required for subsequent NMR analysis. HYLACH® oligomers, meanwhile, ranged between 6 and 14 kDa. Distinct from HYLACH®, the HSQC spectrum of hydrolysed HYLACH® oligomers (*Figure 3-10*) exhibits the presence of reduced anomeric signals attributed to reducing end GlcNAc H1α and GlacNAc H1β (indicated as A1α-r and A1β-r), as well as reducing GlcNAc 2 (A2α-r and A2β-r) compared to starting HYLACH®. The DS, expressed as the percentage of substituent compared to HA disaccharide repetitive units, was obtained according to the following formula *21*:

$$DS = \frac{(S2)}{(A2 + A2\beta - r. + A2\alpha - r)} \cdot 100\% \qquad (21)$$

Where S2 integral value, shown in *Figure 3-10*, is divided by the sum of A2 and A2 (reducing end) signals.

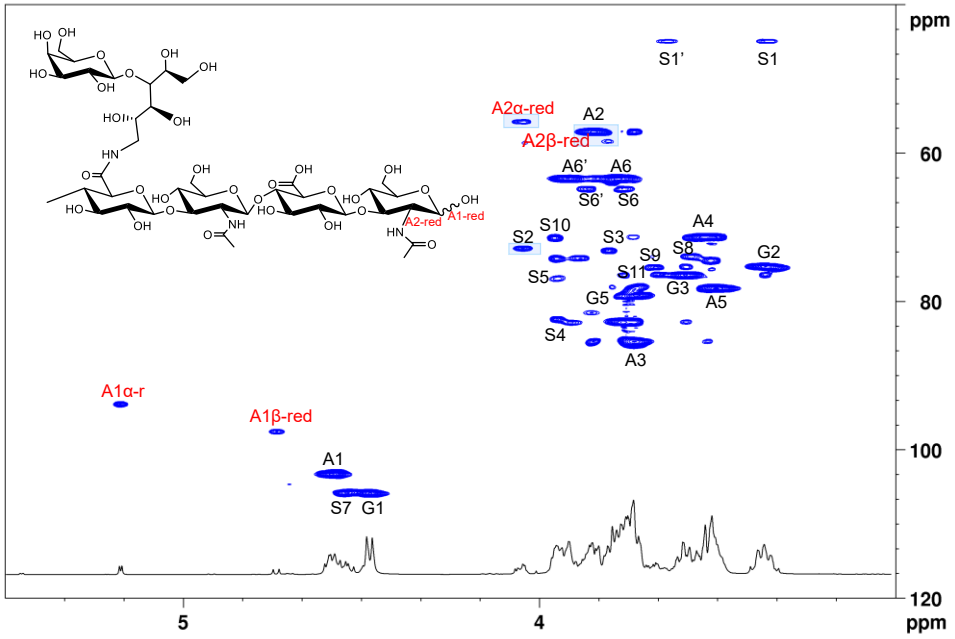

Figure 3- 10: ***2D NMR spectroscopy for the determination of the degree of substitution****. Superimposition of ^{1}H-^{13}C HSQC and ^{1}H spectra of hydrolysed HYLACH® sample. The signals integrated for the calculation of the DS are highlighted in light blue.*

Investigation of the correlation between Mw and DS during a kinetic hydrolysis, led to DS being properly estimated through quantitative 2D-HSQC spectra, when the HYLACH® oligomers were in a Mw range between 6 and 20 kDa. DS values obtained as a function of the stoichiometry ratio of reagent and pH, were in the range between 14 to 44% for all the synthetized HYLACH® (*Table 3-5)*. Additionally, it was observed that the repetition of the same synthesis led to the same DS.

Table 3- 4: ***HP-SEC/TDA and DS results of HA and HYLACH® samples***

Samples	Starting HA (kDa)	DS%	Mw (kDa)	Mn (kDa)	Mw/ Mn	Rh (nm)	η (dl/g)	a	logK
90 kDa HA	-	-	82	58	1.4	14	2.4	0.88	-3.9
HYLACH® 1	90	**14**	86	66	1.4	14	2.2	0.85	-3.9
HYLACH® 2	90	**37**	95	68	1.5	13	1.6	0.79	-3.7
HYLACH® 3	90	**23**	89	63	1.5	14	2.0	0.78	-3.5
400 kDa HA	-	**-**	325	209	1.5	33	7.5	0.76	-3.3
HYLACH® 4	400	**18**	260	170	1.5	27	5.5	0.80	-3.6
HYLACH® 5	400	**44**	280	174	1.6	25	3.9	0.77	-3.6

Starting HA indicate the nominal Mw of the HA, DS (%) determined by formula 1; Mw: weight-average molecular weight; Mn: number-average molecular weight; Mn/Mw: Molecular-weight dispersity; Rh: Hydrodynamic radius; η: viscosity; *a* and logK: Mark-Houwink costant;

An increase of LAC-NH_2 compared to HA leads to higher DS values, HYLACH® **1** (0.5 eq.; DS=14 %) towards HYLACH® **2** (1.5 eq.; DS=37 %), while a pH higher than 8, leads to lower DS as observed for HYLACH® **3** (23%) compared to HYLACH® **2** (DS: 37 %). Analogous results were obtained for HYLACH® **4,** DS 18% and HYLACH® **5**, 2.5 eq., DS: 44%, obtained under different reactions conditions.

3.3.6. *Molecular Weight Distribution*

The chromatographic profiles of 90 kDa and 400 kDa HA, overlapped with their derivatives (HYLACH®1 and HYLACH®4, respectively), are shown in *Figures 3-11* A and *3-11 B*, respectively.

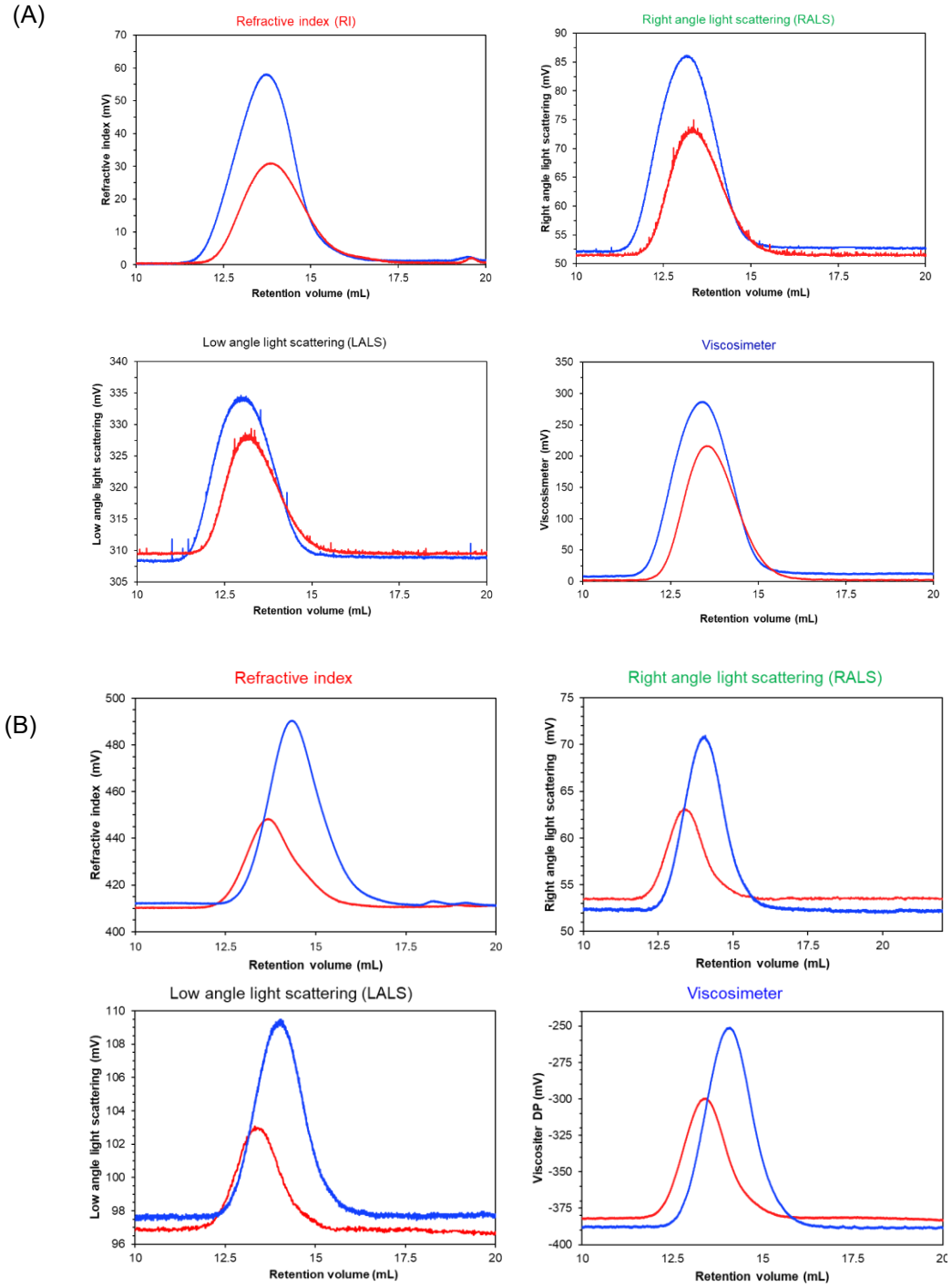

Figure 3- 11: ***HP-SEC-TDA profiles of HA and HYLACH.*** *RI, DP, LALS and RALS of A) 400 kDa HA (red) and HYLACH®4 (blue) and B) 90 kDa HA (red) and HYLACH®1 (blue).*

The samples had an elution volume between 12 and 16 mL, with a broad bell-shape chromatographic peak, caused by a high poly-dispersion index. Weight-average molecular weight (Mw), number-average molecular weight (Mn), and molecular-weight dispersity (Mw/Mn) values are reported in *Table 3-4*. In addition, values of hydrodynamic radius (Rh), intrinsic viscosity value (η), value of a and logK, corresponding respectively to the slope and intercept constants of the Mark-Houwink curve derived from HP-SEC-TDA, are also reported. All the results refer to the mean values of duplicate injections. HP-SEC-TDA profiles showed that HYLACH® at 400 kDa leads to partial hydrolysis of HA, not observed for the 90 kDa HA. On the other hand, the result of a blank experiment obtained using 400 kDa HA in the presence of DMTMM, and left stirred for 48h, revealed a reduction in Mw of HA of the same order of magnitude as HYLACH® samples (*Figure 3-12* and *Table 3-5*).

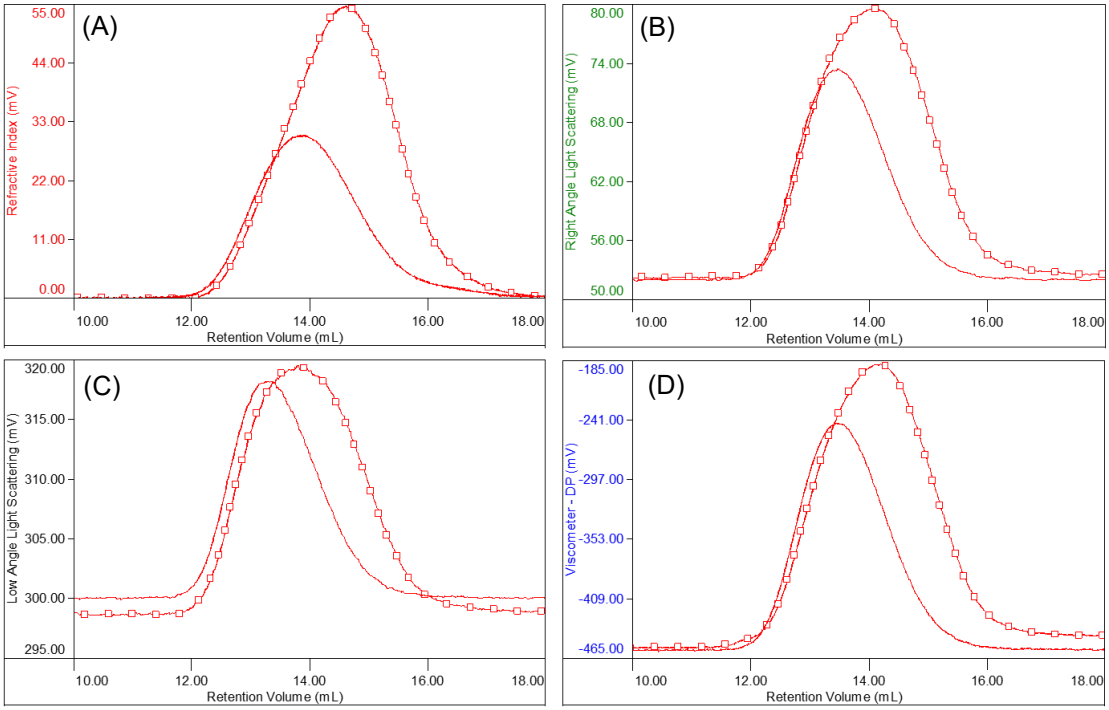

Figure 3- 12: ***HP-SEC/TDA profiles of HA with and without DMTMM.*** *In the image are reported (A) the refractive index (RI), (B) Right-angle light scattering (RALS), (C) Low-angle light scattering (LALS) and (D) Viscosimeter (DP) of HA 400KDa in presence of DMTMM (red) and a blank solution of HA (red and square), obtained after 48h in solution.*

Table 3- 5: ***HP-SEC-TDA results of HA with and without DMTMM.***

Sample	Mw (kDa)	Mn (kDa)	Mw/Mn	Rh (nm)	η (dl/g)	a	logK
HA*	325	209	1.5	33	7.5	0.76	-3.3
Blank of HA*	251	174	1.5	28	6.0	0.78	-3.4

*HA obtained after 48h in solution without DMTMM
**Blank obtained after 48h in solution in presence of DMTMM
Mw: weight-average molecular weight; Mn: number-average molecular weight; Mn/Mw: Molecular-weight dispersity; Rh: Hydrodynamic radius; η: viscosity; *a* and logK: Mark-Houwink costant;

Interestingly, this phenomenon was not observed in the absence of condensing agent. The Mw/Mn remains constant and similar to the starting HA, thus indicating that there is no increase in polydispersity after the functionalization of the HA. The hydrodynamic radius (Rh) for HYLACH® samples obtained from 90 kDa HA remains constant, while this value decreases for HYLACH® samples obtained from 400 kDa HA, due to the partial depolymerization occurring during the polymer derivatization. The intrinsic viscosity (η) of sodium hyaluronate is influenced by the Mw, as observed for the comparison of intrinsic viscosity values of 400 kDa HA and 90 kDa HA. This behaviour does not occur for HYLACH® samples, in fact, η values decrease with increasing Mw, possibly indicating that modification of the structure (different DS) induces different rheological properties. This variation could indicate a difference in intra- or inter-molecular interactions, [122] which alters the chemical properties of the polymers (manuscript in preparation). This phenomenon is also observed for HYLACH® at high molecular weight, despite the fact that depolymerization occurred during the functionalization reactions. *logK* and *a* have similar values and of the same order as data reported in the literature, [123] in addition, "a" values are in the range of 0.7- 0.9, thus indicating that, regardless of Mw and DS, the molecules remain in a random coil conformation. The weight recovery, determined by the refractive index area, is in a range between 81% and 94% for all the samples injected and this value is compatible with the water absorption by dry samples.

3.3.7. HYLACH® stability towards hyaluronidase

The hydrolysis procedure, for the determination of DS, allows the determination of HYLACH® stability towards hyaluronidase (HYAL) depolymerization. Hydrolysis curves over time are shown in *Figure 3-13*. From the hydrolysis curves, it is evident that 90 kDa HA presents a lower degree of enzymatic depolymerization than to 400 kDa HA. On the other hand, all HYLACH® samples, exhibited a degree of depolymerization lower than native HA, and inversely proportional to the DS (see *Table 3-4*).

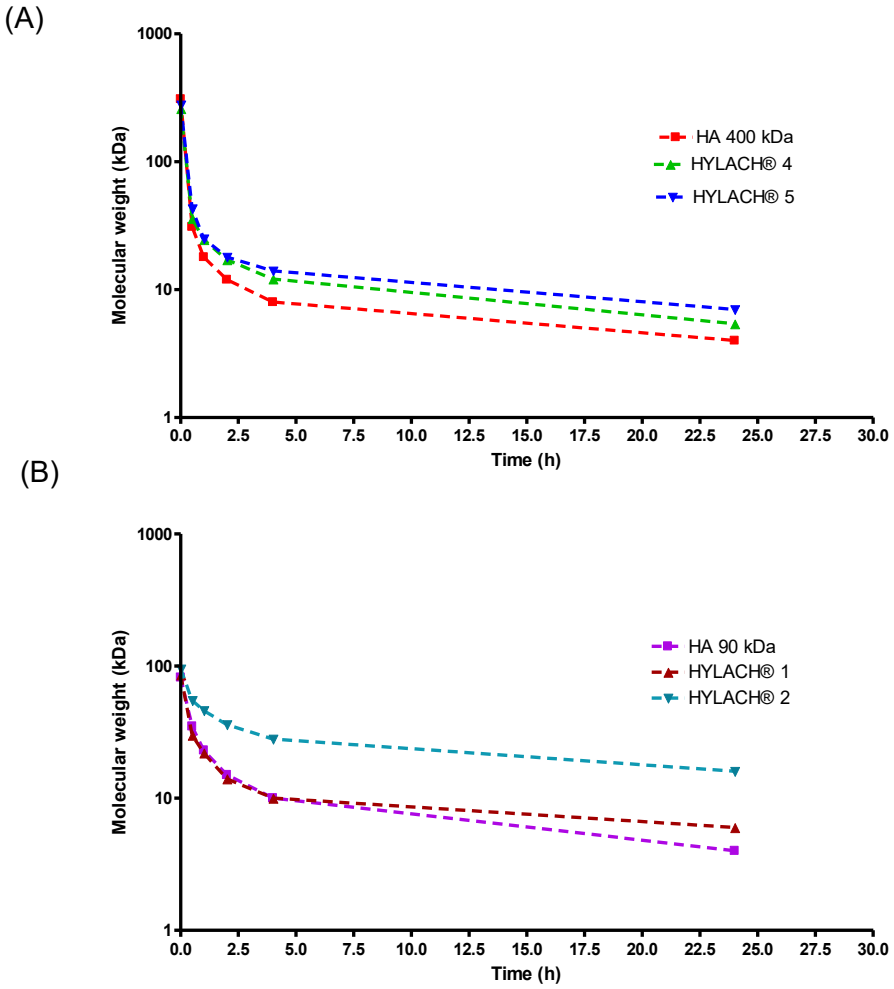

*Figure 3- 13**: Investigation of HYLACH® enzymatic stability**. Hydrolysis curves over time of; A) 400 kDa HA and its corresponding HYLACH® samples B) 90 kDa HA and its corresponding HYLACH® samples.*

3.3.8. Isothermal titration microcalorimetry

Isothermal titration calorimeter experiments were performed to address the interaction between Gal-3 and HA or HYLACH®. This sensitive technique measures the differential power, applied to the cell heaters, required to minimize the temperature difference between the reference and the sample cell. In addition, ITC has the advantages that it does not require labelling or immobilization of the ligands and can be performed in solution.

ITC interaction studies were performed on saccharide ligands and oligomers of HA (OHA) and HYLACH® (OHY1 and OHY2), obtained by enzymatical hydrolysis. The OHA and OHY were used instead of the whole polysaccharide owing to the challenges experienced in data interpretation and the establishment of a reliable binding model for polydisperse polymers. Additionally, high molecular weight polysaccharides such as HA exhibit high viscosity, which can hinder proper mixing during titration and negatively impact ITC measurements. Using

oligomers overcomes this limitation and minimizes viscosity differences between the native and functionalized HA samples.

OHY1 and OHY2 were selected due to the similarity of molecular weight and DS with HYLACH® 1 and HYLACH® 3 respectively, cited by Donato et al. [108]

The typical ITC profile achieve with the interaction OHA and OHY with Gal-3 is shown in *Figure 3-14*. The figure shows a saturable interaction, achieved at higher molar ratios, with an exothermic response during the early injections.

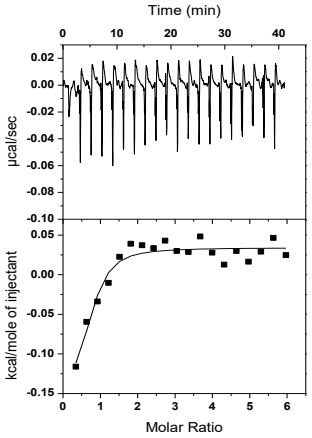

Figure 3- 14: ***ITC profile of Oligomer of HA (OHA-8kDa).*** *The upper panel shows the raw heat change (µcal/sec) over time during successive injections, while the lower panel displays the integrated heat per mole of injectant (kcal/mol) plotted against the molar ratio.*

The thermodynamic parameters obtained from the elaboration of the curve, such as the stoichiometry (N), dissociation constant (K_D), variation of enthalpy (ΔH), variation of Gibbs free energy (ΔG) and variation of entropy (TΔS), are reported in *Table 3-6.*

Table 3- 6: ***Thermodynamic parameters obtained by ITC for the interaction of HA and HYLACH® oligomers with Gal-3.***

Sample	***Mw (Da) (DS%)***	***N (sites)***	***K_D (µM)***	***ΔH (kcal/mol)***	***ΔG (kcal/mol)***	***TΔS (kcal/mol)***
LAC-NH_2	380	0.97 ± 0.12	9.24 ± 1.79	-4.49 ±0.83	-6.87	2.38
Galactose	180	1.29 ± 0.17	19.7 ± 3.46	-3.06 ± 0.63	-6.42	3.36
Lactose	340	1.37 ± 0.13	13.4 ± 2.41	-2.7 ± 0.43	-6.66	3.96
OHA	22 000	0.59 ± 0.03	1.55 ± 0.27	-0.22 ± 0.02	-7.93	7.71
OHA	8 000	0.73 ± 0.02	1.36 ± 0.16	-0.14 ± 0.05	-8.00	7.86
OHY1	6 000 (14%)	0.72 ± 0.04	1.91 ± 0.35	-0.18 ± 0.01	-7.81	7.63
OHY2	14 000 (37%)	0.85 ± 0.12	9.13± 1.63	-9.83 ± 1.87	-6.88	-2.95

OHA: HA oligomers, OHY: HYLACH® oligomers, Mw: molecular weight, DS: Degree of substitution express in %, *[L]:* Ligand concentration, N: number of sites; K_D: dissociation constant; ΔH*:* Variation of enthalpy**;** *ΔG:* Variation of Gibbs free energy*, TΔS:* Variation of Entropy,

ITC results showed that the interactions between Gal-3 and saccharide ligands, OHA and OHY are all energetically favourable binding reactions (ΔG negative) and entropically driven (TΔS>0), except for OHY 2. For small ligands (LAC-NH_2, galactose and lactose) the stoichiometry of the

interaction (N) is in the order of 1 protein:1 ligand, and the dissociation constant (K_D) is the order of μM, with values similar to data reported for lactose. [50], [124]–[128]

It was observed that both OHA and OHY exhibited equivalent behaviour in relation to galactose and lactose. However, significant disparities were identified in the K_D, which exhibited a higher order of magnitude. This finding suggests that the oligomer exhibits a higher binding affinity for the protein compared to the natural ligand. However, it is plausible that this phenomenon is partly driven by electrostatic interactions rather than solely by specific binding at the physiological site. OHA and OHY show the same behaviour of galactose and lactose, the major differences were found in the K_D, higher of 1 order of magnitude. This indicates that the oligomer binds to the protein with higher affinity than the natural ligand; however, this phenomenon may be partly driven by electrostatic interactions rather than solely by specific binding at the physiological site. To evaluate the influence of variation of Mw on protein interaction, OHA were studied at two molecular weights of about 8 kDa and 22 kDa. No significant difference in thermodynamic parameters of the binding was observed, suggesting that there was little variation with the molecular weight. Thermodynamic parameters revealed that the binding of HA to Gal-3 is characterized by hydrogen bonding and hydrophobic interactions as indicated by the higher favourable entropy contribution ($\Delta S > 0$). Similar binding affinity in the micromolar range and thermodynamic parameters were obtained in the binding of HYLACH® oligomers at lower DS (OHY 1). For both OHA and OHY the number of sites (N) is around 0.7, which means that 1 ligand is bound to 2 proteins, suggesting that full-length (recombinant) human Gal-3 protein might dimerize upon oligomer binding, as previously reported for multivalent carbohydrates that induce the self-association of Gal-3. [129]–[131] Interestingly, the binding of OHY 2 with higher DS (37%) showed a different feature, as indicated by the higher K_D and the enthalpic gain that appears to compensate for the loss in entropy, ($\Delta H < 0$ and $\Delta S < 0$), and that can be ascribed to: i) restriction of the conformational freedom of the functionalized HYLACH® ligand upon binding; ii) protein conformational rearrangements upon ligand binding; iii) reorganization of water molecules solvating the protein and /or the ligand. It is possible to speculate that in HYLACH® the pendant LAC-NH_2, although not changing the conformation of the HA-derived backbone, stiffens the overall structure which can, as a consequence, partially impair the wrapping around the Gal-3 molecule. It should also be considered that in HYLACH® fewer negative charges are available in comparison to HA. This is the consequence of the covalent binding of LAC-NH_2 to glucuronic acid units of the backbone, that can be confirm by the K_D of OHY2 similar to that of LAC-NH_2. As for many proteins at neutral pH, Gal-3 possesses a positive electrostatic potential with a pI of 8.58 (as estimated by ExPASy-ProtParam prediction server using the primary protein structure as a template). Structural analysis highlighted the presence of a positively charged "belt" spanning around the protein surface, compatible with the binding to a linear negatively charged polymer. The possible increase in rigidity combined with fewer available negative charges may

decrease the electrostatic interactions and increase the specificity of HYLACH® binding, this phenomenon could explain the higher K_D observed for OHY2. In addition, HYLACH® (OHY1 and OHY2), but not HA, have been reported to provide anti-inflammatory properties in an *in vitro* inflammation model of lung fibroblasts as showed by Donato et al.[108] This is likely to have the consequence that although possessing the same affinity as HA, the specific occupation of the CRD pocket by LAC-NH_2, triggers altered Gal-3 function in terms of reduction of both gene and protein expression of fundamental profibrotic molecules as reported by Donato et al. [109]

3.3.9. Circular dichroism

Circular dichroism measurements were performed to address conformational changes of Gal-3 upon ligand binding. Specifically, the CD signal in the far-UV (200–250 nm) provides information concerning possible changes in the protein secondary structure and conformation (α-helices, β-sheet and unstructured regions) that may be induced by interactions with other ligands. In the CD analysis, no significant variation of protein secondary structure content was observed, however, a decrease in the intrinsic CD signal was observed when titrating increasing concentrations of OHA and OHY ligands, reflecting the destabilizing and/or oligomerization of the protein (*Figure 3-15, Table 3-7*).

Table 3- 7: ***CD signals and standard deviation measured at 218 nm in the titration of Gal-3 with OHY1****, at different Ligand Protein molar ratio (L/P).*

L/P molar ratio	CD signal @ 218 nm
0.00	-7.12152 ± 0.080
0.012	-6.74927 ± 0.0795
0.025	-6.16536 ± 0.0787
0.05	-5.67469 ± 0.0781
0.10	-4.96339 ± 0.0767
0.20	-4.32979 ± 0.0758
0.33	-3.79987 ± 0.0754
0.50	-3.59526 ± 0.0738
1.00	-3.22123 ± 0.0739
2.00	-2.19865 ± 0.0728
4.00	-1.83421 ± 0.073
7.70	-2.60441± 0.074

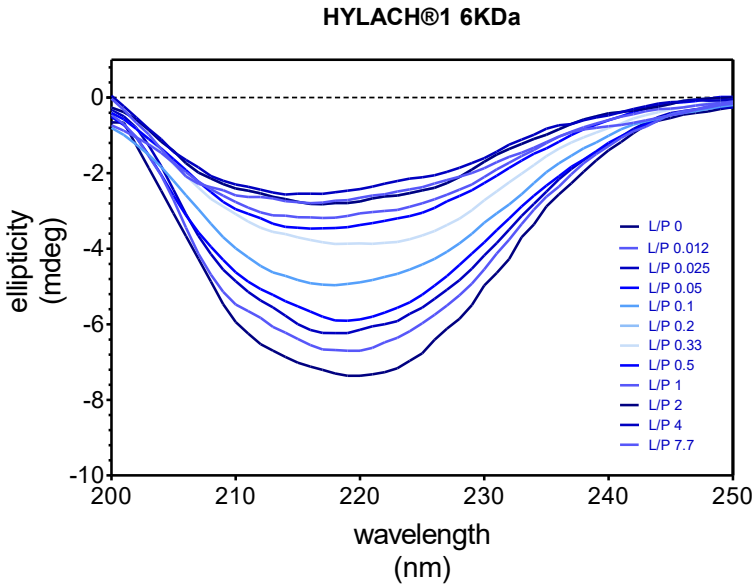

Figure 3- 15: ***Representative circular dichroism spectra titration of Gal-3 with increasing concentration of OHY1 sample****. To assess the protein changes upon ligand addition, we selected the intensity at 218 nm, where the CD spectral change was more significant.*

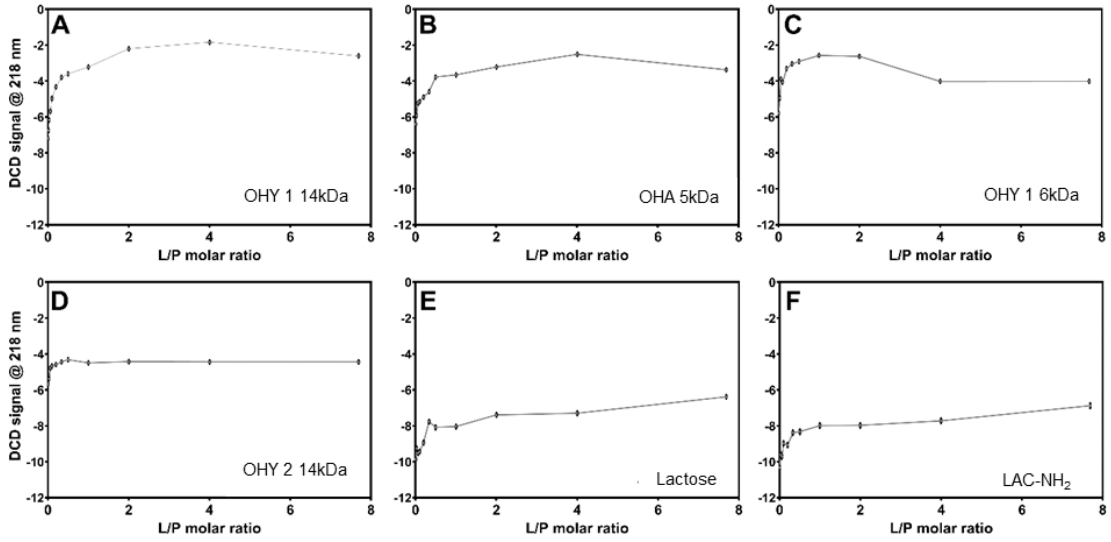

Figure 3- 16: ***Circular dichroism plots to evaluate protein conformation variation upon ligand binding****. CD signal variations at 218 nm, the maximum (negative) CD ellipticity for Gal-3 in the apo form, monitored in titration spectra of Gal-3 in the presence of increasing concentrations of HA and HYLACH® oligomers (OHA and OHY respectively) obtained after enzymatical hydrolysis compared to Lactose and LACNH₂. In details in figure are reported: A) OHY®1 (Molecular weight: 6 kDa, Degree of substitution: 14%), B) OHA (Molecular weight: 5 kDa), C) OHY1 oligomer (Molecular weight: 14 kDa, Degree of substitution: 14%) D) OHY2 oligomer (Molecular weight: 14 kDa, Degree of substitution: 37%), E) lactose and F) LACNH₂*

In more detail, the intensity at 218 nm, where the CD signal change was more significant, was plotted versus the Ligand/Protein molar ratio. Interestingly, in OHA and OHY, (*Figure 3-16, A-D*) the maximum in CD signal variation was reached at an L/P molar ratio of 0.5, and this is in line with ITC data, in which one molecule of ligand is bound to two molecules of Gal-3. Interestingly, the interaction of the protein with OHY2 at higher DS (37%) resulted in small CD signal variations comparable to the LAC-NH_2 and lactose (*Figure 3-16*) suggesting lower affinity and destabilization of the protein. The CD data on the reference small ligands, however, showed that the maximum variation of CD signal was reached in both cases at L/P molar ratio of 1, which is in good agreement with the stoichiometry measured by ITC data.

3.4. Conclusion

HA was successfully functionalised with an amino derivative of lactose to create a new biopolymer: HYLACH®. This new biopolymer was characterized, and the extent of substitution was confirmed by NMR spectroscopy. The molecular weight distribution of HYLACH®, determined by HP-SEC/TDA, was in the range of 85 kDa to 290 kDa depending on the starting HA. The biopolymer degree of substitution, determined by a validated bidimensional NMR method on the hydrolysed samples, was found between 14% to 44% depending on the synthetic condition used. A hydrolysis step was necessary in order to determine the degree of substitution using 2D-NMR, which cannot be measured directly on high-molecular-weight polysaccharides. ITC experiments provided that HYLACH® oligomers present strong affinities for Gal-3 in μM range, and this is consistent with literature of the enhancing of binding affinity for larger oligosaccharides, as well as complex-type N-glycans and poly-N-acetyllactosamine.[132], [133] CD experiments agreed with ITC data. Despite little variation of protein secondary structure being observed, a reduction in CD signals was seen with interaction studies of HYLACH® and HA oligomers. It was also observed that ligand binding significantly affected the stability of Gal-3, suggesting a further investigation of these functionalized HA as therapeutic inhibitors of Gal-3 associated human diseases such as the treatment of pulmonary disease and IPF.

The experiment with HYLACH® demonstrated how the combination of safety and biocompatibility of a functionalized sodium hyaluronate that is able to bind Gal-3 opens-up new perspectives in the therapy of IPF, and the results suggest that this biopolymer can be further investigated as a specific potential therapeutic drug.

Chapter 4

PENTOSAN POLYSULPHATE

Comparisons between the interactions of pentosan polysulphate and heparin with platelet factor 4.

4.1. Introduction:

As described in § 1.5, carbohydrates play a key role in several biological activities, thanks to their structural characteristics, which enable them to interact and form complexes with several proteins. One example is heparin, a sulphated GAG, which is well known for interacting with positively charged proteins such as platelet factor 4 (PF4). This interaction underlines both its therapeutic effects and its side effects.

Despite its clinical benefits, the use of heparin is limited by the risk of heparin-induced thrombocytopenia (HIT), an immune-mediated adverse reaction. HIT occurs when IgG antibodies recognise complexes formed between heparin and tetrameric PF4, particularly after conformational changes in PF4, such as an increase in antiparallel β-strand content compared to its monomeric counterparts. PF4, also known as CXCL4, is a member of the chemokines (CXC) protein family. PF4 consists of a small, heat-stable peptide molecules, with a size below 8KDa, which are insoluble in solution at low ionic strength. Monomeric PF4 consists of (from N to C termini) of three antiparallel beta-strands and one alpha-helix. [134][135][136]

In details, the interaction between PF4 and heparin stabilises the tetrameric form of the protein, exposing a variable immunogenic region, depending on the size of the bound heparin, or heparin-derived oligosaccharide. [136] The proportion of beta-strand increases upon complexation with heparin and, a variety of antibodies, which are polyclonal and polyspecific, have been identified. The incidence of this antibody-mediated response varies considerably depending on the clinical scenario and the type of heparin administered, with an higher prevalence observed in certain patient populations undergoing prolonged or intensive treatment. [137], [138], [139]

Furthermore, not all of the antibodies are associated with immunological problems, and the formation of antibodies does not directly correlate with the extent of immunogenicity in mice, [137] although there is evidence that complexes with positive Zp cause stronger immunological responses. [138]

HIT is routinely diagnosed using a screening assay to detect antibodies that bind to PF4/heparin complexes. Because antibodies binding is rather nonspecific, functional assays are required to demonstrate their potential of some of these antibodies to activate platelets *in vitro*, using heparin-induced platelet activation assay (HIPA) or serotonin release assays (SRAs); only these activating antibodies are clinically relevant. [140]

An interesting polysaccharide similar to heparin, due to its sulfation, is PPS. It is a semisynthetic, highly sulphated polysaccharide obtained by exhaustive O-sulfation of beechwood glucuronoxylan. [31] This chemical modification produces a heterogeneous mixture of polysaccharide chains, primarily composed of a backbone of repeating β(1→4)-linked D-xylose-2,3-di-*O*-sulphate units. A low degree of branching is present, involving α(1→2)-linked 2,3-di-*O*-sulphated 4-*O*-methyl-D-glucuronic acid residues. [33], [141] This active ingredient has been approved by both the US Food and Drug Administration (FDA) and the European Medicines Agency (EMA) for commercialisation under the name Elmiron for the treatment of interstitial cystitis and bladder pain syndrome. [142], [143]

Like heparin, PPS has been shown to possess anticoagulant activity [144] to demonstrate antiviral action against human immunodeficiency virus and influenza, [40] SARS-CoV-2, [41], [145] and influenza virus [146] and to possess anti-inflammatory activities [147]. It has also been shown to inhibit hepcidin expression [39], and its use has been evaluated for the treatment of mucopolysaccharidosis. [42], [148]

Clinical manifestations resembling HIT have been reported after the administration of PPS. [149] However, at the time most cases were described, antibody assays were not yet available, additionally some patients not only received PPS but also Heparin. Functional assays suggested an association of the clinical symptoms with PPS-induced thrombocytopenia. [150]–[155] The current state of knowledge regarding those structural features that underly the ability of PPS to induce HIT are not sufficiently well-understood to provide an explanation of the mechanism, nor reveal which structural or biochemical characteristics could serve as proxy measures, or predictors, of its extent. In this chapter is reported how closely PPS resembles heparin in its interaction with PF4. In the absence of any defined proxy measure for the likelihood of including HIT, employing a broad, multi-faceted and unbiased approach, encompassing several complementary physicochemical and biochemical properties, to compare the interactions between PPS and PF4 with those between unfractionated heparin and PF4.

This chapter reports several physicochemical and biological analyses, performed to establish and characterise the interaction between PF4 and PPS, and to compare the nature of these interactions with those observed for heparins (UFH and LMWH). [25]

The nature of the interactions between heparin and PF4 is known to differ for unfractionated and low molecular weight heparin and, in order to explore whether a similar relationship occurred in the case of PPS, it was fractionated with anionic exchange chromatography as reported by Bertini

et al. The interactions of its fractions, possessing varying molecular weights, and PF4 were also evaluated. [41]

Complex formation was assessed using a combination of orthogonal analytical techniques including dynamic light scattering (DLS), Zeta potential (Zp), atomic force microscopy (AFM) and isothermal titration calorimetry (ITC). The size of the resulting macromolecular complexes was strongly dependent on the molar ratio of PF4 to the ligand; the largest aggregates forming at ratios corresponding to net charge neutrality. Additionally, an enzyme immunoassay (EIA) was developed to evaluate the binding of monoclonal antibody (clone KKO), which functionally mimics pathogenic human antibodies implicated in immune responses associated with PF4/polyanion complexes. [156]

4.2. Materials and Methods

The pentosan polysulphate and the six fractions (named PPS Fractions 1.0, 1.1, 1.3, 1.4 and 2.0 at different Mw, [41] used in this study were supplied by bene pharmaChem GmbH & Co.KG (Geretsried, Germany). Enoxaparin (LMWH) was purchased by Sanofi Aventis (Bridgewater, USA), while for enzyme immunoassay LMWH Deltaparin, purchased by Pfizer Pharma (Berlin, Germany), was used, Fondaparinux was purchased by Mylan IRE Healthcare (Dublin, Ireland). Unfractionated porcine heparin (UFH) was purchased from Hepalink Pharmaceutical Co (Shenzhen, China), heparin used for EIA was purchased by Ratiopharm (Ulm, Germany). Hank's balanced salt solution (HBSS) was purchased from Sigma Aldrich (Milan, Italy), while phosphate-buffered saline was purchased from Biowest (France). 96 well Maxissorp F8 plates were purchased from Thermo Scientific (Dreieich, Germany). PBS-Tween was purchased from Jackson ImmunoResearch (Baltimore Pike, United States). PF4 freeze-dried in HBSS was purchased from ChromaTech (Greifswald, Germany). Lyophilized PF4 was dissolved in prefiltered water to achieve a concentration of 1 mg/mL (32 µM), while for enzyme immunoassay it was solubilized at a concentration of 3 µg/mL.

4.2.1. Photon Correlation Spectroscopy

Photo correlation spectroscopy (PCS) was used to determine the size of the particles in solution. PCS measurements were performed with a DLS Zetasizer Nano ZS (Malvern Instruments Ltd, UK) with a fixed angle at 173° and a 633 nm helium-neon laser, and the data were analysed with Zetasizer software version 7.12. To evaluate aggregate formation, the protein was titrated at different protein/ligand ratios (PLRs). For each sample, five different points were evaluated. Size solutions were measured after the transfer in a disposable size cell (ZEN0040, Malvern Panalytical, UK) of 80 µL of a solution, prepared as reported by Bertini et al. 2017, [25] obtained by the addition of a suitable volume of HBSS, ligand sample solution at different concentrations and 4 µL of PF4 32 µM. The analyses were recorded after 60 minutes at room temperature (RT).

4.2.2. Zeta potential

The Zp was measured with a Zetasizer Nano ZS (Malvern Instruments Ltd, UK), and the data were analysed with Zetasizer software version 7.12, Origin Software was used to fit the Zp data versus logPLR, allowing determination of the neutral state of the complex (Zp=0). As for PCS, for each sample, at least 5 different points were evaluated. In detail, to analyse the Zp, 40 µL of PF4 32 µM was added to the ligand sample solution and diluted with the correct amount of water.

Measurements were performed after 10 minutes of incubation at RT, in disposable folded capillary cell (DTS1070, Malvern Panalytical, UK). [25]

4.2.3. Isothermal titration microcalorimetry

Thermodynamic properties, such as variation of enthalpy, entropy, and Gibbs free energy (ΔH, ΔS and ΔG) and the binding affinities between samples and PF4, were obtained by ITC and were carried out using a MicroCal Peaq-ITC (Malvern Panalytical, UK). To perform ITC measurements 200 µL of 10 µM PF4 solution was loaded in the sample cell, and heparin or PPS solution was added into the injection syringe. Each ITC experiment consists of twenty injections of 2 µL each with a delay of 180 s between injections, the stirring rate was set to 500 rpm and the temperature was set to 25°C. To estimate the thermodynamic parameters (K_D, ΔH and ΔS), the data were fitted using the MicroCal analysis software.

4.2.4. Atomic force microscopy

Atomic force microscopy analyses were performed using an NX-12 microscope (Park Systems, Sud Korea) equipped with a Nikon IX optical microscope. Characterization was carried out in non-contact mode using qp-BioAC probes (Uniqprobe, CH) with a nominal elastic constant of 0.3 N/m and a resonance frequency of 90 kHz. The real elastic constant of the cantilever was regularly checked through the thermal noise method. For each sample, at least three different PLRs were evaluated. AFM samples were prepared on cleaved mica (1 cm^2) by depositing 80 µL of solution (distilled water and PPS solution), followed by 40 µL of PF4 (32 µM). After 10 minutes of incubation at 20°C, 3 mL of distilled water was used to remove unbound complexes, and the samples were analysed immediately. During acquisition, the driving frequency was set between 50–100 kHz and with cantilever oscillation amplitude kept below 20 nm. For each PLR, at least 10 images were collected from different random areas (including 5 µm-wide images collected collection with a 2–4 s/line scan speed). The data were collected using the using the SmartScan software (Park Systems, Sud Korea), while the analysis was conducted with the open software Gwyddion (v. 2.59), considering complexes larger than 20 nm. The observed nanostructures were divided in small, medium and large-size populations, and the equivalent sphere radius (Req.) was calculated from the measured average volume of each population.

4.2.5. Enzyme immunoassay

Platelet factor 4/ligand EIA was performed with monoclonal antibodies (mAb, a mouse IgG antibody) known to react specifically with PF4/heparin complexes and to induce HIT in platelet activation tests as described in the literature and called KKO.[157] PF4 (3 µg/mL) was preincubated (60 min at RT) with rising concentrations of ligand in PBS buffer to enable complex formation before coating wells of a microtiter plate with 100 µL at RT for 60 min. Then plates were washed three times with PBS-Tween (0.15 M NaCl, 0.1% Tween 20, pH 7.5) and incubated with 200 µL blocking solution for 60 min at RT (Roti-block, Roth, Karlsruhe, Germany). Then plates were washed three times with PBS-Tween and incubated with 100 µL diluted mAb for 60 min (KKO, diluted to 0.1 µg/mL in PBS-Tween). Plates were washed three times and incubated with 100 µL peroxidase-conjugated anti-mouse IgG diluted 1:20,000 in PBS-Tween. Afterward, plates were washed four times and incubated (10 min, RT) with 100 µL of TMB (tetramethylbenzidine). The reaction was stopped with 100 µL 1 M H_2SO_4 and absorbance was measured at 450 nm.

4.3. Results

4.3.1. Photo correlation spectroscopy

Literature reports [156] that certain polyanions can interact to the positively charged PF4, forming large and antigenic complexes. Photo correlation spectroscopy can be used to measure and monitor the average radius of these PF4/ligand complexes. Generally, titration of PF4 with a negatively charged ligand shows an increase in particle size after the formation of nonspecific electrostatic binding between the ligands and the protein. [25] After reaching a maximum point, however, the average size may decrease due to potential saturation or aggregation effects. This leads to a typical "bell curve" shape, in which the peak of the curve corresponds to maximum aggregation. Aggregation studies by PCS on PPS exhibit this typical behaviour, with a maximum aggregation achieved between PF4-ligand molar ratio (PLR) of 4 and 5, and with an average radius of about 540 nm (*Figure 4-1A*). PPS results were compared to UFH and LMWH data, which revealed that UFH/PF4 complexes reach peak aggregation at a higher PLR (between 12.8 and 16.0) and have an average radius exceeding 1000 nm, while LMWH/PF4 complexes display a maximum aggregation at PLR values between 3.2 and 2.0 and sizes consistently larger than PPS aggregates, but below 1000 nm.

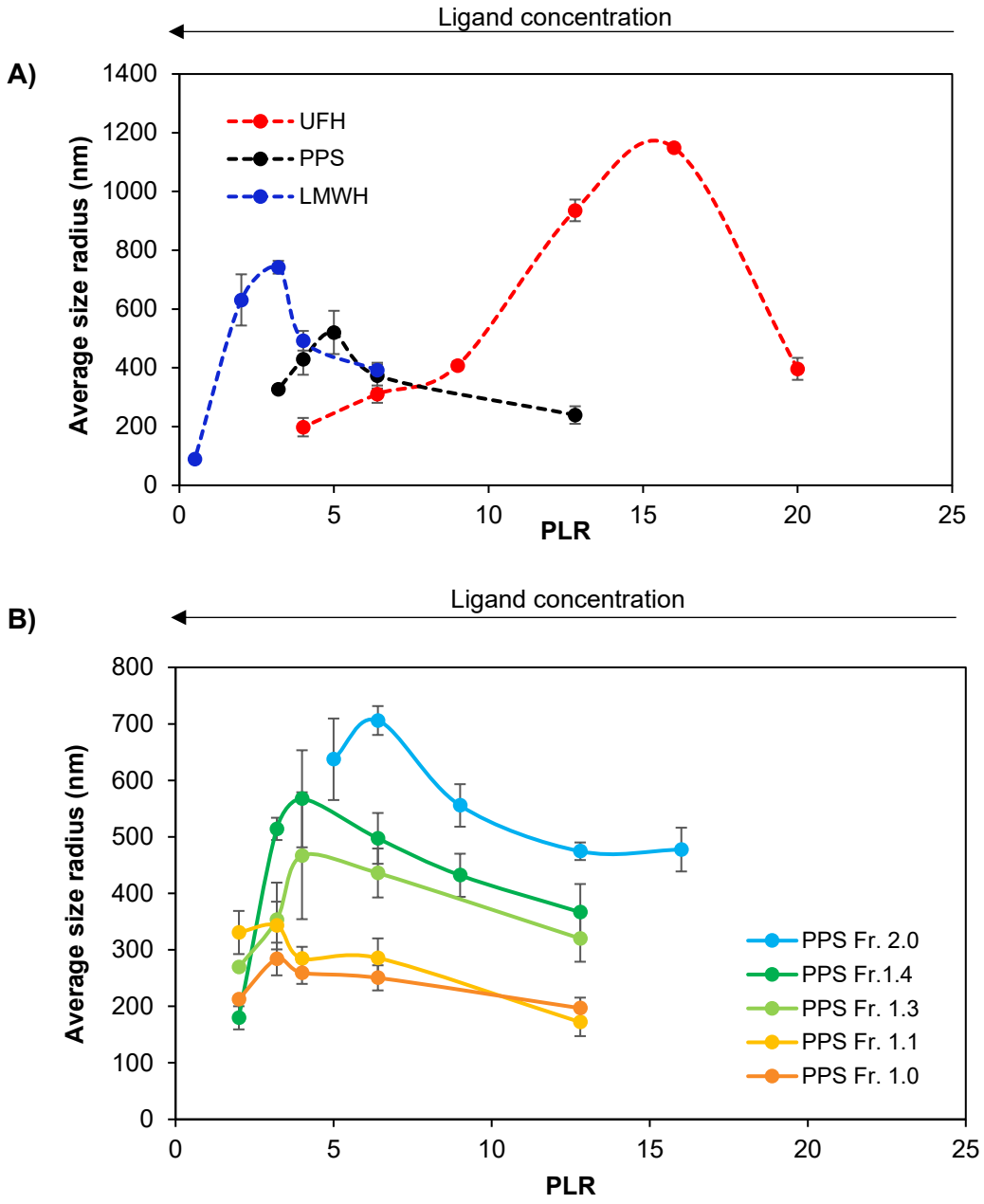

*Figure 4- 1:**PCS measurements of PF4/Heparin or PPS aggregates**. Average size over the PLR of (A) PPS (●), LMWH (●) and UFH (●). (B) PPS fractions: in detail are reported PPS Fr. 1.0 (●), PPS Fr. 1.1 (●), PPS Fr. 1.3 (●), PPS Fr. 1.4 (●), PPS Fr. 2.0 (●). The standard deviation is shown for each sample.*

The impact of PPS fractions with different Mw values on complex formation was evaluated (*Figure 4-1 B*). A decrease of fraction size corresponded to a reduction in the average size of the aggregates, as observed and reported in the literature for heparin fractions. [25] The behaviour of the aggregates of PPS fractions, especially for those at low Mw, however, was characterized by flatter curves, making the identification of the point of maximum aggregation more difficult. Unlike the other PPS fractions, PPS Fraction 2.0, which had the highest Mw (17 kDa), showed

maximum aggregation of a PLR between 4.0 and 6.4, with aggregates averaging 700 nm similar to PF4/LMWH complexes (*Table 4-1*). At low Mw, the PPS fractions exhibited a comparable PLR to PF4/LMWH, but with a smaller average radius (*Table 4-1*).

Table 4- 1: ***Summary of PCS and Zp results of LMWH, UFH, PPS and its fractions****, in terms of molecular weight, polydispersity index, protein-ligand complex average radius and PLR at the neutral zeta potential.*

Sample	***Mw [Da]***	***PDI***	***Z-average radius [nm]***	***Std Dev (nm)***	***Z-maximum PLR***	***PLR Zp=0***
UFH	18000	1.47	1110	28	12.8-16.0	11.2
LMWH	4300	1.37	707	39	2.0-3.2	3.2
PPS	5700	1.38	303	28	4.0-5.0	5.4
PPS Fr. 1.0	3700	1.04	284	20	3.2-5.0	3.2
PPS Fr. 1.1	5300	1.02	343	42	2.0-3.2	4.0
PPS Fr. 1.3	9100	1.01	466	38	3.2-4.0	8.7
PPS Fr. 1.4	11700	1.01	506	39	3.2-4.0	8.3
PPS Fr. 2.0	17000	1.02	706	26	5.0-6.4	11.2

Mw: molecular weight determined by HP-SEC;[41] *PDI*: polydispersity index determined by HP-SEC/TDA; [41] *Z-average radius*: radius value at the maximum of aggregation, *Std Dev*: Standard deviation of the Z-average radius, *Z-maximum PLR*: range of PLR, determined by PCS, where the size of the complex is higher, *PLR Zp=0*: PLR at which Zp reaches zero, as determined from the fit to the experimental data.

4.3.2. Zeta potential

The interaction between PF4 and ligands (PPS and heparins) is driven by electrostatic forces, and the complex formation follows a colloidal interaction model. Colloidal formulations remain stable at high positive or negative charges, which prevent flocculation, whereas a neutral charge is associated with particle instability and aggregation. A positive Zp has been linked to immunogenicity. [138] The surface charge of the complexes and the role of PPS and heparin ligands in the complex formation could be determined by a measurement of the Zp. The titration of PF4 with the ligands provides important information about the stoichiometry ratios and the charge. The typical titration curve is characterized by a sigmoidal curve (*Figure 4-2*). Initially, Zp of the protein assumes a positive value. Upon ligand addition, however, the Zp shifts to negative values. At the neutralization charge, where Zp is zero, all protein molecules are assumed to be bound to ligand molecules. Comparison of the Zp data of PPS demonstrated that it exhibits intermediate behaviour that of UFH and LMWH (*Figure 4-2A*), consistent with its intermediate Mw.

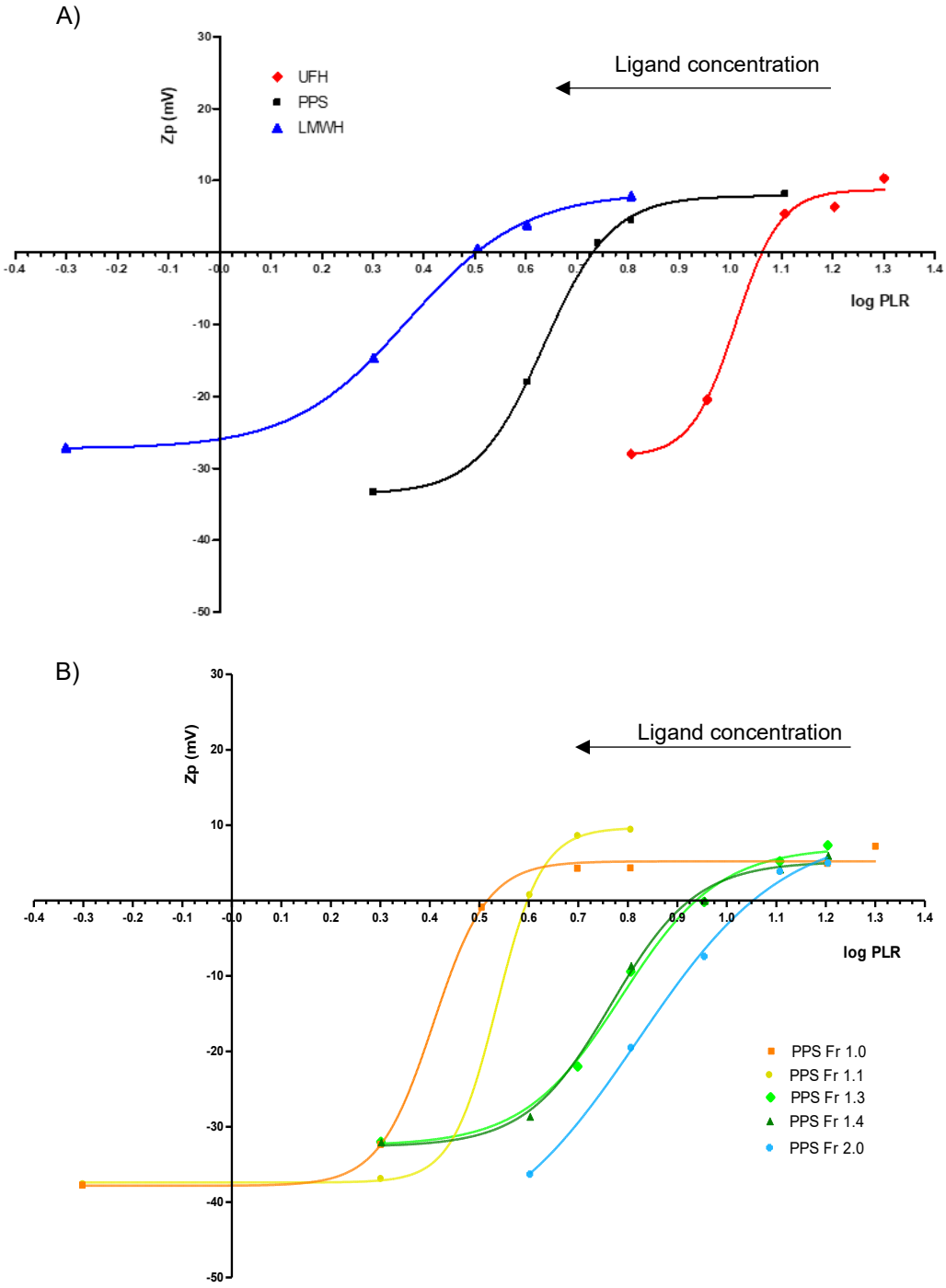

Figure 4- 2: ***Surface charge of PF4/ Heparins or PPS complexes****. Zp average [mV] vs log PLR (PLR: protein ligand ratio) of: (A) PPS (●), LMWH (●) and UFH (●). (B) PPS fractions: in detail are reported PPS Fr. 1.0 (●), PPS Fr. 1.1 (●), PPS Fr. 1.3 (●), PPS Fr. 1.4 (●), PPS Fr. 2.0 (●). Error bars, not reported on the graphs, of Zp measurements range between 0.07 and 2.5 mV for each point, based on three repetitions.*

As illustrated in *Figure 4-2*, PPS fractions demonstrated analogous behaviour to that of unfractionated PPS.

PPS fractions demonstrate a direct correlation between a decrease in Mw and a decrease in the Zp value at which charge neutralisation occurs, corresponding to the intersection of the fitting curve on the x-axis graph, log PLR, (*Figure 4-2B*). The same phenomenon is reported in literature in the case of heparin. [25]

PPS fractions 1.1 and 1.3 present similar values, hypothesized to be correlated with the slightly higher differences in the content of branched 4-O-methyl-D-glucuronic acid (MGA) residues in PPS fractions, [41] potentially reducing the number of available sites for interaction with the protein. Higher Mw fractions (such as Fraction 2.0, Mw: 17 kDa) reached a neutral Zp at higher log PLR than lower Mw fractions, indicating that lower molar ratio of the sample are required to reach protein neutralization (*Figure 4-2 B).* The PLR values at which the Zp is zero, determined from the sigmoidal fitting of Zp versus the logarithm of the PLR, as well as the average size and corresponding PLR ranges obtained from PCS measurements, are listed in *Table 4-1.* The maximum positive Zp values are similar between all of the PPS fractions and heparin samples (<= 10 mV) but, the concentrations at which these maximum values occur vary over half a log unit; PPS falling between those of LMWH and UFH (*Figure 4-2 A*). Similar variation was observed in the PPS fractions (*Figure 4-2 B*), indicating that, again, like heparin, PPS is a heterogeneous product comprising a variety of substituents. The overall similarities between these heparin and PPS samples, particularly their positive Zp characteristics, [137] [138] suggest likely similarities in immunogenicity.

4.3.3. Isothermal titration microcalorimetry

To further characterize the binding, ITC technique was applied to determine the binding constants and thermodynamic parameters of interactions between the PF4 and PPS and related oligosaccharides (***Table 4-2***). ITC results showed that the stoichiometry (N) of PF4 binding to each ligand was in the range 0.9 to 0.13, which correlated with the different Mw and chain lengths of the samples. Indeed, the interaction of PF4 with Fraction 1.0, which contains the smallest Mw fractionated PPS, resulted in a stoichiometry of about 1, suggesting that only 1 oligosaccharide chain was bound per protein. The binding stoichiometry, however, was found to change with increasing ligand Mw, with maximum binding of about 7-8 PF4 molecules per chain occurring with PPS Fraction 2.0 (N=0.13, Mw: 17 kDa). The same trend was observed for the equilibrium dissociation constant (K_D), with stronger binding for higher Mw fractions compared with the K_D of the complexes formed with short chain length. Additionally, both PPS and its fractions had favorable enthalpic (ΔH, -13.0 to -68.2 kcal/mol) and unfavorable entropic (ΔS, 3.2 to 56.9 kcal/mol) terms. The negative enthalpic contribution to binding was mainly attributed to the

formation of strong ionic interactions, hydrogen bonds and van der Waals interactions, all of which increase with the chain length, and consequently with the number of sulphate groups on the ligand. In contrast, the unfavorable entropic contribution was due to conformational changes restricting the conformational freedom of the complex. Similar to PPS Fraction 2.0 (Mw: 17 kDa) with comparable Mw, thermodynamic parameters were estimated for PF4/UFH binding, showing that 4 protein molecules bind per heparin chain, whereas LMWH (Mw: 4.3 kDa) showed the same stoichiometry, but weaker binding compared to the complexes formed with PPS fractions 1.0 and 1.1 which contain PPS chains with similar Mw, respectively of 3.7 kDa and 5.3 kDa.

Table 4- 2: ***Binding constants and thermodynamic parameters of PF4 interactions with PPS and its fractions determined by Isothermal Titration Calorimetry (ITC).*** *Results were compared to the interactions between PF4 and UFH or LMWH.*

Sample	***N (Sites)***	***PLR (1/N)***	***K_D (M)***	***ΔH (kcal/mol)***	***ΔG (kcal/mol)***	***-TΔS (kcal/mol)***
PPS	0.369± 0.003	3	$27.8 \times 10^{-9} \pm 4.86 \times 10^{-9}$	-22.9±0.35	-10.3	12.6
PPS Fr. 1.0	0.899±0.01	1	$74.1 \times 10^{-9} \pm 11.2 \times 10^{-9}$	-13.0±0.20	-9.7	3.2
PPS Fr. 1.1	0.504±0.03	2	$23.2 \times 10^{-9} \pm 3.40 \times 10^{-9}$	-20.3±0.21	-10.4	9.8
PPS Fr. 1.3	0.265±0.002	4	$20.2 \times 10^{-9} \pm 3.84 \times 10^{-9}$	-37.3±056	-10.5	26.8
PPS Fr. 1.4	0.146±0.001	7	$10.1 \times 10^{-9} \pm 1.77 \times 10^{-9}$	-61.3±0.83	-10.9	50.4
PPS Fr. 2.0	0.132±0.001	8	$5.39 \times 10^{-9} \pm 0.78 \times 10^{-9}$	-68.2±0.63	-11.3	56.9
UFH	0.254±0.016	4	$6.17 \times 10^{-9} \pm 0.78 \times 10^{-9}$	-47.0±3.68	-11.3	35.8
LMWH	1.170±0.11	1	$340 \times 10^{-9} \pm 17.7 \times 10^{-9}$	-9.20±0.04	-8.83	0.37

N: stoichiometry of the interaction; K_D: dissociation constant; ΔH: variation of enthalpy; ΔS: variation of entropy; ΔG: variation of Gibbs free energy;

4.3.4. Atomic force microscopy

Atomic force microscopy (AFM) in solution was used to characterize the PF4/PPS complexes at the nanoscale level, providing information about the shape, size and abundance of the aggregates. The analyses were performed in tapping mode in solution to prevent disruption of the complexes and to reproduce a system close to the native physiological environment. The mica surface was not functionalized, as surface derivatization may induce non-native interactions, conformational changes, or unfavorable molecular orientations that could compromise accessibility of the physiological binding sites.

Blank analysis, performed on PF4 protein deposits on mica surfaces, without the addition of the ligand, revealed an absence of aggregate formation, *Figure 4-3*.

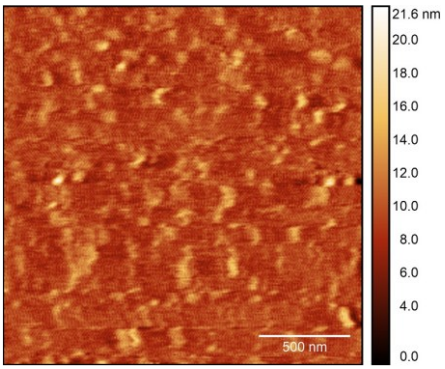

Figure 4- 3: ***AFM analysis of PF4, without the addition of ligand****. The mean roughness is 0.67 nm.*

The concentration of the reagent deposited on the mica and the deposition time, were both chosen in order to ensure an electrostatic interaction between the mica and the complexes. All the samples were analysed under conditions close to, below and above the Zp zero point, confirming the trend obtaining at the DLS. *Table 4-3* shows the characteristic values measured for the PPS sample, reporting the mean aggregates volume, the percentage of aggregated materials and the average aggregate size (expressed by the equivalent sphere radius, REq), measured at three different PLR values. Similar results were observed for all of the investigated samples. Specifically, no or few aggregates were detected at lower PLR values; the aggregate size reached a maximum at intermediate PLR values and the degree of aggregation dropped significantly at higher PLR values.

*Table 4- 3****: AFM subpopulation of PPS/PF4 complexes observed at different PLR.*** *The table reports the measured mean volume value, % of volume*

PLR	Ligand concentration (µM)	Mean volume (nm^3)	% in volume	REq. (nm)
0.5	3.20	0	-	0
5.4	0.23	$4.21x10^{10}$	87%	2158
12.0	0.13	$2.31x10^{8}$	83%	380

Figure 4-4 show a comparison of the AFM results for PPS, PPS fraction 1.0, and PPS fraction 1.4, obtained at PLR values close to zero Zp, a condition previously demonstrated to represent the higher number of population aggregates. All aggregates showed approximately round structures of different sizes and abundance. The features observed in the PPS fraction 1.0 are, on average, slightly larger than those in the PPS sample. In addition, PPS fraction 1.0 (Mw: 3.7 kDa) (*Figure 4-4 B*), was characterized by higher aggregation compared to PPS fraction 1.4 (Mw: 11.7 kDa) (*Figure 4-4 C*).

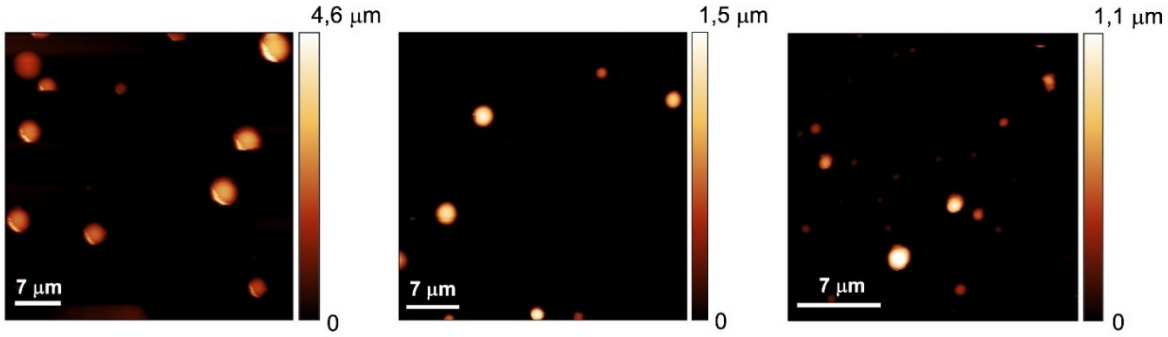

Figure 4- 4: ***AFM images of the PF4/PPS aggregates****, achieved at PLR close to the zero Zp of A) PPS sample at PLR 5.4, B) PPS fr. 1.0 at PLR of 3.2, and C) PPS fr. 1.4 at PLR of 9.*

4.3.5. Enzyme immunoassay

Enzyme immunoassay (EIA) was used to quantify the formation of PF4/heparin complexes and their recognition by the monoclonal antibody KKO. The antigenicity obtained with the PF4/ligand EIA is highly concentration dependent on the PF4/Ligand ratios. For UFH, PPS and PPS fractions, the antigenicity rose with increasing ligand; reaching a maximum at an optimal value and a further increase in ligand concentration decreases the binding of the specific antibody to the PF4/ligand complexes. UFH, LMWH, fondaparinux (the anticoagulant pentasaccharide, which is known not to cause HIT) and PPS comparison are reported in *Figure 4-5 A*. Fondaparinux as expected does not show the formation of PF4/ligand antigenic complexes, while LMWH showed strongly reduced binding in comparison to UFH and PPS samples. PF4/UFH and PF4/PPS aggregates were similar in intensity and maximum point values. Immunoassay analysis on the PPS fractions (*Figure 4-5 B*), showed that PPS Fr. 2.0, the higher Mw (17 kDa), i.e. longer xylose-chains, presents a high peak at the highest molar concentrations. Otherwise, PPS fraction with the lowest Mw (PPS Fr. 0.8, Mw: 2900 Da, PDI: 1.10) showed the lowest peak of antibody-binding at the lowest molar concentration (*Figure 4-5*). This fraction shows an atypical reactivity with two peaks. It also exhibits atypical behaviour in physicochemical characterization and significant differences in its composition (data not shown).

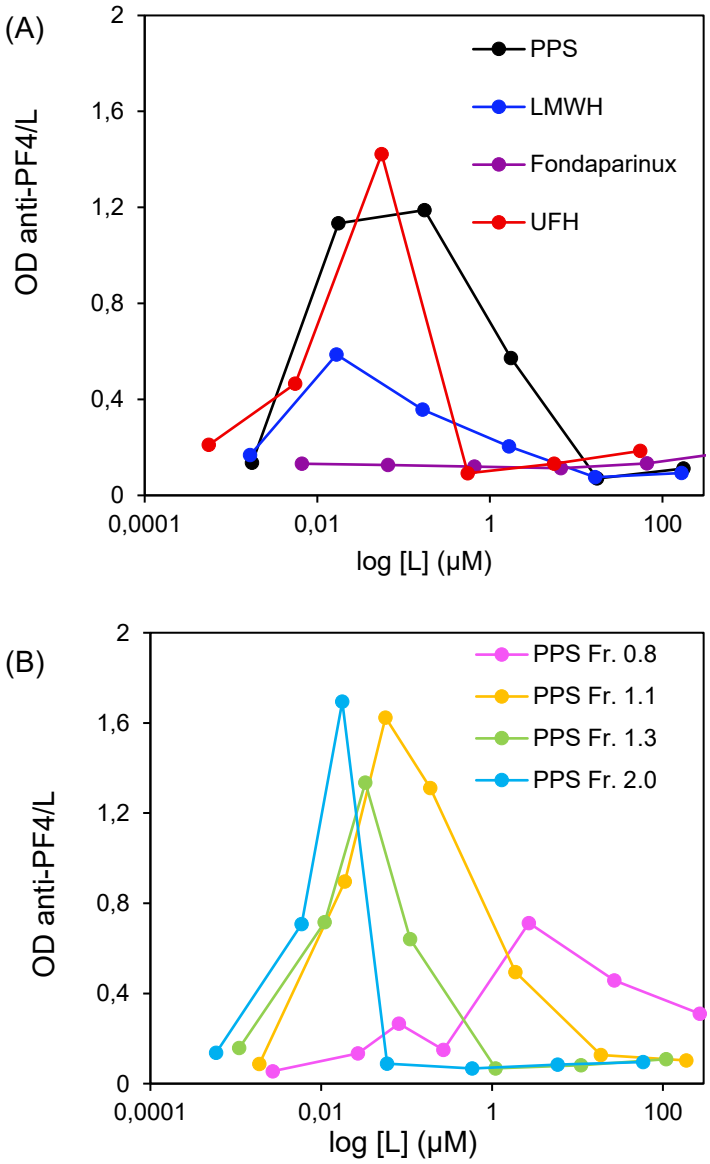

Figure 4- 5: ***Reactivity of anti-PF4/ligands (L) antibody KKO****. The optical density (OD) of anti PF4/L versus the logarithm of the concentration of ligands (log[L]) of (A) PPS (●), UFH (●), LMWH (●) and Fondaparinux (Mw ~1.7, ●); (B) PPS fractions; PPS Fr. 0.8 (●), PPS Fr. 1.1 (●), PPS Fr. 1.3 (●), PPS Fr. 2.0 (●).*

4.4. Conclusion

Currently, pentosan polysulphate is used widely to treat bladder pain syndrome and interstitial cystitis in humans with an oral formulation. As PPS shares some structural similarities with heparin, it has also been investigated as an anticoagulant. PPS exhibits only around one tenth the activity of heparin, however, and furthermore it inhibits heparin action. [158] More recently, the potential of PPS to bind viruses, similar to the action of heparin and other GAGs, has also been explored. [41] Several other potential applications have also been investigated, such as cancer [159] and prion diseases, [160] and comparative studies revealing that protamine sulphate neutralises PPS more weakly than it does heparin.[161] With the interest of using PPS in a variety of new applications, some of which could include its parental administration as well as the manufacture of materials incorporating PPS, it is also important to understand any potential risks that it may pose and it was useful to compare these with UFH and LMWH, particularly regarding the response in relation to concentration. The major risk upon extended heparin administration is posed by the immunogenic response to complexes formed from PF4 and heparin. A fully heparinised patient may have serum concentrations of about 1.5 – 3.5 μg/mL (considering a level on the serum of 0.3 – 0.7 IU/mL for a dose of 196 IU/mg) [162] and the half-life of heparin varies between 1.5 hours (for UFH) to 2-5 hours (for various LMWH preparations), driven in part by its enzymatic degradation by endogenous heparinase, and up to 21 hours for Fondaparinux, the synthetic pentasaccharide heparin analogue. If administered intravenously, PPS would not be subject to heparinase degradation but, is known to bind to a number of growth factors and receptors; [163] a half-life of 4.8 hours has been reported. [164]

The *in vivo* risk of HIT is related subtly to several structural properties that include the size of the aggregates formed, their overall charge, as well as their ability to provoke an antibody response; this latter property being further complicated as a means of predicting in vivo side-effects by the polyclonal and polyspecific nature of the antibody response. [138] The size of PPS/PF4 complexes was found to depend on their molar ratios and was intermediate between those formed by PF4 with UFH and LMWH but, its maximum size was smaller than that formed with heparin. More complex behaviour was observed with the PPS fractions, although the complexes were smaller with lower molecular weight PPS fractions. Zeta potential analysis provided deeper insights into the behaviour of PF4/PPS aggregates by enabling the determination of the zero point, which corresponds to maximum complex formation. [25] PPS exhibited a comparable profile and, as for PCS measurements, its extrapolated Zp zero value lay between those of LMWH and UFH (*Table 4-1*), consistent with the Mw of the PPS samples. This trend was also observed in the PPS fractions, where the lowest zero Zp value was found in the fractions with the lowest Mw (PPS Fr. 1.0, Mw 3.7 kDa). This indicates that more ligand is required to reach the neutralisation point.

Studies using ITC also showed that PPS exhibits PF4 affinity values between those of UFH and LMWH. Its stoichiometry (0.369) indicating that two to three PF4 proteins are bound to each PPS chain. Binding interactions were exothermically and enthalpically driven in all samples, suggesting the formation of strong ionic interactions, coupled with hydrogen bonds and van der Waals interactions between the sulphate groups of the ligands and PF4. For both PPS and UFH, complex formation was accompanied by negative entropy, indicating restriction of the conformational freedom of the ligands and conformational rearrangements of the protein. ITC studies of PPS fractions showed that the binding affinity increases with the molecular weight of PPS fractions.

The relatively low K_D values achieved for PF4 with PPS and its fractions were indicative of high affinity. The higher negative enthalpy seen in PF4/PPS interactions, can be attributed mainly to the formation of strong ionic, hydrogen bond and van der Waals interactions with the positively charged PF4 protein.

Atomic force microscopy confirmed that aggregation depends on ligand concentration. Smaller particles adhered more easily to the mica surface, and the limited scanning range favoured the detection of smaller and medium-sized sub-populations while excluding the larger components (size greater than, approximately 5-6 μm) which were observed by an optical microscope (data not shown). These limitations of the AFM technique explain why PPS Fraction 1.0 aggregates were larger than those of PPS Fraction 1.4 (Mw 11.7 kDa). PPS samples exhibit different size populations, confirming these observations.

Finally, immunoassay analysis of KKO antibody binding to both PF4–heparin and PF4/PPS complexes was consistent with other analytical data and binding was strongly dependent on PLR.[156] The size, approximately 12 sugars units, was identified as key parameters of interaction in this study. While PPS showed antigenicity closer to UFH than to LMWH, despite its Mw resembling that of LMWH, the antigenicity of the PPS fractions was dependent on the chain length of the sugar backbone. The in vitro detection of HIT-antibody binding does not, however, strictly correlate with in vivo immunogenicity or clinical outcome, as antibodies against PF4-ligand complexes, especially with UFH, are more common than active antibodies in functional assays and, these are not always associated with clinical signs of HIT-2. Furthermore, Fondaparinux, based on a single pentasaccharide from heparin, cannot induce the neoantigen on PF4 and therefore exhibits no in vitro binding of HIT-2 antibodies in diverse assays but, has been shown to induce anti-PF4/ligand antibodies in patients treated solely with fondaparinux.[165] The findings suggest that, regarding the possible induction of HIT though interactions with PF4, PPS exhibits properties comparable to those of heparin (UFH) and its derivatives (LMWH). To ensure that any future applications of PPS, especially involving intravenous application, are safe, further studies, particularly in vivo are warranted.

Interestingly, despite PF4 complexes with PPS, and PF4 complexes with its fractions, being smaller than those formed between PF4 with UFH or LMWH, EIA studies demonstrated the formation of antigenic (KKO antibody) complexes. It is recognised that the KKO antibody mimics the behaviour of some HIT antibodies, however not all antibodies, so further investigation of the immunogenicity of PPS and its fractions will be necessary. Since PPS appears to provoke comparable interactions with PF4 and has a plasma half live longer than heparin - but much shorter than Fondaparinux, the results suggest monitoring of potential thrombocytopenia effects will be necessary (as for treatment with heparin) when considering PPS dosing, especially for intravenous applications.

The current state of knowledge concerning the structural causes underlying the propensity of PPS, as well as heparin, to induce HIT does not provide an explanation of the precise mechanism, nor suggest particular structural or biochemical characteristics that can provide proxy measures, or serve as predictors, of its extent. With this limitation in mind, but wary of the fact that PPS is employed as an anticoagulant, the similar structural and immunological consequences arise through PPS interactions with PF4 as with heparin, whose tendency to induce HIT in patients is well-known, were emphasis. The use, or any future development of PPS for indications in which its parental administration is proposed must, therefore, be tempered by an appreciation of the possibility of a comparable risk of inducing HIT.

Chapter 5

LIPID NANOPARTICLES

Lipid nanoparticles as a strategy for the encapsulation of polysaccharides

5.1. Introduction

In recent years, there has been a growing interest in drug delivery and targeting systems, particularly lipid nanocarriers (LNCs), to the extent that they have become the most widely used drug delivery system for molecular transport. LNCs, and especially liposomes, were also the first nanoparticles approved for drug by regulatory bodies such as the FDA and EMA. [166]

The success of these system arise from the numerous advantages that they offer, including their low toxicity, their high biocompatibility, their ability to protect the active content from moisture, pH, and enzyme activity, and the ability to encapsulate both hydrophobic and hydrophilic molecules. [167]

Additionally, LNCs can be easily targeted to release their active content at specific sites.[166] In particular, they allow two targeting mechanisms: passive, which is related to the enhance permeability and retention of tissue in diseases such as cancer; and active, which involves surface modification of the carrier through chemical reactions. [168][169]

Lipid nanocarriers have also been identified as a promising approach for the encapsulation of polysaccharides. Several lipid-based systems designed to encapsulate polysaccharides have been reported in literature. [170][171]

Most polysaccharides, including HA and heparin, are susceptible to enzymatic degradation. Furthermore, their high Mw and charged nature may compromise their ability to efficiently reach target sites. For these reasons, many polysaccharides can only be administered through invasive routes, while others, such as heparin and PPS, exhibit poor oral bioavailability,[27] and are rapidly cleared in the body. [162] [164]

Encapsulation within LNCs overcome these limitations by protecting polysaccharides from enzymatic degradation and improving their biodistribution.

Several LBDDS formulations encapsulating heparin have been documented in the literature. Most of these studies have focused on developing formulations that can offer less invasive methods of

heparin administration, such as oral, inhaled, topical, and spray administration. Liposomal heparin has proven suitable for clinical applications, with prolonged anticoagulant activity observed. [28] Additionally, a liposomal heparin spray gel formulation developed for topical delivery demonstrated both safety and efficacy.[172]

Cationic PEGylated liposome formulations, characterized by small particle size (approximately 100 nm) and high encapsulation efficiency, have been shown to extend the half-life of heparin and to be effective in the treatment of venous thromboembolism. [173] [174]

In the field of LNCs, HA is often used as an external nanoparticle coating, primarily for targeting purposes. [175] However, several studies have demonstrated that the encapsulation of HA increases its permeation and retention through the skin.[176][177][178]

5.1.1. Formulation components

Lipid nanocarriers are defined as submicron-sized lipid vesicles that encapsulate a therapeutic cargo. [179]

The most recent nanocarriers to be authorised are lipid nanoparticles (LNPs), which have been approved for the delivery of Patisiran and the SARS-CoV-2 vaccines.

All the approved LNPs formulations contains four key components:

- Ionizable lipid
- Helper lipid
- Cholesterol
- PEGylated lipid

These components are typically present in a molar ratio of about 50:10:38.5:1.5 mol%, with each playing a distinct and essential role. [180]

Ionizable lipids (ILs) are a class of lipids, composed of an ionizable polar head group (most commonly a tertiary amine) and two or more hydrophobic hydrocarbon chains. ILs typically exhibit a pKa value of aroung 6.2–6.5, allowing them to become protonated and positively charged under acidic conditions, enabling the interaction with negatively charged cargo, while they remain neutral at physiological pH, to minimise toxicity. [180] ILs not only promote efficient encapsulation of negatively charged drugs, but also enhance endosomal escape, as their electrostatic interactions with endosomal membranes destabilise the bilayer and trigger a release of the cargo. [61], [181], [182]

Several ILs have been approved from EMA and FDA, including DLin-MC3-DMA, used for Patisiran, and SM-102, employed in a mRNA vaccine against SARS-CoV-2.

Cholesterol typically constitutes around 40% of the total lipid composition of an LNP formulation. It performs several structural functions, including improving particle stability, modulating membrane rigidity, maintaining the bilayer and enhancing delivery efficiency. It has

also been shown to reduce surface protein adsorption, thereby prolonging the circulation half-life. Moreover, the presence of a hydroxyl functional group allows cholesterol to be easily functionalised for targeting purposes. [180], [181], [182]

Phospholipids are a class of helper lipids, usually present at around 10% of the total lipid composition. They provide structural integrity, modulate the fluidity of the lipid bilayer and influence the *in vivo* biodistribution of nanoparticles. A common example is 1,2-distearoyl-sn-glycero-3-phosphocholine (DSPC). [180]

PEGylated-lipids (PEG-lipids) represent the minor component of the lipid formulations, generally not more than the 3%. This class of molecules consists of lipids conjugated to hydrophilic polyethylene glycol (PEG) polymers.

These lipids regulate particle size and polydispersity, thereby influencing the encapsulation efficiency of the therapeutic cargo. The absence of PEG-lipids in a formulation has been shown to increase the nanoparticle diameter. They prevent aggregation and improve stability, and prolong the circulation time *in vivo*, thereby avoiding clearance of the nanoparticles. PEG-lipids have, however, influence on the immune response, and a notable drawback associated with their use is their immunogenicity.

Repeated dose can stimulate the production of anti-PEG antibodies, which, not only enhance clearance and reduce therapeutic efficiency, but also lead to allergic reactions and other adverse effects. [183]

The structure of the four examples of lipids, one for each class, are reported in *Figure 5-1*.

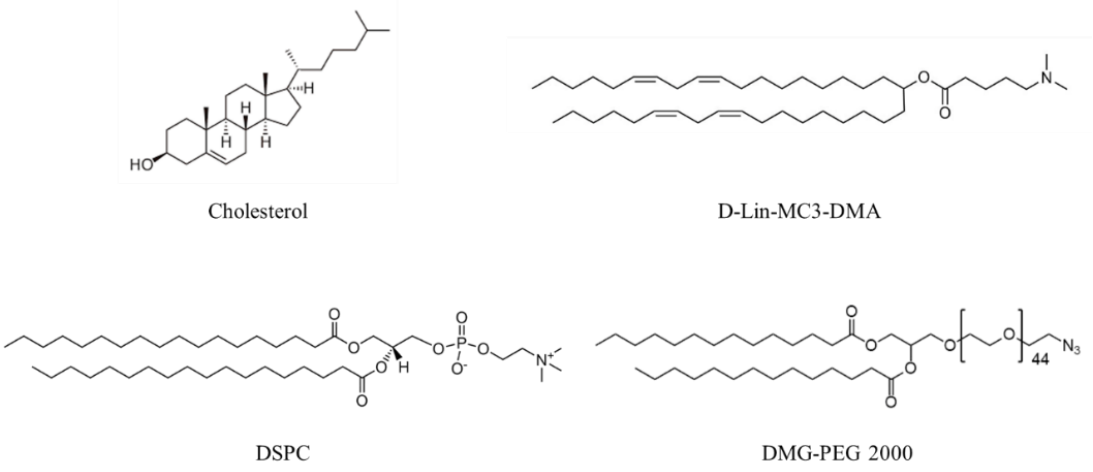

Figure 5- 1: ***Chemical structure of four components of the LNPs formulations.***

5.1.2. Characterization of the LNPs

The structural organisation of LNPs has not yet fully elucidated, primarily due to the complexity of their composition and the variability introduced by the different types and ratios of lipids used in the formulations. Additionally, factor such as size of the cargo molecules and the production methods employed can further influence their structure arrangement.
However, the most widely accepted structural model for LNPs encapsulating RNA is illustrated in *Figure 5-2*. [59]

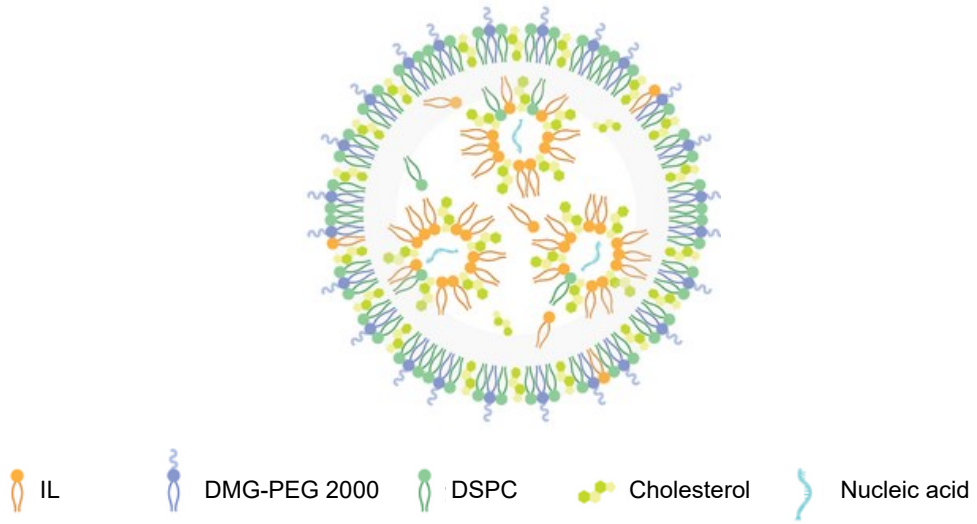

Figure 5- 2: ***Hypostatised RNA-LNPs structure,*** *imagine preprint from Cayman.*

Given their complexity, the characterisation of the LNPs is essential, as each parameter can influence their therapeutic performance. For instance, the size and PDI influence the half-life time of drugs *in vivo* and the intracellular delivery. Small NPs, with a size below 10 nm, can be easily removed by the lymphatic system, whereas LNCs with a size greater than 100 nm are easily excreted by the spleen. The optimal particle size for pharmaceutical LNPs is therefore considered to be below 100 nm. [184], [185]
For this reason, in 2018 and subsequently in 2022, the FDA issued the first guidelines defining the critical quality attributes (CQAs) for the production and characterisation of LNCs.
As outlined in § 1.6.1, these CQAs encompass not only the characterisation of the API and lipid content, but also the nanocarrier properties, including size distribution, PDI, and Zp.

5.2. Materials and methods

LNPs were produced using the same lipidic formulation employed in the first approved lipid nanoparticles, ONPATTRO.[186] The LNPs were composed of Dlin-MC3-DMA: Chol:1,2DSPC:DMG-PEG2000 in a molar ratio of 50:38.5:10:1.5. Individual lipid stock solutions were prepared in ethanol and different lipid mixture concentrations. Heparin, HA and PPS were dissolved at different concentration ranging from 0.5 mg/mL to 30 mg/mL in 0.14 M sodium chloride (NaCl) solution pH 6. UFH was purchased from Hepalink Pharmaceutical Co (Shenzhen, China), LMWH was purchased from Sanofi Aventis (Italy), Arixtra (Fondaparinox) was purchased from Aspen, PPS was purchased by Benepharma and HA was purchased from HTL.
Filtered and distilled water (conductivity: 0.055 µS) was achieved with Elga Veolia system.
96 well Maxissorp F8 plates, Alexafluor 405 and Alexa fluor 488 were purchased from Thermo Scientific. NaCl, absolute ethanol (EtOH), sodium phosphate dibasic dihydrate (NaH_2PO_4), sodium phosphate monobasic monohydrate (Na_2HPO_4), cholesterol assay, fluorescein isothiocyanate (FITC), sodium acetate trihydrate, acetic acid, sodium citrate dihydrate, citric acid, pyridine, cholesterol, 1,2-Distearoyl-sn-glycero-3-phosphocholine (DSPC), 1,2-Dimyristoyl-sn-glycero-3-methoxypolyethylene glycol (DMG-PEG2000) were purchased from Sigma Aldrich (Italy). 4-(dimethylamino)-butanoic acid, (10Z,13Z)-1-(9Z,12Z)-9,12-octadecadien-1-yl-10,13-nonadecadien-1-yl ester (DLin-MC3-DMA) was purchased from Cayman chemicals (United states).

5.2.1. LNPs formulation IJM Nanoscaler

LNPs formulations were produced using the mixing chamber 2 (IJM2) of IJM Nanoscaler from Knauer (Germany). The instrument set up is shown in *Figure 5-3*. The lipid mixture was directly injected in the instruments via a syringe (Pump 1), while the polysaccharide solutions were maintained in continuous flow (Pump 2). Following production, the LNPs were diluted with quenching buffer (Pump 3), 2:1 dilution ratio. The total flow rate (TFR) was set between 2 mL/min and 12 mL/min. Lipids were injected at concentration of 3, 6 and 9 mg/mL. The aqueous-to-organic ratio (FFR) was set at 3:1. The buffers evaluated included sodium acetate (pH 4.5), citrate buffer (pH 5.5), and phosphate-buffered saline (PBS, pH 7.3).

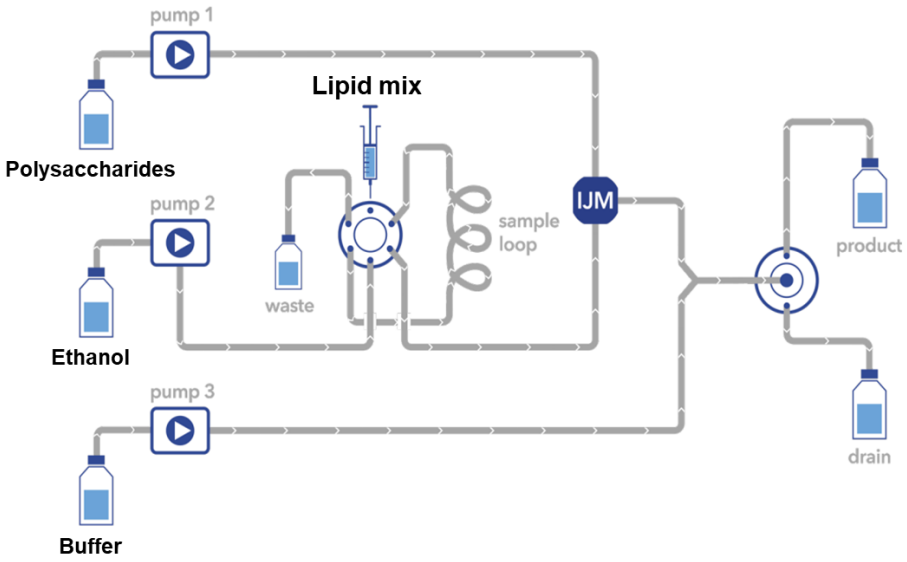

Figure 5- 3: ***IJM Nanoscaler set up.*** *Imagine preprint from Knauer.*

The formulation of fluorescent heparin was performed using the IJM Nanoscaler, incorporating an additional 2.5 mL loop on pump 1, in order to reduce the consume of reagent.

5.2.2. Purification with Gel Permeation Chromatography

For the purification of Hep-LNPs, a Sepharose CL-4B column (1.6 cm diameter × 10 cm height) was used, with 0.1 M phosphate-buffered saline (PBS, pH 7.3) as the elution buffer. Sample volumes of 1 -2 mL were loaded onto the column. Fractions were collected every 0.5 mL and analysed using a Cary 3500 Compact UV-Vis Spectrophotometer (Agilent Technologies, Italy), equipped with a Cary UV workstation. Absorbance was measured at 210 nm, and 488 in presence of fluorescent heparin.

5.2.3. Synthesis of fluorescent heparin

Various fluorescently labelled heparins were synthesized using different dyes, including Alexa Fluor 488, Alexa Fluor 405, and fluorescein isothiocyanate (FITC).

5.2.3.1. Alexa Fluor 405-Heparin

UFH (1 eq) and Alexa Fluor 405 cadaverine (0.1 eq) were dissolved in PBS at a concentration of 20 mg/mL, with the pH adjusted between 6.5 and 8.5. N-hydroxysuccinimide (NHS, 0.1–4 eq) and 1-ethyl-3-(3-dimethylaminopropyl) carbodiimide (EDC, 0.1–4 eq) were then added subsequently, with EDC introduced gradually over 24 to 48 hours at temperatures ranging from 0 °C to 25 °C. The crude product was purified using a PD10 column.

5.2.3.2. Alexa Fluor 488-Heparin

UFH, 1 eq and Alexa Fluor 488 hydrazide (0.1 eq) were dissolved in PBS (pH 7.3) at a concentration of 20 mg/mL. To this solution, NHS (4 eq) and EDC (4 eq) were added, with EDC introduced gradually over a period of 24 hours at room temperature. The crude product was purified using a PD10 column.

5.2.3.3. Fluorescein isothiocyanate-Heparin

UFH (1 eq), solubilized in water at a concentration of 100 mg/mL, was passed through IR-120^{+} ion-exchange resin. The resulting solution was quenched with pyridine, concentrated, and then solubilised in DMSO. FITC, 0.1 eq was added, and the mixture was heated at 90 °C for 2.5 hours. The crude product was purified by precipitation in ethanol and washed several times.

5.2.4. Photo correlation spectroscopy

The size distribution and PDI of the LNPs were measured using a Zetasizer Nano ZS (Malvern Panalytical Ltd., UK), equipped with a 633 nm laser and a backscatter detection angle of 173°. A 100 µL aliquot of each sample was loaded into disposable cuvettes (ZEN0040, Malvern Panalytical Ltd., UK) and analysed at 20 °C. All measurements were performed in triplicate, and results were reported as average values. Data analysis was conducted using Zetasizer software version 7.12.

5.2.5. Electrophoretic light scattering

The Zp, used to assess the stability of the formulations, was measured using a Zetasizer Nano ZS (Malvern Panalytical Ltd., UK). Data analysis was performed with Zetasizer software version 7.12. Formulations were diluted 1:2 with filtered and distilled water, and 800 µL of each sample was loaded into disposable folded capillary cells (DTS1070, Malvern Panalytical Ltd., UK) for analysis.

5.2.6. Nuclear magnetic resonance spectroscopy

Proton NMR spectra were recorded at 298 K on a Bruker AVANCE NEO spectrometer operating at a proton frequency of 500MHz (Bruker, Karlsruhe, Germany), equipped with 5 mm TCI cryoprobe. Lipids were solubilised in EtOD, at a concentration of 5 mg/mL, while LNPs formulations were diluted (3 to 1) with D_2O.

^{1}H-NMR of LNPs were acquired using the Bruker "noesypr1d" pulse programme, with the following parameters: number of scans 32, relaxation delay 12s, time domain 32k points and a

spectral width of 11 ppm with transmitter offset ppm 4.7. ^{1}H-NMR of lipids was acquired using the "stegp1s1d" pulse programme, with 512 number of scans, relaxation delay 12s, time domain 32k points and a spectral width of 18 ppm.

5.2.7. Transmission Electron Microscopy

To investigate the structure and the morphology of the LNPs formulations, TEM was performed. TEM analyses were carried out on a Jeol JEM 2100 Plus, operated at an accelerating voltage of 200 kV. The instrument was equipped with a Gatan Rio 8-megapixel Complementary Metal-Oxide-Semiconductor (CMOS) camera (Gatan, USA).

5.2.8. Nanoparticle tracking analysis

Nanoparticle tracking analysis was performed using a NanoSight (NS300, Malvern Panalytical Instruments Ltd, UK) to determine the particles number in formulations, size distribution and EE of fluorescent cargo following sample purification. The instrument was equipped with a low volume sample flow cell chamber, a 488-nm laser and a Viton fluoroelastomer O-ring. Samples were introduced onto the chamber using 1 mL syringes, and measurements were conducted at room temperature. For each sample, three measurements were recorded, with each consisting of 1498 frames. Formulations were analysed after dilution at either 1:10.000 or 1:2.000, depending on the lipid concentration used in the preparation.

5.2.9. Lipid quantification Cholesterol Assay

The cholesterol content was determined using a commercially available kit (Sigma-Aldrich). Samples were diluted 1 to 5 with the buffer and deposited into a 96-well plate. Absorbance was measured after 30 minutes using a Versamax Microplate Reader instrument (Molecular device, USA) equipped with SoftMax Pro software, version 5.

5.2.10. Cell studies

Cells studies were conducted to evaluate the ability of the LNPs to cross cell membrane, facilitate intracellular delivery, and assess potential toxicity.

HEK293T wild type (wt) cells, a human embryonic kidney–derived epithelial-like cell line, were grown in Dulbecco's modified Eagle's medium (DMEM) supplemented with 1% penicillin/streptomycin. Cells were seeded in four-well 35-mm glass bottom dishes (four wells for dish) and after 24 hours, were transfected with a pH sensitive construct using lipofectamine 2000. Twelve hours post transfection, 1mL of purified fluorescently labelled- heparin LNPs (with

a final heparin concentration of 0.05mg/mL) was added to each well. Samples were analysed using Zeiss LSM800 confocal laser scanning microscope.

To monitor uptake, heparin was conjugated with Alexa Fluor 488 or Alexa Fluor 405 prior to encapsulation in the LNPs. Control experiments included treatment with fluorescently labelled heparin alone (not encapsulated).

5.3. *Results*

The initial phase of the study on LNP formulations focused on the optimization of experimental parameters. All the formulations were directly analysed by DLS. Various total flow rates (TFR), ranging from 2 to 12 mL/min, as well as various dilution buffer, including acetate buffer (pH 4.5), citrate buffer (pH 5.5), NaCl 0.14 M (pH 6.5), and different lipid concentrations, were evaluated. Formulations prepared using PBS (pH 7.3) as the dilution buffer and NaCl as the solubilization buffer exhibited greater stability and reproducibility over the time and were characterized by single, well defined size distribution. Increasing the TFR led to a progressive reduction in the size of LNPs, reaching a minimum beyond which a further increase in flow rate resulted in higher PDI values. A TFR of 6 mL/min was selected for all the subsequent formulations. These optimized conditions were applied across all formulations discussed in the study. No significant changes in particle size were observed when comparing formulations prepared with different lipid concentrations.

Preliminary tests, conduced in triplicate, demonstrated the reproducibility of the formulation process. *Figure 5-4* shows the results obtained for (*A*) Empty LNPs and (*B*) LNPs containing unfractionated heparin (UFH, 1mg/mL, Hep-LNPs).

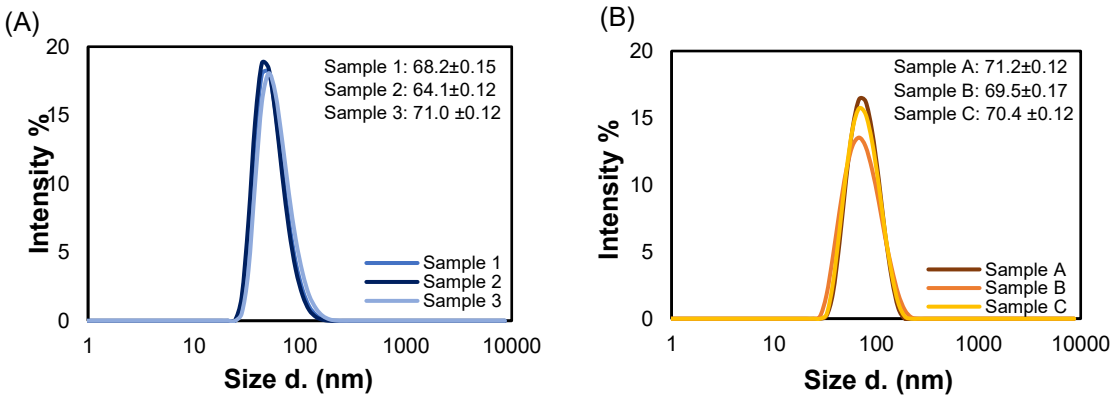

Figure 5- 4: ***DLS results of three different formulations****. A) "Empty"-LNPs and B) Hep(1mg/mL)-LNPs, in terms of average size (d.nm) and intensity of the signals. The average size values and the PDI of the three formulations are reported in each figure.*

The particle size, which is below 100 nm, confirms the potential suitability of these LNPs for biomedical application. Furthermore, the low PDI, below 0.2, indicates a uniform size distribution compatible with therapeutic systems. *In Figure 5-4B*, the Hep-LNPs exhibit a single peak, indicating the absence indicating the absence of any unencapsulated heparin, which size distribution profile at 1mg/mL is shown in *Figure 5-5*.

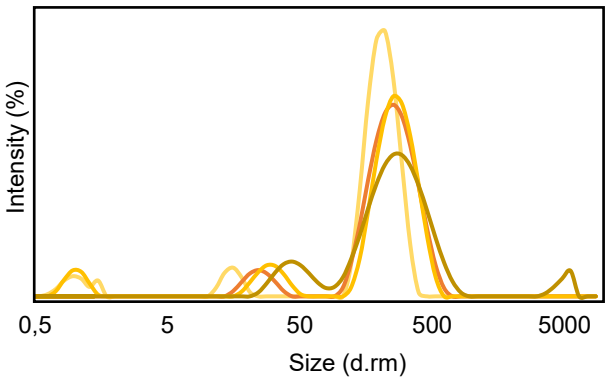

Figure 5- 5: ***Size distribution by intensity of Hep*** *(1mg/mL)*

LNPs were formulated with solution of heparin, PPS and HA at different concentrations (ranging from 0.5 mg/mL to 20 mg/mL) to investigate the influence of the type and concentration of polysaccharides on particles size and PDI. The average size and PDI is reported in *Figure 5-6*.

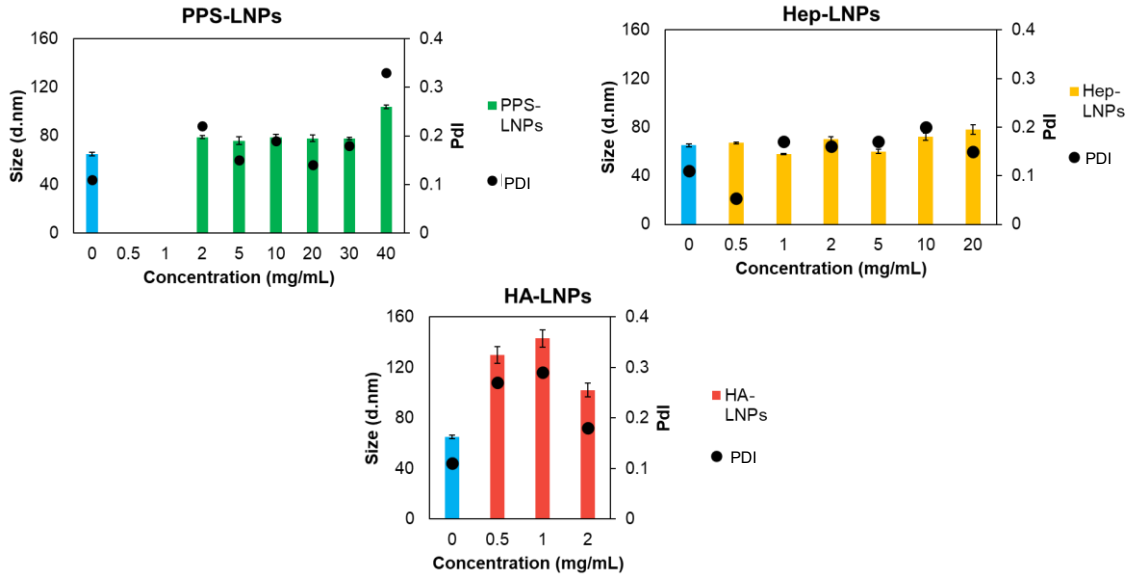

Figure 5- 6: ***The average size values and PDI of PPS-LNPs, Hep-LNPs and HA-LNPs achieved at different concentrations of polysaccharide.*** *The PDI is represented as a black dot, while PPS-LNP are reported in green, Hep-LNPs in yellow and HA-LNPs in red) achieved at different concentration of polysaccharides and compared with Empty-LNPs (reported in light blue).*

LNPs formulations containing PPS and UFH exhibited size similar to those of the empty LNPs, particularly at lower polysaccharide concentrations. Their PDI were slightly higher compared to the Empty LNPs, especially at higher concentration of polysaccharides. In contrast, LNP formulations containing HA presented a higher average size (greater than 120 nm) and higher PDI than empty LNPs. This increase could be related to the larger molecular size of HA which influences the overall size of the LNPs, as demonstrated by Schober B. et al. [181]

Formulations prepared with different types of heparins, including LMWH and Arixtra, a synthetic ultra-low molecular weight heparin ULMWH, are summarised in *Table 5-1*.

Table 5- 1: ***Size and PDI of LNP formulations achieved using different type of heparins*** *(Hep or UFH: unfractionated heparin, LMWH: low molecular weight heparin, ULMWH: ultra-low molecular weight heparin)*

Sample description	Size (d.nm)	PDI
UFH (1mg/ml)	70.4	0.16
LMWH (1mg/ml)	68.4	0.14
ULMWH (1mg/ml)	67.9	0.08

As observed in *Table 5-1*, while the size of the resulting nanoparticles remained largely similar, indicating that variations polysaccharide type was insufficient to increase the size of the LNPs, significant differences in PDI were observed. These differences could be likely attributed to the high polydispersity of the starting polysaccharides.

Subsequent studies focused on Hep-LNPs, as this formulation is more readily available in our laboratories, and has been extensively characterized in previous works. [17],[23],[25],[26]

Zeta potential is another important parameter required from the regulatory agency for the characterisation of LBDDS. This parameter, which depends on the lipids composition, influence the cellular internalisation across the biological barriers. [185]

The Zp of the formulations, both empty and loaded with heparin at 1mg/mL, are reported in *Table 5-2*. These values were also compared to the Zp of heparin alone (concentration of 1mg/mL) and a mixture of empty LNPs with heparin at the same final concentration. Zeta potential is commonly associated with the colloidal stability of nanoparticles. Values near zero suggest low electrostatic repulsion between particles, increasing the risk of aggregation and potentially indicating poor stability. In contrast, higher absolute Zp values, whether positive or negative, are associated with more stable formulations due to greater electrostatic repulsion.

Table 5- 2: ***Zp of Empty and Hep(1mg/mL)-LNPs formulations with their standard deviation****. Results were compared to a heparin formulation at 1mg/mL and a mixture of Empty LNPs and Hep.*

Sample	Zp (mV)	Std. Deviation
Heparin	-14.7	0.98
Empty-LNPs	1.4	0.56
Hep(1mg/mL) LNPs	-3.2	0.69
Empty LNPs and Hep(1mg/mL)	-3.5	0.61

The Zp of both formulations was close to zero, with the Hep (1 mg/mL)-LNPs exhibiting slightly negative value, similar to that of a mixture of empty LNPs and heparin. However, this small shift is insufficient to confirm the presence of the negatively charged heparin molecules, which alone exhibit a highly negative Zp, on the nanoparticle surface.

Despite the low Zp values observed, the formulation remained stable over time, *Figure 5-8*, suggesting that factors other than surface charge may contribute to stability.

Several phenomena can explain the near neutral Zp:

- The high ionic strength of the medium compresses the electrical double layer surrounding the LNPs. This reduces the measured Zp, effectively masking the true surface charge.
- The charge of the LNPs surface is hidden by the presence of the polymer layer, additionally the presence of PEG lipids can reduce their mobility, and consequently their Zp. [73]
- Finally, the presence of cationic lipid components that are not fully protonated under acidic conditions may result in a lower net surface charge.

The latter hypothesis was considered the most likely. This was confirmed by measuring Zp under acidic conditions using citrate buffer at pH 4.5. Under these conditions, empty LNPs displayed a positive Zp (+27 mV) whereas LNPs containing heparin and exhibit a negative Zp (-16 mV).

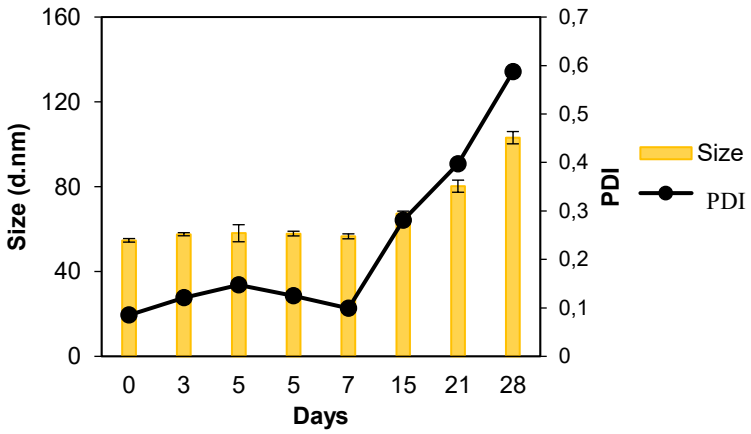

Figure 5- 7: ***Stability over the time*** *of Hep(1mg/mL)-LNPs at 4°C.*

As shown in *Figure 5-7*, the formulation remained stable in terms of particle size and PDI for the first 15 days. After this period, a significant increase in PDI was observed, indicating the onset of instability. A similar trend was also observed for empty LNPs. At higher temperatures, such as 25°C, aggregation occurred more rapidly.

5.3.1. Evaluation of the lipid concentration

Formulations were also prepared using different lipid concentrations. *Table 5-3* reports the corresponding hydrodynamic size and PDI of the LNPs:

Table 5- 3: ***Influence of the concentration of the lipids on the size and PDI of Hep(0.5mg/mL) LNPs***

Lipid concentration (mg/mL)	Size (d.nm)	PDI
0.5 mg/mL	65.1	0.05
1.0 mg/mL	69.9	0.17

An increase in lipid concentration from 0.5 mg/mL to 1.0 mg/mL resulted in a slight increase in the average particle size (from 65.14 nm to 69.89 nm) and in the polydispersity index, which rose from 0.046 to 0.168. This suggests a less uniform size distribution at higher lipid concentrations, potentially due to increased aggregation or less controlled nanoparticle self-assembly during formulation. Nevertheless, the size and PDI values observed at higher lipid concentrations remain within the range suitable for biomedical applications.

5.3.2. Cholesterol Assay for the cholesterol quantification

The cholesterol content of the formulations was evaluated using a commercially available colorimetric cholesterol assay. The method was optimized, and several different dilutions were tested, allowing the determination of the optimal conditions that provided accurate quantification. The measured values were compared to the theorical cholesterol content, showing good agreement. In particular, the deviation from theoretical values was below 8% for both empty LNPs and Hep-LNPs.

It was also assumed that the other lipid components were present in the expected ratios, as defined during formulation, even though they were not directly quantified.

5.3.3. NMR spectroscopy of the LNPs

NMR spectroscopy is often used for the characterization of the nanoparticles structure. [187], [188]

LNPs were investigated with proton NMR spectroscopy. *Figure 5-8* shows the typical spectrum of Empty-LNPs (green spectrum). The major component corresponds to D-Lin-MC3-DMA (shown in blue), which is present at the highest molar ratio among the lipids. The spectra of LNPs is also characterized by signal broadening, which is consistent with the complexation of lipids in an aqueous environment and the subsequent formation of micelle-like supramolecular structures. ^{1}H NMR spectrum of Hep-LNPs (not shown) primarily show the lipid components, rendering this technique unsuitable for direct demonstrating drug encapsulation.

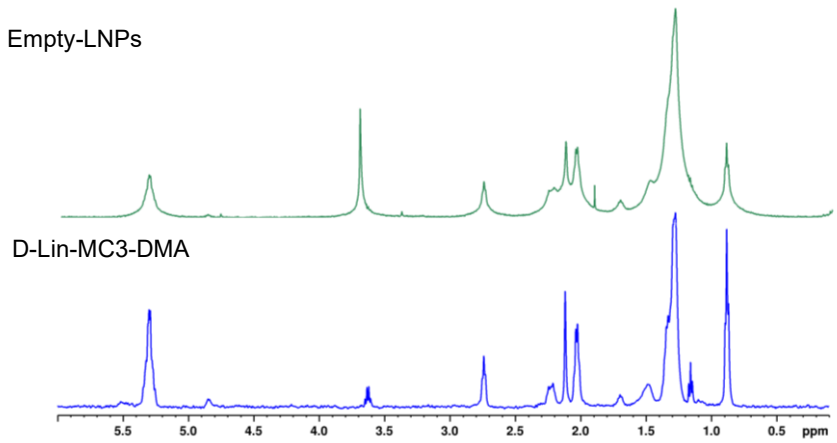

Figure 5- 8: ***^{1}H NMR of empty-LNPs*** *(green),* ***and Dlin-MC3-DMA*** *(Blu)*

5.3.4. Purification

5.3.4.1. Dialysis

Several methods to purify LNPs were evaluated, and the extent of polysaccharide encapsulation was assessed. One of the purification strategies employed was dialysis using membranes with a molecular weight cut-off (MWCO) of 25kDa. A control experiments with a heparin solution demonstrated that at least two weeks, with several buffer changes, were required to remove the majority of the polysaccharide. Furthermore, significant aggregation of LNPs was observed during the dialysis in water. This method was, however, effective for the rapid removal of the ethanol.

5.3.4.2. Centrifugal filtration

Centrifugal filtration using 100kDa MWCO membranes was found to be ineffective. The process was a time-consuming leading to sample aggregation and resulted in a significant sample loss through the membrane, as demonstrated by the size analysis.

5.3.4.3. Size exclusion chromatography

Several resins were tested for the purification of the LNPs, with Sepharose CL4B proving to be the most effective. *Figure 5-9* shows the typical elution profiles acquired at 210 nm. Empty LNPs and the formulation containing heparin at a low concentration (*Figure 5-9A*) were characterised by a single monodisperse peak. Differences in peak intensity were also observed between formulations prepared with different concentration of the lipid mixture, *Figure 5-9A*.

In contrast, the elution of heparin(5mg/mL)-LNPs exhibited two peaks, indicating that not all the heparin was encapsulated, *Figure 5-9B*. The first peak corresponds to the LNPs encapsulating heparin, while the second peak indicated the presence of free polysaccharides.

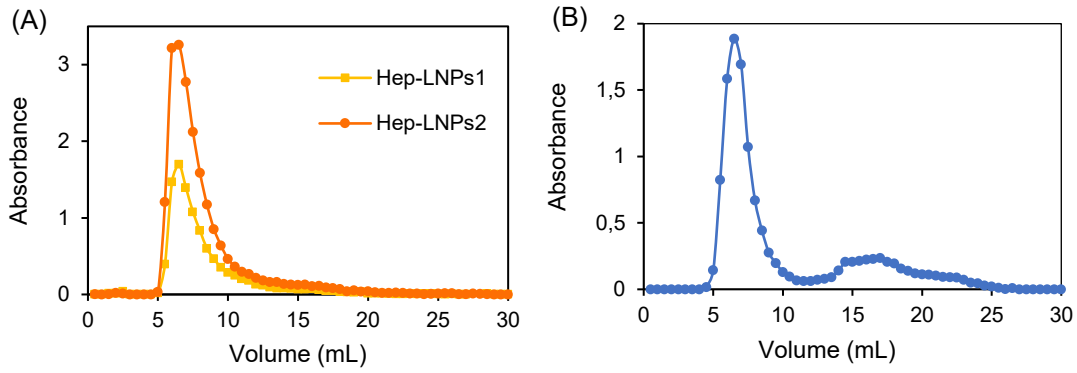

Figure 5- 9: ***Elution profiles of LNPs formulations****. (A) Elution profiles of LNPs with Hep 1mg/mL formulations achieve at different concentration of lipids,* ●*Hep-LNPs1 (3mg/mL) and* ● *Hep-LNPs2 (6mg/mL). (B) Elution profile of Hep-LNPs at 5mg/mL.*

Studies on formulations containing heparin at concentrations below 3 mg/ml encountered difficulties in the detection of the free polysaccharide. Furthermore, the purification process caused dilution of the LNP formulations, complicating the characterisation with techniques in which dilution reduces signal intensity. Examples include NMR spectroscopy, HP-SEC/TDA and UV, in which the free heparin was unquantifiable.

5.3.5. Transmission electron microscopy

Transmission electron microscopy (TEM) was employed to investigate the morphology and structure of the lipid nanoparticles (LNPs), as these characteristics can influence circulation time, payload delivery and cell internalisation.

It should be noted that TEM analysis can induce structural changes in LNPs due to the staining and dehydration that occur during sample preparation. *Figures 5–10* show the TEM images of the Hep-LNPs before (*Figure 5-10 A*) and after purification (*Figure 5-10 B* and *C*). The nanoparticles maintained their spherical shape following purification, indicating that during the purification process do not alter the LNP structure.

Additionally, the observed sizes are consistent with the DLS results. The presence of an electron-dense core inside the LNPs suggests successful encapsulated of the material (*Figure 5-10C*).

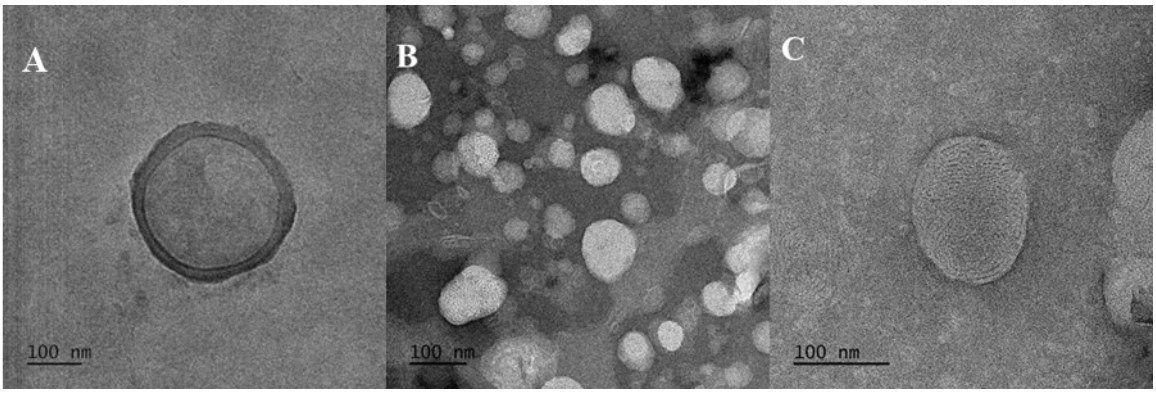

Figure 5- 10: ***TEM images of Hep(1mg/mL)- LNPs*** *of (A) unpurified formulation, (B) and (C) purified formulations.*

5.3.6. Stability after purification

Size distribution analysis performed after purification, showed similar particle size and PDI values compared to formulations prior purification.

Furthermore, the stability of the purified sample was determined at different temperatures (4°C, and 37°C), the results are reported in *Figure 5-11*.

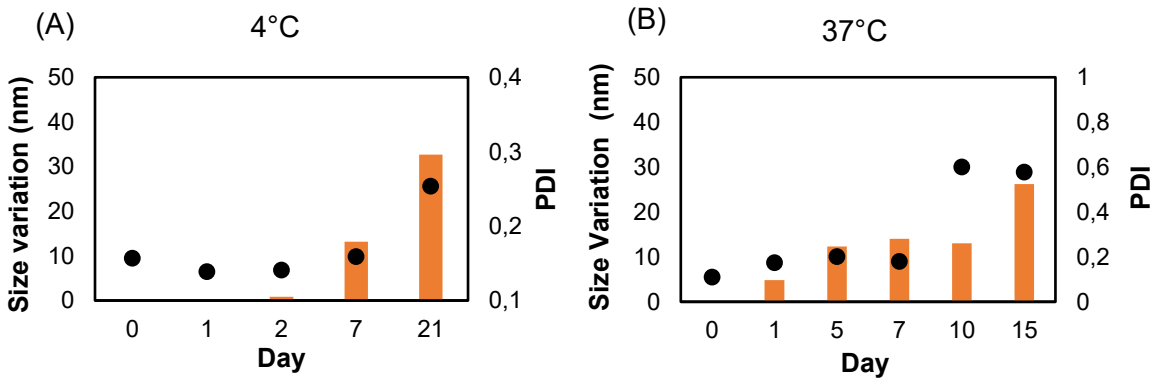

*Figure 5- 11:****Stability of purified Hep-LNPs formulations at 4°C and 37°C.*** *(A) Stability profile of purified Hep-LNPs stored at 4°C over time. (B) Stability profile of purified Hep-LNPs stored at 37°C over time. In both graphs, particle size and polydispersity index (PDI) are reported to assess formulation stability.*

As observed in *Figure 5-11*, the purified LNP formulation remained stable, without significative variation of size and PDI over a period of approximately 10 to 20 days, according to the temperature. The significative variation of size and PDI were attributed to aggregation phenomena and consequently leaking of the active content.

Notably, the formulation remained stable not only at 4°C but also at 37°C. At 37°C, an increase in PDI was observed after 10 days, indicating a reduction in nanoparticles population

homogeneity. However, the mean particle size remained relatively constant, with variations below 30 nm. In contrast, formulations stored at 4°C maintained stability for up to 21 days, exhibiting by only a slight increase in particle size and a PDI consistently around 0.3.

5.3.7. Synthesis of fluorescent heparin

Fluorescently labelled heparin was synthesised to enable detailed studies of LNPs, particularly to determine encapsulation efficiency (EE) and to investigate their interactions with cells.

Several fluorescently labelled heparins were synthesised, with the choice of fluorophore depending on the intended application, required quantity and the cost. For cellular studies, heparins were conjugated with Alexa Fluor 488 and Alexa Fluor 405. In contrast, FITC-labelled heparin was used to determine EE.

All reactions were optimized, and *Table 5-4* summarised the different experiments and conditions tested for the functionalization of heparin with Alexa Fluor 405.

Table 5- 4: ***Synthesis condition of heparin functionalized with Alexa Fluor 405***

Reaction	Temperature (°C)	pH	Eq. NHS	Eq. EDC	% of functionalization
1	0	6.5	-	0.1	0.006
2	25	6.5	-	0.1	0.008
3	25	6.5	0.1	0.1	0.017
4	25	6.5	2.0	2.0	0.036
5	25	8.5	2.0	2.0	0.044
6	25	8.5	4.0	4.0	0.879

Eq: equivalents; NHS: N-hydroxysuccinimide; EDC: 1-Ethyl-3-(3-dimethylaminopropyl) carbodiimide; % of functionalization: determined by UV absorbance after the purification (using ε= 35000 $M^{-1} \cdot cm^{-1}$).

The effect of temperature on the functionalization reaction was evaluated at 0 °C and RT with higher functionalisation observed at 25 °C. The effect of pH was tested in the range between 6.5 and 8.5, with maximum functionalisation occurring at pH 8.5. Furthermore, the use of coupling agents, such as NHS, and increasing the amount of EDC, consistently improved reaction yield.

The optimised reaction conditions were also applied to functionalise heparin with Alexa Fluor 488, achieving a degree of functionalisation of around 0.93 % (ε= 71000 $M^{-1} \cdot cm^{-1}$).

FITC-Heparin was achieved by conjugation with isothiocyanate fluorescein based on Morrison et al. [189] yielding a functionalization degree of about 0.7%.

5.3.8. Nanoparticles tracking analysis

The particle concentration in solution was determined using NTA. This analysis was performed on Hep-LNPs prepared with different polysaccharide contents (1 and 5mg/mL) and with two lipid concentrations (3 mg/mL and 6 mg/mL), to evaluate the influence of lipid and polysaccharide contents on particle counts and size distribution. The results showed that particles number was independent of heparin concentrations. Formulations prepared with 3 mg/mL of lipids, contained approximately 10^{11} particles whereas, the increase of lipid concentration to 6 mg/mL leads to two orders of magnitude increase, reaching approximately 10^{13} particles.

Interestingly, the mean size of LNPs measured by NTA correlated well with the average size obtained by DLS, consistent with previous literature. [65]

The same analysis was performed on purified formulations, revealing particle counts of approximately 10^{8} for a lipid concentration of 3 mg/mL and 10^{10} for 6 mg/mL. These results were consistent with the dilution occurred during the purification process, indicating also that the purification step was effective without significant product loss.

Additionally, NTA allow, using a fluorescence filter for FITC-heparin-LNPs, the direct detection of numerous fluorescent LNPs in purified formulations. This confirmed the successful encapsulation of Heparin demonstrating that the purification process does not result in the loss of the active payload.

5.3.9. Determination of the EE

Identifying a simple and unambiguous method for determining the EE% was challenging. Quantification of free heparin using HP-SEC/TDA, requires multiple steps at very low concentrations, which can lead to sample loss or dispersion.

The determination of native heparin content was attempted using UV spectroscopy; however, the low ε of heparin at an aspecific wavelength (210 nm) and the interference from high salts concentration, resulted in reduced sensitivity of the technique. The issue was resolved by using fluorescently labelled heparin, in particular FITC-heparin, to determine EE%. FITC-heparin can be measured at a specific wavelength (488 nm), compared to the native heparin. This approach enabled reliable the reliable quantification of both encapsulated and non-encapsulated heparin, even at low concentrations of the fluorescent conjugate. The elution profile of FITC-heparin(1mg/mL)-loaded LNPs, acquired by UV-Visible spectroscopy at 488 nm, is shown in *Figure 5-12*. Similar to the other samples, reported in *Figures 5-9*, the profile shows peaks corresponding to LNPs that encapsulate the fluorescent compound, as well as the non-encapsulated material. Evaluating both peaks and knowing the ε of the fluorescent polysaccharides (of about 2860 $M^{*}cm^{-1}$, in PBS pH 7.4), was possible to estimate the EE%, which result to be about 70%.

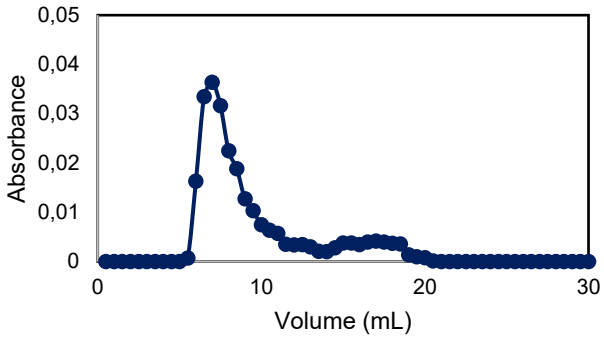

Figure 5- 12: ***Elution profile of FITC-heparin*** *(1 mg/mL)-LNPs at 488 nm*

5.3.10. Cellular Study

Cell studies were performed to evaluate the toxicity of the LNP formulations and determine whether their lipid content enables cellular uptake. To this end, heparin functionalised with Alexa Fluor 488 and Alexa Fluor 405 were encapsulated in the LNPs.

After the confirmation that the cells remained viable for several hours in the presence of the LNP formulations, further experiments were performed using purified LNPs encapsulating the heparin functionalized with the two fluorophores.

Alexa Fluor 405–heparin did not produce intracellular fluorescence. This was attributed to the weaker extinction coefficient of the fluorophore, resulting in insufficient signal after the purification process.

LNPs encapsulating Alexa Fluor 488–heparin produced a detectable intracellular signal, localised in punctate green structures. This indicates that intact vesicle-like carriers had been internalised. Furthermore, the presence of the fluorescent ligand inside the cells became evident, as illustrated in the images in *Figure 5-13.*

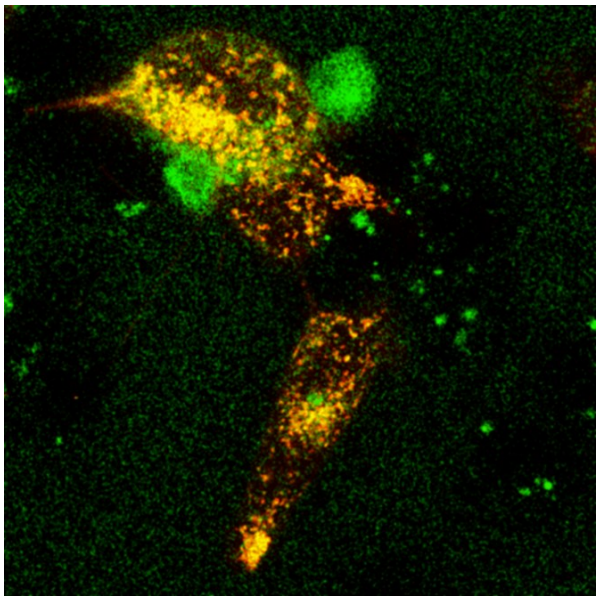

*Figure 5- 13: (**A) Frame from the live-cell imaging results**. HEK293T cells expressing pH-sensitive probes are shown. Lysosomes are highlighted in yellow/orange, while the green spot detected inside the cells represent the fluorescent heparin. Scale bar about 10 µm.*

As observed in *Figure 5-13* from the punctate green signal did not strongly overlap lysosomal signal (yellow/orange). This suggests that, at the imaged time point, most vesicles containing heparin-LNPs had not yet fused with lysosomes.

The distinct green vesicles could represent endocytic compartments or phagosomes, as suggested by their clustering and lack of lysosomal overlap. This interpretation is consistent with a phagocytic or endocytic uptake route, with lysosomal fusion likely occurring at later stages.

Large fluorescent clusters were observed in the medium, indicating potential aggregation of the heparin–LNP formulations.

Control tests performed on free fluorescent heparin (not encapsulated in LNPs) showed that the fluorescent molecule could not be detected inside the cells. In contrast, the use of LNPs enabled the uptake.

Despite the positive preliminary results, new tests are required to understand the biologicals mechanism of action of the LNPs, included time-course imaging to track vesicle maturation and fusion with lysosomes, colocalization assays with established endocytic/lysosomal markers to map the trafficking route, and flow cytometry quantification of uptake efficiency.

5.4. Conclusions

Polysaccharides are natural polymers with several applications in the pharmaceutical field. However, their potential use is limited in many cases by the ease of their degradation, poor ability to reach target sites, and low oral absorption. In order to expand their applications, it was hypothesised that polysaccharides could be encapsulated in lipid nanocarriers. This would provide protection from enzymatic attack, increase their biodistribution and enable targeting to specific sites onto the body. The literature contains reports of successful applications of different types, and for various purposes, demonstrating controlled release and decreased side effects. [59]

To evaluate the scope of the approach, three polysaccharides (HA, PPS and heparin), choose for their different structures and sizes and known for their potential applications as drugs for the treatment of several disease, (i.e. anticancer, antiviral or for the treatment of mucopolysaccharidosis), were encapsulated into LNPs, the latest approved DDS from EMA and FDA, and which has also been approved for the delivery of COVID19 vaccines.

Polysaccharide-loaded LNPs exhibited particle sizes below 100 nm, similar to empty LNPs, with the exception of HA, for which the average size exceeded 120 nm. This observation suggests a relationship between the molecular size of the cargo and the resulting LNP dimensions which merits further investigation. Additionally, the formulations displayed low PDI values, indicating homogeneous particle size distributions. Both parameters (small particle size and low PDI) are essential for ensuring the suitability of the formulation for biomedical applications. Despite their low Zeta potentials, Hep-LNPs exhibited good colloidal stability over time, with a shelf life of up to 10 days, observed both before and after the purification process. A purification method for Hep-LNPs was established; size exclusion chromatography using Sepharose CL-4B resin, was employed to purify the LNP-heparin formulations, which exhibited two peaks in their UV profile. This indicated that not all of the polysaccharide was encapsulated into the nanoparticles. However, the low absorption coefficient of heparin and the high salt concentration limited the sensitivity of this technique, preventing determination of the encapsulated material. Using fluorescently labelled heparin enabled the quantification of the encapsulation efficiency. The EE% was about more than the 70% using a heparin concentration of 1 mg/mL. The effective encapsulation was also demonstrated by NTA analysis of purified fluorescent labelled heparin encapsulated in LNPs.

It was demonstrated that the formulations remained stable in terms of size and PDI, for at least 15 days at 4°C following purification, and also for seven days at 37°C.

Finally, preliminary biological tests demonstrated that this drug delivery system can enable the cellular uptake of the cargo. However, further investigations of the biological mechanism required additional analysis and optimisation of the formulations to minimise extracellular aggregation. The next steps of the project should involve the evaluation of targeted uptake strategies, achieved

by modifying the surface of the LNPs with molecules to target specific cell surface receptors, for example incorporating N-linked sugars, O-linked glycosaminoglycans, or peptide/protein ligands, to enable receptor-mediated endocytosis. Further future work should also focus on undertaking more detailed studies of other types of cargo, and the determining of the composition of the encapsulated materials.

Chapter 6

CONCLUSIONS

The derivatisation of polysaccharides is often used to improve their pharmacokinetic and pharmacodynamics properties and, the primary objective of this thesis was to explore the feasibility of derivatising and characterising polysaccharides for applications in the functionalisation of biomaterials.

Hyaluronic acid, modified with an amino derivative of lactose, denoted HYLACH®, was designed and synthetised in order to interact specifically with galectin-3, a galactose-binding lectin involved in idiopathic pulmonary fibrosis. The characterisation of the biopolymer and the determination of the degree of substitution necessitate the development of a bidimensional NMR method with which to study the hydrolysed products. The presence of the lactose moiety led to an increase in affinity towards Gal-3, as demonstrated by interaction studies, demonstrating the potential of HYLACH® as a therapeutic drug for the treatment of IPF. This modification resulted, however, in a decrease in the solubility of the biopolymer and a substantial decrease in its viscosity in proportion to the increase of its degree of functionalisation.

The second part of the project involved the study of the interaction between pentosan polysulphate and platelet factor 4 with analytical orthogonal techniques. PPS is a semi-synthetic polysaccharide, which shares structural similarities with heparin and, again, like heparin interacts with PF4, the protein involved in heparin-induced thrombocytopenia (HIT) which is the major adverse effect associated with heparin use. Physico-chemical techniques demonstrated that the PPS/PF4 aggregates were smaller than heparin/PF4 aggregates and, it is known that the risk of heparin-induced thrombocytopenia relates to the size of the aggregate formed, nevertheless, the enzyme immunoassay analysis demonstrated that PPS provokes comparable interactions with PF4. This indicated that not only the size of the aggregate as a defining factor in HIT but, also that the protein/ligand interaction is more complex than thought. Additionally, these results suggested that new parenteral application of PPS should be carefully evaluated and indicates that detailed studies and monitoring of potential thrombocytopenia effects, including the pharmacokinetics of this polysaccharide, are required.

The final chapter of this thesis involved designing and formulation a delivery system for polysaccharides, in order to increase their shelf life, facilitate a controlled release over time and enable the use of reduced doses, thereby reducing potential adverse effects. LNPs were selected as a promising candidate for a potential polysaccharide carrier. Their efficient cargo encapsulation, small size, low polydispersity, and stability over time have been demonstrated as

fundamental parameters for clinical use. LNPs formulated using microfluidic systems were found to be spherical in shape with a size below 100 nm and a low polydispersity index.

Furthermore, biological tests, based on fluorescently labelled heparin encapsulated in LNPs, demonstrated that the cargo can penetrate living cells. The encapsulation of material was, however, only demonstrated at low concentrations of polysaccharide. The purification process led to considerable dilution of the formulation, resulting in low final concentration of the polysaccharide. Nevertheless, lipid nanoparticles have been identified as a potential system for the administration of polysaccharides, particularly owing to their ability to be delivered to specific areas and their known capacity to cross the blood-brain barrier.

Looking to the future, the encapsulation of polysaccharide in lipid nanoparticles systems for anticancer purposes or, for the treatment of specific disease, can now be considered, taking advantage of the possibility of carrying out controlled release to targeted areas of the body.

Modification of the external surface of the nanoparticles can also be considered for this purpose.

REFERENCES

[1] S. W. Cui *et al.*, *Methodology for Structural Analysis of Polysaccharides*. 2018.

[2] Y. Yu *et al.*, "Biological activities and pharmaceutical applications of polysaccharide from natural resources: A review," *Carbohydr. Polym.*, vol. 183, no. 235, pp. 91–101, 2018, doi: 10.1016/j.carbpol.2017.12.009.

[3] A. S. A. Mohammed *et al.*, "Polysaccharides; Classification, Chemical Properties, and Future Perspective Applications in Fields of Pharmacology and Biological Medicine (A Review of Current Applications and Upcoming Potentialities)," *J. Polym. Environ.*, vol. 29, no. 8, pp. 2359–2371, 2021, doi: 10.1007/s10924-021-02052-2.

[4] J. Liu *et al.*, "A review of bioactive plant polysaccharides: Biological activities, functionalization, and biomedical applications," *Bioact. Carbohydrates Diet. Fibre*, vol. 5, no. 1, pp. 31–61, 2015, doi: 10.1016/j.bcdf.2014.12.001.

[5] R. K. Srivastava *et al.*, *Sources and industrial applications of polysaccharides*. INC, 2020.

[6] E. Díaz-Montes, "Polysaccharides: Sources, Characteristics, Properties, and Their Application in Biodegradable Films," *Polysaccharides*, vol. 3, no. 3, pp. 480–501, 2022, doi: 10.3390/polysaccharides3030029.

[7] J. Necas *et al.*, "Hyaluronic acid (hyaluronan): A review," *Vet. Med. (Praha).*, vol. 53, no. 8, pp. 397–411, 2008, doi: 10.17221/1930-VETMED.

[8] C. E. Schanté *et al.*, "Chemical modifications of hyaluronic acid for the synthesis of derivatives for a broad range of biomedical applications," *Carbohydr. Polym.*, vol. 85, no. 3, pp. 469–489, 2011, doi: 10.1016/j.carbpol.2011.03.019.

[9] K. Yoshida *et al.*, "United States Patent," 1975.

[10] S. Vasvani *et al.*, "Hyaluronic acid: A review on its biology, aspects of drug delivery, route of administrations and a special emphasis on its approved marketed products and recent clinical studies," *International Journal of Biological Macromolecules*, vol. 151. Elsevier B.V., pp. 1012–1029, May 15, 2020, doi: 10.1016/j.ijbiomac.2019.11.066.

[11] A. Basu *et al.*, "Polysaccharide-Based Conjugates for Biomedical Applications," *Bioconjug. Chem.*, vol. 26, no. 8, pp. 1396–1412, 2015, doi: 10.1021/acs.bioconjchem.5b00242.

[12] Future Market Insights, "Hyaluronic Acid Products Market," 2025. https://www.futuremarketinsights.com/reports/hyaluronic-acid-products-market.

[13] K. Girish *et al.*, "Hyaluronidase Inhibitors: A Biological and Therapeutic Perspective," *Curr. Med. Chem.*, vol. 16, no. 18, pp. 2261–2288, 2009, doi: 10.2174/092986709788453078.

[14] C. E. Schanté *et al.*, "Improvement of hyaluronic acid enzymatic stability by the grafting of amino-acids," *Carbohydr. Polym.*, vol. 87, no. 3, pp. 2211–2216, 2012, doi: 10.1016/j.carbpol.2011.10.050.

[15] D. M. H. Beurskens *et al.*, "The Anticoagulant and Nonanticoagulant Properties of Heparin," *Thromb. Haemost.*, vol. 120, no. 10, pp. 1371–1383, 2020, doi: 10.1055/s-0040-1715460.

[16] E. I. Oduah *et al.*, "Heparin: Past, present, and future," *Pharmaceuticals*, vol. 9, no. 3, pp. 1–12, 2016, doi: 10.3390/ph9030038.

[17] B. Casu *et al.*, “Re-visiting the structure of heparin,” *Carbohydr. Res.*, vol. 403, pp. 60–68, 2015, doi: 10.1016/j.carres.2014.06.023.

[18] C. Hao *et al.*, *Heparin: An essential drug for modern medicine*, 1st ed., vol. 163. Elsevier Inc., 2019.

[19] D. L. Rabenstein, “Heparin and heparan sulfate: Structure and function,” *Nat. Prod. Rep.*, vol. 19, no. 3, pp. 312–331, 2002, doi: 10.1039/b100916h.

[20] P. Bianchini *et al.*, “Heterogeneity of unfractionated heparins studied in connection with species, source, and production processes,” *Semin. Thromb. Hemost.*, vol. 23, no. 1, pp. 3–10, 1997, doi: 10.1055/s-2007-996063.

[21] M. Iacomini *et al.*, “‘Linkage region’ sequences of heparins and heparan sulfates: Detection and quantification by nuclear magnetic resonance spectroscopy,” *Anal. Biochem.*, vol. 274, no. 1, pp. 50–58, 1999, doi: 10.1006/abio.1999.4230.

[22] U. Lindahl *et al.*, “Evidence for a 3-O-sulfated D-glucosamine residue in the antithrombin-binding sequence of heparin,” *Proc. Natl. Acad. Sci. U. S. A.*, vol. 77, no. 11 I, pp. 6551–6555, 1980, doi: 10.1073/pnas.77.11.6551.

[23] R. Lever *et al.*,, Heparin- A century of Progress, vol. 207. Springer, 2012.

[24] C. J. Mycroft-West *et al.*, “Heparin Inhibits Cellular Invasion by SARS-CoV-2: Structural Dependence of the Interaction of the Spike S1 Receptor-Binding Domain with Heparin,” *Thromb. Haemost.*, vol. 120, no. 12, pp. 1700–1715, 2020, doi: 10.1055/s-0040-1721319.

[25] S. Bertini *et al.*, “Characterization of PF4-Heparin Complexes by Photon Correlation Spectroscopy and Zeta Potential,” *Clin. Appl. Thromb.*, vol. 23, no. 7, pp. 725–734, 2017, doi: 10.1177/1076029616685430.

[26] B. Casu and U. Lindahl, “Structure and biological interactions of heparin and heparan sulfate,” *Adv. Carbohydr. Chem. Biochem.*, vol. 57, pp. 159–206, 2001, doi: 10.1016/S0065-2318(01)57017-1.

[27] L. Nallaguntla *et al.*, “Preparation and evaluation of a novel oral delivery system for low molecular weight heparin,” *Int. J. Pharm. Investig.*, vol. 6, no. 3, p. 148, 2016, doi: 10.4103/2230-973x.187351.

[28] T. D. Kim *et al.*, “Studies on liposome-encapsulated heparin,” *Thromb. Res.*, vol. 43, no. 6, pp. 603–612, 1986, doi: 10.1016/0049-3848(86)90097-6.

[29] X. Yang *et al.*, “Strategies for sustained release of heparin: A review,” *Carbohydr. Polym.*, vol. 294, no. April, p. 119793, 2022, doi: 10.1016/j.carbpol.2022.119793.

[30] A. Yildiz-Pekoz and Y. Ozsoy, “Inhaled Heparin: Therapeutic Efficacy and Recent Formulations,” *J. Aerosol Med. Pulm. Drug Deliv.*, vol. 30, no. 3, pp. 143–156, 2017, doi: 10.1089/jamp.2015.1273.

[31] A. Alekseeva *et al.*, “In-depth structural characterization of pentosan polysulfate sodium complex drug using orthogonal analytical tools,” *Carbohydr. Polym.*, vol. 234, no. July 2019, 2020, doi: 10.1016/j.carbpol.2020.115913.

[32] L. DeFerra, A. Naggi, and Z. Maurizio, “WO 2014/114723 A1 Method for the qualification of preparation of pentosan polysulphate, raw materials and production processes thereof,” 2014.

[33] G. Eisele *et al.*, “Further advances in identification of pentosan polysulfate monosaccharide composition by NMR,” *J. Pharm. Biomed. Anal.*, vol. 235, no. August, p. 115672, 2023, doi: 10.1016/j.jpba.2023.115672.

[34] A. M. Fischer *et al.*, “Comparison between the effect of pentosan polysulphate heparin and antithrombin III injections in antithrombin III deficient patients,” *Thromb. Res.*, vol. 37, no. 2, pp. 295–307, 1985, doi: 10.1016/0049-3848(85)90018-0.

[35] P. Hwang, *et al.*, “Efficacy of pentosan polysulfate in the treatment of interstitial cystitis: a meta-analysis,” *Adult Urol.*, vol. 50, no. 1, pp. 40–43, 1997, doi: 10.1097/00005392-199803000-00038.

[36] “Pentosan polysulfate sodium-NDA reference number 020193,” 1996. .

[37] C. L. Parsons *et al.*, “A quantitatively controlled method to study prospectively interstitial cystitis and demonstrate the efficacy of pentosanpolysulfate,” *J. Urol.*, vol. 150, no. 3, pp. 845–848, 1993, doi: 10.1016/S0022-5347(17)35629-X.

[38] P. C. Sadhukhan *et al.*, “Sodium pentosan polysulfate reduces urothelial responses to inflammatory stimuli via an indirect mechanism,” *J. Urol.*, vol. 168, no. 1, pp. 289–292, 2002, doi: 10.1016/S0022-5347(05)64909-9.

[39] M. Asperti *et al.*, “Pentosan polysulfate to control hepcidin expression in vitro and in vivo,” *Biochem. Pharmacol.*, vol. 175, no. December 2019, p. 113867, 2020, doi: 10.1016/j.bcp.2020.113867.

[40] M. Rusnati *et al.*, “Pentosan Polysulfate as an Inhibitor of Extracellular HIV-1 Tat,” *J. Biol. Chem.*, vol. 276, no. 25, pp. 22420–22425, 2001, doi: 10.1074/jbc.M010779200.

[41] S. Bertini *et al.*, “Pentosan Polysulfate Inhibits Attachment and Infection by SARS-CoV-2 in Vitro: Insights into Structural Requirements for Binding,” *Thromb. Haemost.*, vol. 122, no. 6, pp. 984–997, 2022, doi: 10.1055/a-1807-0168.

[42] E. H. Schuchman *et al.*, “Pentosan Polysulfate: A Novel Therapy for the Mucopolysaccharidoses,” *PLoS One*, vol. 8, no. 1, 2013, doi: 10.1371/journal.pone.0054459.

[43] V. R. Anderson and C. M. Perry, “Pentosan polysulfate: A review of its use in the relief of bladder pain or discomfort in interstitial cystitis,” *Drugs*, vol. 66, no. 6, pp. 821–835, 2006, doi: 10.2165/00003495-200666060-00006.

[44] A. Lindeke-Myers *et al.*, “Pentosan polysulfate maculopathy,” *Surv. Ophthalmol.*, vol. 67, no. 1, pp. 83–96, 2022, doi: 10.1016/j.survophthal.2021.05.005.

[45] P. Tomasik, “Chemical modifications of polysaccharides,” *Chem. Funct. Prop. Food Saccharides*, vol. 2013, pp. 123–130, 2003, doi: 10.1155/2013/417672.

[46] S. Li *et al.*, “Molecular Modification of Polysaccharides and Resulting Bioactivities,” *Compr. Rev. Food Sci. Food Saf.*, vol. 15, no. 2, pp. 237–250, 2016, doi: 10.1111/1541-4337.12161.

[47] European Medicines Agency, “European Pharmacopoeia.”

[48] S. J. Williams and G. J. Davies, “Protein-carbohydrate interactions: Learning lessons from nature,” *Trends Biotechnol.*, vol. 19, no. 9, pp. 356–362, 2001, doi: 10.1016/S0167-7799(01)01699-7.

[49] C. Y. Lee and T. R. Lee, “Carbohydrate-Protein Interactions: Basis of Glycobiology,” *Acc. Chem. Res.*, vol. 28, no. 8, pp. 321–327, 1995.

[50] M. J. Bernhard *et al.*, “Time-Dependent Fluorescence Spectroscopy to Quantify Complex Binding Interactions,” *ACS Omega*, vol. 5, no. 45, pp. 29017–29024, Nov. 2020, doi: 10.1021/acsomega.0c03416.

[51] S. Zhang *et al.*, “Carbohydrate-Protein Interactions : Advances and Challenges,” *Commun.*

Inf. Syst., vol. 21, no. 1, pp. 1–12, 2021, doi: 10.4310/cis.2021.v21.n1.a7.Carbohydrate-Protein.

[52] Y. K. Song and C. K. Kim, "Topical delivery of low-molecular-weight heparin with surface-charged flexible liposomes," *Biomaterials*, vol. 27, no. 2, pp. 271–280, 2006, doi: 10.1016/j.biomaterials.2005.05.097.

[53] S. M. Mawazi, *et al.*, "Niosome Preparation Techniques and Structure—An Illustrated Review," *Pharmaceutics*, vol. 17, no. 1, 2025, doi: 10.3390/pharmaceutics17010067.

[54] P. Chivte *et al.*, Biological Methods for Drug Delivery, vol. 26. *Springer Nature Singapore*, 2023.

[55] M. K. Kataria *et al.*, "Liposome: An art for drug delivery," *Int. J. Pharm. Sci. Lett.*, vol. 5, no. 2, pp. 523–530, 2015.

[56] J. Pardeike *et al.*, "Lipid nanoparticles (SLN, NLC) in cosmetic and pharmaceutical dermal products," *Int. J. Pharm.*, vol. 366, no. 1–2, pp. 170–184, 2009, doi: 10.1016/j.ijpharm.2008.10.003.

[57] A. M. Kyrychenko and O. H. Kovalenko, "Prospects of Liposomes Application in Agriculture," *Mikrobiol. Zh.*, vol. 87, no. 1, pp. 72–82, 2025, doi: 10.15407/microbiolj87.01.072.

[58] T. M. Taylor *et al.*, "Liposomal nanocapsules in food science and agriculture," *Crit. Rev. Food Sci. Nutr.*, vol. 45, no. 7–8, pp. 587–605, 2005, doi: 10.1080/10408390591001135.

[59] R. Tenchov, *et al.*, "Lipid Nanoparticles from Liposomes to mRNA Vaccine Delivery, a Landscape of Research Diversity and Advancement," *ACS Nano*, vol. 15, no. 11, pp. 16982–17015, 2021, doi: 10.1021/acsnano.1c04996.

[60] B. N. Aldosari, *et al.*, "Lipid nanoparticles as delivery systems for RNA-based vaccines," *Pharmaceutics*, vol. 13, no. 2, pp. 1–29, 2021, doi: 10.3390/pharmaceutics13020206.

[61] Y. Xiao and J. Shi, "Lipids and the Emerging RNA Medicines," *Chem. Rev.*, vol. 121, no. 20, pp. 12109–12111, 2021, doi: 10.1021/acs.chemrev.1c00778.

[62] H. N. Jung *et al.*, "Lipid nanoparticles for delivery of RNA therapeutics: Current status and the role of in vivo imaging," *Theranostics*, vol. 12, no. 17, pp. 7509–7531, 2022, doi: 10.7150/thno.77259.

[63] M. Maeki *et al.*, "Microfluidic technologies and devices for lipid nanoparticle-based RNA delivery," *J. Control. Release*, vol. 344, no. October 2021, pp. 80–96, 2022, doi: 10.1016/j.jconrel.2022.02.017.

[64] U.S. Department of Health and Human Services and F. and D. Administration, "Liposome Drug Products Chemistry, Manufacturing, and Controls; Human Pharmacokinetics and Bioavailability; and Labeling Documentation," 2018. http://www.fda.gov/Drugs/GuidanceComplianceRegulatoryInformation/Guidances/default.htm.

[65] S. S. Nogueira *et al.*, "Analytical techniques for the characterization of nanoparticles for mRNA delivery," *Eur. J. Pharm. Biopharm.*, vol. 198, no. January, p. 114235, 2024, doi: 10.1016/j.ejpb.2024.114235.

[66] Y. Fan *et al.*, "Analytical characterization of liposomes and other lipid nanoparticles for drug delivery," *J. Pharm. Biomed. Anal.*, vol. 192, 2021, doi: 10.1016/j.jpba.2020.113642.

[67] O. Coskun, "Separation Tecniques: CHROMATOGRAPHY," *North. Clin. Istanbul*, vol. 3, no. 2, pp. 156–160, 2016, doi: 10.14744/nci.2016.32757.

[68] A. M. Striegel *et al.*, "Modern Size-Exclusion Liquid Chromatography," *Mod. Size-Exclusion Liq. Chromatogr.*, 2009, doi: 10.1002/9780470442876.

[69] C. Hill *et al.*, Handbook of size exclusion chromatography, vol. 316, no. 3. 1995.

[70] Malvern Instruments Ltd., Viscotek 305 TDA User manual, Man0420-04 ed. 2016.

[71] S. Mori and H. G. Barth, Size Exclusion Chromatography. *Springer*, 1999.

[72] S. Bertini, *et al.*, "Molecular weight determination of heparin and dermatan sulfate by size exclusion chromatography with a triple detector array," *Biomacromolecules*, vol. 6, no. 1, pp. 168–173, 2005, doi: 10.1021/bm049693s.

[73] K. Williams, "Malvern Panalytical," 2018. https://www.malvernpanalytical.com/en/learn/knowledge-center/insights/waters-and-malvern-panalytical-partner-for-complete-high-resolution-polymer-characterization.

[74] Malvern Instruments Ltd., *OMNISEC System User Guide*, MAN0550-11th ed. 2023.

[75] A. M. J. J. Bonvin, R. Boelens, and R. Kaptein, "NMR analysis of protein interactions," *Curr. Opin. Chem. Biol.*, vol. 9, no. 5, pp. 501–508, 2005, doi: 10.1016/j.cbpa.2005.08.011.

[76] A. Randazzo, *Guida pratica all'interpretazione di spettri NMR*. 2018.

[77] Agilent Technologies, "The Basics of UV-Vis Spectrophotometry," *The basics of UV-Vis Spectrophotometry*, p. 36, 2021.

[78] H. Yadav *et al.*, *Sophisticated techniques for characterization of polysaccharide hydrogels*, no. April. 2023.

[79] A. Pooja, Chawla, *Modern Pharmaceutical Analysis Techniques*. Pharma Med Press, 2024.

[80] A. K. Biswas, *et al.*, "A simple UV-Vis spectrophotometric method for determination of β-carotene content in raw carrot, sweet potato and supplemented chicken meat nuggets," *Lwt*, vol. 44, no. 8, pp. 1809–1813, 2011, doi: 10.1016/j.lwt.2011.03.017.

[81] B. C. Smith, *Fundamentals of Fourier transform infrared spectroscopy, Taylor & Francis Group*. 2011.

[82] S. A. Khan, *et al.*, "Fourier transform infrared spectroscopy: Fundamentals and application in functional groups and nanomaterials characterization," *Handb. Mater. Charact.*, pp. 317–344, 2018, doi: 10.1007/978-3-319-92955-2_9.

[83] J. Stetefeld *et al.*, "Dynamic light scattering: a practical guide and applications in biomedical sciences," *Biophys. Rev.*, vol. 8, no. 4, pp. 409–427, 2016, doi: 10.1007/s12551-016-0218-6.

[84] K. S. Schmitz, "Introduction to Dynamic Light Scattering by Macromolecules- Chapter 1," in *Introduction to Dynamic Light Scattering by Macromolecules*, 1990, pp. 1–10.

[85] C. F. Phelps, "Dynamic light scattering, with application to chemistry, biology and physics," *Biochemical Education*, vol. 5, no. 1. p. 22, 1977, doi: 10.1016/0307-4412(77)90025-5.

[86] R. Shaw, "Dynamic Light Scattering Training Achieving reliable nano particle sizing," *ATA Scientific; Malvern*, 2014. http://www.chem.uci.edu/~dmitryf/manuals/Fundamentals/DLS concept.pdf.

[87] S. S. Hallan *et al.*, "Challenges in the physical characterization of lipid nanoparticles," *Pharmaceutics*, vol. 13, no. 4, pp. 1–31, 2021, doi: 10.3390/pharmaceutics13040549.

[88] Malvern panalytical, *Zetasizer nano series, user manual*, MAN0485 Is. 2013.

[89] M. Abe, "Chapter 15 Zeta (ζ) Potential for Micelle and Microemulsion," in *Measurement Techniques and Practices of Colloid and Interface Phenomena*, 2019, pp. 1–145.

[90] B. Carr, M. Wright, and Malvern Instruments Ltd., *Nanoparticle tracking analysis, manual*. 2015.

[91] V. Filipe *et al.*, "Critical evaluation of nanoparticle tracking analysis (NTA) by NanoSight for the measurement of nanoparticles and protein aggregates," *Pharm. Res.*, vol. 27, no. 5, pp. 796–810, 2010, doi: 10.1007/s11095-010-0073-2.

[92] Malvern Instruments Ltd., "Characterizing the size and concentration of liposomes using nanosight pro, Application Note," 2024. https://www.malvernpanalytical.com/en/learn/knowledge-center/application-notes/an240408-characterizing-the-size-and-concentration-of-liposomes.

[93] E. Freire *et al.*, "Isothermal Titration," *Anal. Chem.*, vol. 62, no. 18, pp. 950A-959A, 1990, doi: https://doi.org/10.1021/ac00217a002.

[94] R. J. Falconer, "Applications of isothermal titration calorimetry – the research and technical developments from 2011 to 2015," *J. Mol. Recognit.*, vol. 29, no. 10, pp. 504–515, 2016, doi: https://doi.org/10.1002/jmr.2550.

[95] C. M. Johnson, "Isothermal Titration Calorimetry," in *Methods in Molecular Biology*, vol. 2263, no. 18, 2021, pp. 135–159.

[96] M. L. Doyle, "Characterization of binding interactions by isothermal titration calorimetry," *Curr. Opin. Biotechnol.*, vol. 8, no. 1, pp. 31–35, 1997, doi: https://doi.org/10.1016/S0958-1669(97)80154-1.

[97] S. M. Kelly, *et al.*, "How to study proteins by circular dichroism," *Biochim. Biophys. Acta - Proteins Proteomics*, vol. 1751, no. 2, pp. 119–139, 2005, doi: 10.1016/j.bbapap.2005.06.005.

[98] V. Colaco, *et al.*, "Development of mRNA Lipid Nanoparticles: Targeting and Therapeutic Aspects," *OpenNano*, vol. 15, no. November 2023, p. 100199, 2024, doi: 10.1016/j.onano.2023.100199.

[99] J. Garcia and C. Felip, "Development and optimization of LNP formulations," *Appl. note, KNAUER*.

[100] S. Xu, *et al.*, "Lipid nanoparticles: Composition, formulation, and application," *Mol. Ther. Methods Clin. Dev.*, vol. 33, no. 2, p. 101463, 2025, doi: 10.1016/j.omtm.2025.101463.

[101] S. Sciacchitano *et al.*,, "Galectin-3: One molecule for an alphabet of diseases, from A to Z," *Int. J. Mol. Sci.*, vol. 19, no. 2, 2018, doi: 10.3390/ijms19020379.

[102] C. J. Spagnolo *et al.*, "Idiopathic pulmonary fibrosis: Disease mechanisms and drug development," *Pharmacol. Ther.*, vol. 222, p. 107798, 2021, doi: 10.1016/j.pharmthera.2020.107798.

[103] S. L. Barratt *et al.*, "Idiopathic pulmonary fibrosis (IPF): An overview," *J. Clin. Med.*, vol. 7, no. 8, pp. 1–21, 2018, doi: 10.3390/jcm7080201.

[104] Y.Nishi *et al.*, "Role of galectin-3 in human pulmonary fibrosis," *Allergol. Int.*, vol. 56, no. 1, pp. 57–65, 2007, doi: 10.2332/allergolint.O-06-449.

[105] A. MacKinnon *et al.*, "Regulation of transforming growth factor-β1-driven lung fibrosis by galectin-3," *Am. J. Respir. Crit. Care Med.*, vol. 185, no. 5, pp. 537–546, Mar. 2012, doi: 10.1164/rccm.201106-0965OC.

[106] T. Takehara *et al.*, "Differential Discontinuation Profiles between Pirfenidone and Nintedanib in Patients with Idiopathic Pulmonary Fibrosis," *Cells*, vol. 11, no. 1, p. 143, Jan. 2022, doi: 10.3390/cells11010143.

[107] N. M. Salwowska *et al.*, "Physiochemical properties and application of hyaluronic acid: a systematic review," *Journal of Cosmetic Dermatology*, vol. 15, no. 4. Blackwell Publishing Ltd, pp. 520–526, Dec. 01, 2016, doi: 10.1111/jocd.12237.

[108] A. Donato *et al.*, "The Anti-Inflammatory Effect of Lactose-Modified Hyaluronic Acid Molecules on Primary Bronchial Fibroblasts of Smokers," *Polymers (Basel).*, vol. 15, no. 7, 2023, doi: 10.3390/polym15071616.

[109] A. Donato, *et al.*, "Inhibition of Pro-Fibrotic Molecules Expression in Idiopathic Pulmonary Fibrosis—Derived Lung Fibroblasts by Lactose-Modified Hyaluronic Acid Compounds," *Polymers (Basel).*, vol. 16, no. 1, 2024, doi: 10.3390/polym16010138.

[110] E. M. Dangerfield *et al.*, "Protecting-group-free synthesis of amines: Synthesis of primary amines from aldehydes via reductive amination," *J. Org. Chem.*, vol. 75, no. 16, pp. 5470–5477, 2010, doi: 10.1021/jo100004c.

[111] M. B. Bertini *et al.*, "Molecular Weights of Bovine and Porcine Heparin Samples: Comparison of Chromatographic Methods and Results of a Collaborative Survey," *Molecules*, vol. 22, no. 7, pp. 1–10, 2017, doi: 10.3390/molecules22071214.

[112] A. Harding *et al.*, *Refractive Increment Data-Book, 1st ed.* Nottingham, UK,: Nottingham University Press, 1999.

[113] I. Christiansen-Brams *et al.*, "Synthesis of the 1-Amino-Alditols Derived from Cellobiose, Lactose and Maltose. A Comprehensive NMR Study of Some Alditols and Amino-Alditols," *J. Carbohydr. Chem.*, vol. 11, no. 7, pp. 813–835, 1992, doi: 10.1080/07328309208018272.

[114] M. D'Este *et al.*, "A systematic analysis of DMTMM vs EDC/NHS for ligation of amines to Hyaluronan in water," *Carbohydr. Polym.*, vol. 108, no. 1, pp. 239–246, Aug. 2014, doi: 10.1016/j.carbpol.2014.02.070.

[115] S. A. Raw, "An improved process for the synthesis of DMTMM-based coupling reagents," *Tetrahedron Lett.*, vol. 50, no. 8, pp. 946–948, 2009, doi: 10.1016/j.tetlet.2008.12.047.

[116] F. J. Wende *et al.*, "1D NMR methods for determination of degree of cross-linking and BDDE substitution positions in HA hydrogels," *Carbohydr. Polym.*, vol. 157, no. November, pp. 1525–1530, 2017, doi: 10.1016/j.carbpol.2016.11.029.

[117] P. Farkaš and S. Bystrický, "Efficient activation of carboxyl polysaccharides for the preparation of conjugates," *Carbohydr. Polym.*, vol. 68, no. 1, pp. 187–190, Mar. 2007, doi: 10.1016/j.carbpol.2006.07.013.

[118] A. Veraldi *et al.*, "Fine structural characterization of sulodexide," *J. Pharm. Biomed. Anal.*, vol. 156, pp. 67–79, 2018, doi: 10.1016/j.jpba.2018.04.012.

[119] M. Mauri *et al.*, "Qualification of HSQC methods for quantitative composition of heparin and low molecular weight heparins," *J. Pharm. Biomed. Anal.*, vol. 136, pp. 92–105, 2017, doi: 10.1016/j.jpba.2016.12.031.

[120] S. Highsmith *et al.*, "Mechanism of action of bovine testicular hyaluronidase. Mapping of the active site," *J. Biol. Chem.*, vol. 250, no. 18, pp. 7473–7480, 1975, doi: 10.1016/s0021-9258(19)40968-x.

[121] I. Kakizaki *et al.*, "Mechanism for the hydrolysis of hyaluronan oligosaccharides by bovine testicular hyaluronidase," *FEBS J.*, vol. 277, no. 7, pp. 1776–1786, Apr. 2010, doi:

10.1111/j.1742-4658.2010.07600.x.

[122] L. C. Li *et al.*, "Functions of galectin-3 and its role in fibrotic diseases," *J. Pharmacol. Exp. Ther.*, vol. 351, no. 2, pp. 336–343, 2014, doi: 10.1124/jpet.114.218370.

[123] A. García-Abuín *et al.*, "Viscosimetric behaviour of hyaluronic acid in different aqueous solutions," *Carbohydr. Polym.*, vol. 85, no. 3, pp. 500–505, Jun. 2011, doi: 10.1016/j.carbpol.2011.02.028.

[124] L. Sindrewicz P., Li X., Yates E., Turnbull J., Lian L., Yu, "Intrinsic tryptophan fluorescence spectroscopy reliably determines galectin-ligand interactions," *Sci. Rep.*, vol. 9, no. 1, Dec. 2019, doi: 10.1038/s41598-019-47658-8.

[125] P. Sindrewicz *et al.*, "Interaction with the heparin-derived binding inhibitors destabilizes galectin-3 protein structure," *Biochem. Biophys. Res. Commun.*, vol. 523, no. 2, pp. 336–341, Mar. 2020, doi: 10.1016/j.bbrc.2019.12.054.

[126] P. Fayad *et al.*, "Hyaluronidase reaction kinetics evaluated by capillary electrophoresis with UV and high-resolution mass spectrometry (HRMS) detection," *Anal. Chim. Acta*, vol. 951, pp. 140–150, Jan. 2017, doi: 10.1016/j.aca.2016.11.036.

[127] M. Rodriguez *et al.*, "Thermodynamic Switch in Binding of Adhesion/Growth Regulatory Human Galectin-3 to Tumor-Associated TF Antigen (CD176) and MUC1 Glycopeptides," *Biochemistry*, vol. 54, no. 29, pp. 4462–4474, Jul. 2015, doi: 10.1021/acs.biochem.5b00555.

[128] C. Hsieh *et al.*, "Structural basis underlying the binding preference of human galectins-1, -3 and -7 for Galβ1-3/4GlcNAc," *PLoS One*, vol. 10, no. 5, May 2015, doi: 10.1371/journal.pone.0125946.

[129] A. Lepur *et al.*, "Ligand induced galectin-3 protein self-association," *J. Biol. Chem.*, vol. 287, no. 26, pp. 21751–21756, Jun. 2012, doi: 10.1074/jbc.C112.358002.

[130] N. Ahmad *et al.*, "Galectin-3 Precipitates as a Pentamer with Synthetic Multivalent Carbohydrates and Forms Heterogeneous Cross-linked Complexes," *J. Biol. Chem.*, vol. 279, no. 12, pp. 10841–10847, Mar. 2004, doi: 10.1074/jbc.M312834200.

[131] C. Ahmad *et al.*, "Thermodynamic binding studies of cell surface carbohydrate epitopes to galectins-1, -3, and -7: Evidence for differential binding specificities," *Can. J. Chem.*, vol. 80, no. 8, pp. 1096–1104, 2002, doi: 10.1139/v02-162.

[132] H. Leffler and S. H. Barondes, "Specificity of binding of three soluble rat lung lectins to substituted and unsubstituted mammalian β-galactosides," *J. Biol. Chem.*, vol. 261, no. 22, pp. 10119–10126, 1986, doi: 10.1016/s0021-9258(18)67499-x.

[133] K. Hirabayashi *et al.*, "Oligosaccharide specificity of galectins: A search by frontal affinity chromatography," *Biochim. Biophys. Acta - Gen. Subj.*, vol. 1572, no. 2–3, pp. 232–254, 2002, doi: 10.1016/S0304-4165(02)00311-2.

[134] J. M. Fox *et al.*, "CXCL4/Platelet Factor 4 is an agonist of CCR1 and drives human monocyte migration," *Sci. Rep.*, vol. 8, no. 1, pp. 1–15, 2018, doi: 10.1038/s41598-018-27710-9.

[135] T. F. Deuel, P. S. Keim, M. Farmer, and R. L. Heinrikson, "Amino acid sequence of human platelet factor 4," *Proc. Natl. Acad. Sci. U. S. A.*, vol. 74, no. 6, pp. 2256–2258, 1977, doi: 10.1073/pnas.74.6.2256.

[136] T. H. Nguyen *et al.*, "Characterization of the interaction between platelet factor 4 and homogeneous synthetic low molecular weight heparins," *J. Thromb. Haemost.*, vol. 18, no. 2, pp. 390–398, 2020, doi: 10.1111/jth.14657.

[137] S. Suvarna *et al.*, “Determinants of PF4 / heparin immunogenicity,” *Blood*, vol. 110, no. 13, pp. 4253–4260, 2007, doi: 10.1182/blood-2007-08-105098.The.

[138] Z. Q. Li *et al.*, “Defining a second epitope for heparin-induced thrombocytopenia/thrombosis antibodies using KKO, a murine HIT-like monoclonal antibody,” *Blood*, vol. 99, no. 4, pp. 1230–1236, 2002, doi: 10.1182/blood.V99.4.1230.

[139] I. Ahmed *et al.*, “Heparin induced thrombocytopenia: Diagnosis and management update,” *Postgrad. Med. J.*, vol. 83, no. 983, pp. 575–582, 2007, doi: 10.1136/pgmj.2007.059188.

[140] T. E. Warkentin and A. Greinacher, “Laboratory Testing for Heparin-Induced Thrombocytopenia and Vaccine-Induced Immune Thrombotic Thrombocytopenia Antibodies: A Narrative Review,” *Semin. Thromb. Hemost.*, vol. 49, no. 6, pp. 621–633, 2023, doi: 10.1055/s-0042-1758818.

[141] H. V. Scheller and P. Ulvskov, “Hemicelluloses,” *Annu. Rev. Plant Biol.*, vol. 61, pp. 263–289, 2010, doi: 10.1146/annurev-arplant-042809-112315.

[142] V. R. Anderson and C. M. Perry, “Pentosan Polysulfate,” *Drugs*, vol. 66, no. 6, pp. 821–835, 2006, doi: 10.2165/00003495-200666060-00006.

[143] A. van Ophoven *et al.*, “Efficacy of pentosan polysulfate for the treatment of interstitial cystitis/bladder pain syndrome: results of a systematic review of randomized controlled trials,” *Curr. Med. Res. Opin.*, vol. 35, no. 9, pp. 1495–1503, 2019, doi: 10.1080/03007995.2019.1586401.

[144] S. T. Olson and I. Björk, “Mechanism of action of heparin and heparin-like antithrombotics,” *Perspect. Drug Discov. Des.*, vol. 1, no. 3, pp. 479–501, 1994, doi: 10.1007/BF02171861.

[145] F. Zhang *et al.*, “Potential Anti-SARS-CoV-2 Activity of Pentosan Polysulfate and Mucopolysaccharide Polysulfate,” *Pharmaceuticals*, vol. 15, no. 2, pp. 1–13, 2022, doi: 10.3390/ph15020258.

[146] R. Krishnan *et al.*, “Anti-inflammatory actions of Pentosan polysulfate sodium in a mouse model of influenza virus A/PR8/34-induced pulmonary inflammation,” *Front. Immunol.*, vol. 14, no. February, pp. 1–15, 2023, doi: 10.3389/fimmu.2023.1030879.

[147] C. Sanden *et al.*, “Broad th2 neutralization and anti-inflammatory action of pentosan polysulfate sodiumin experimental allergic rhinitis,” *Immunity, Inflamm. Dis.*, vol. 5, no. 3, pp. 300–309, 2017, doi: 10.1002/iid3.164.

[148] D. Bratkovic *et al.*, “Open-label, single-center, clinical study evaluating the safety, tolerability and clinical effects of pentosan polysulfate sodium in subjects with mucopolysaccharidosis I,” *J. Inherit. Metab. Dis.*, vol. 47, no. 2, pp. 355–365, 2024, doi: 10.1002/jimd.12715.

[149] B. Tardy-poncet *et al.*, “Pentosan Polysulfate Induced Thrombocytopenia and Thrombosis,” vol. 257, pp. 252–257, 1994.

[150] A. Le Querrec *et al.*, “Pentosan polysulfate like heparin may induce severe thrombocitopenia,” *Thromb. Res.*, vol. Suppl. VI, p. 1986, 1986.

[151] R. M. Lush *et al.*, “A phase I study of pentosan polysulfate sodium in patients with advanced malignancies,” *Ann. Oncol.*, vol. 7, no. 9, pp. 939–944, 1996, doi: 10.1093/oxfordjournals.annonc.a010797.

[152] G. Follea, I. Tjian, and R. Streichenberger, “Pentosan polysulphate associated thrombocytopenia,” *Thromb. Res.*, vol. 42, pp. 413–418, 1986.

[153] L. Rice *et al.*, “Pentosan induced cerebral sagittal sinus thrombosis : a variant of heparin induced thrombocytopenia,” *J. Urol.*, vol. 160, no. 2148, p. 5347, 1998.

[154] B. Tardy-poncet *et al.*, “Pentosan polysulfate-Induced thrombocytopenia and thrombosis,” *Am. J. Hematol.*, vol. 45, pp. 252–257, 1994.

[155] E. K. Goad *et al.*, “Pentosan-induced thrombocytopenia : support for an immune complex mechanism,” *Br. J. Haematol.*, vol. 88, pp. 803–808, 1994.

[156] S. Brandt *et al.*, “Characterisation of the conformational changes in platelet factor 4 induced by polyanions: Towards in vitro prediction of antigenicity,” *Thromb. Haemost.*, vol. 112, no. 1, pp. 53–64, 2014, doi: 10.1160/TH13-08-0634.

[157] G. M. Arepally *et al.*, “Characterization of a murine monoclonal antibody that mimics heparin- induced thrombocytopenia antibodies,” *Blood*, vol. 95, no. 5, pp. 1533–1540, 2000, doi: 10.1182/blood.v95.5.1533.005k01_1533_1540.

[158] M. F. Scully *et al.*, “Anticoagulant and antiheparin activities of a pentosan polysulphate,” *Thromb. Res.*, vol. 31, no. 1, pp. 87–97, 1983, doi: 10.1016/0049-3848(83)90010-5.

[159] J. L. Marshall *et al.*, “Phase I trial of orally administered pentosan polysulfate in patients with advanced cancer,” *Clin. Cancer Res.*, vol. 3, no. 12 I, pp. 2347–2354, 1997.

[160] Y. Tsuboi *et al.*, “Continuous intraventricular infusion of pentosan polysulfate: Clinical trial against prion diseases: Symposium: Prion diseases - Updated,” *Neuropathology*, vol. 29, no. 5, pp. 632–636, 2009, doi: 10.1111/j.1440-1789.2009.01058.x.

[161] V. Venkitasubramony *et al.*, “Biological and Pharmacological Profiling of Pentosan Polysulfate (PPS) in Comparison to Heparin and its Relative Neutralization by Protamine Sulfate,” *FASEB J.*, vol. 34, no. S1, p. 1, 2020, doi: https://doi.org/10.1096/fasebj.2020.34.s1.04049.

[162] P. Möhnle *et al.*, “Anticoagulation in intensive care medicine,” *Medizinische Klin. - Intensivmed. und Notfallmedizin*, vol. 116, no. 6, pp. 499–507, 2021, doi: 10.1007/s00063-021-00849-6.

[163] M. M. Smith and J. Melrose, “Pentosan Polysulfate Affords Pleotropic Protection to Multiple Cells and Tissues,” *Pharmaceuticals*, vol. 16, no. 3, 2023, doi: 10.3390/ph16030437.

[164] “Drug Bank.” https: //www.drugbank.ca/drugs/DB00686.

[165] T. E. Warkentin *et al.*, “Anti-platelet factor 4/heparin antibodies in orthopedic surgery patients receiving antithrombotic prophylaxis with fondaparinux or enoxaparin,” *Blood*, vol. 106, no. 12, pp. 3791–3796, 2005, doi: 10.1182/blood-2005-05-1938.

[166] L. Xu *et al.*, “Lipid Nanoparticles for Drug Delivery,” *Adv. NanoBiomed Res.*, vol. 2, no. 2, 2022, doi: 10.1002/anbr.202100109.

[167] E. Musielak *et al.*, “Synthesis and Potential Applications of Lipid Nanoparticles in Medicine,” *Materials (Basel).*, vol. 15, no. 2, 2022, doi: 10.3390/ma15020682.

[168] E. Kon *et al.*, “Targeting cancer with mRNA–lipid nanoparticles: key considerations and future prospects,” *Nat. Rev. Clin. Oncol.*, vol. 20, no. 11, pp. 739–754, 2023, doi: 10.1038/s41571-023-00811-9.

[169] B. Tafech *et al.*, “Surface modification of lipid nanoparticles for gene therapy,” *J. Gene Med.*, vol. 26, no. 1, 2024, doi: 10.1002/jgm.3642.

[170] M. Chen *et al.*, “Liposome-based delivery systems in plant polysaccharides,” *J. Nanomater.*, vol. 2012, 2012, doi: 10.1155/2012/682545.

[171] R. Bo *et al.*, “Optimization on conditions of Lycium barbarum polysaccharides liposome by RSM and its effects on the peritoneal macrophages function,” *Carbohydr. Polym.*, vol. 117, pp. 215–222, 2015, doi: 10.1016/j.carbpol.2014.09.060.

[172] G. Górski *et al.*, “Liposomal heparin spray: A new formula in adjunctive treatment of superficial venous thrombosis,” *Angiology*, vol. 56, no. 1, pp. 9–17, 2005, doi: 10.1177/000331970505600102.

[173] B. Shuhua, V. Gupta, and F. Ahsan, “Cationic Liposomes as Carriers for Aerosolized Formulations of an Anionic Drug:Safety and Efficacy Study,” *Eur. J. Pharm. Sci.*, vol. 38, no. 2, pp. 165–171, 2009, doi: 10.1016/j.ejps.2009.07.002.Cationic.

[174] B. Shuhua and F. Ahsan, “Inhalable Liposomes of Low Molecular Weight Heparin for the Treatment of Venous Thromboembolism,” *J. Pharm. Sci.*, vol. 99, no. 11, pp. 4554-, 2010, doi: 10.1002/jps.

[175] L. Pandolfi *et al.*, “Liposomes loaded with everolimus and coated with hyaluronic acid: A promising approach for lung fibrosis,” *International Journal of Molecular Sciences*, vol. 22, no. 14. 2021, doi: 10.3390/ijms22147743.

[176] H. Xing *et al.*, “High molecular weight hyaluronic acid-liposome delivery system for efficient transdermal treatment of acute and chronic skin photodamage,” *Acta Biomater.*, vol. 182, pp. 171–187, 2024, doi: 10.1016/j.actbio.2024.05.026.

[177] C. Ni*, et al*., “Hyaluronic acid and HA-modified cationic liposomes for promoting skin penetration and retention,” *J. Control. Release*, vol. 357, no. March, pp. 432–443, 2023, doi: 10.1016/j.jconrel.2023.03.049.

[178] M. L. Vázquez-González *et al*.,“Enhanced topical delivery of hyaluronic acid encapsulated in liposomes: A surface-dependent phenomenon,” *Colloids Surfaces B Biointerfaces*, vol. 134, pp. 31–39, 2015, doi: 10.1016/j.colsurfb.2015.06.029.

[179] Y. Eygeris *et al*, “Chemistry of Lipid Nanoparticles for RNA Delivery,” *Acc. Chem. Res.*, vol. 55, no. 1, pp. 2–12, 2022, doi: 10.1021/acs.accounts.1c00544.

[180] C. Hald Albertsen *et al.*, “The role of lipid components in lipid nanoparticles for vaccines and gene therapy,” *Adv. Drug Deliv. Rev.*, vol. 188, p. 114416, 2022, doi: 10.1016/j.addr.2022.114416.

[181] G. B. Schober, *et al.*, “A careful look at lipid nanoparticle characterization: analysis of benchmark formulations for encapsulation of RNA cargo size gradient,” *Sci. Rep.*, vol. 14, no. 1, pp. 1–10, 2024, doi: 10.1038/s41598-024-52685-1.

[182] S. C. Semple *et al.*, “Rational design of cationic lipids for siRNA delivery,” *Nat. Biotechnol.*, vol. 28, no. 2, pp. 172–176, 2010, doi: 10.1038/nbt.1602.

[183] Y. Liu *et al.*, “Development of mRNA Lipid Nanoparticles: Targeting and Therapeutic Aspects,” *Int. J. Mol. Sci.*, vol. 25, no. 18, 2024, doi: 10.3390/ijms251810166.

[184] M. Maeki *et al.*, “Understanding the formation mechanism of lipid nanoparticles in microfluidic devices with chaotic micromixers,” *PLoS One*, vol. 12, no. 11, pp. 1–16, 2017, doi: 10.1371/journal.pone.0187962.

[185] C. Malburet *et al.*, “Size and Charge Characterization of Lipid Nanoparticles for mRNA Vaccines,” *Anal. Chem.*, vol. 94, no. 11, pp. 4677–4685, 2022, doi: 10.1021/acs.analchem.1c04778.

[186] Alnylam, “ONPATTRO (patisiran) (patisiran) | Treatment for Polyneuropathy of hATTR amyloidosis,” 2018. https://www.onpattro.com/.

[187] M. Garcia-Fuentes *et al.*, “Application of NMR Spectroscopy to the Characterization of

PEG-Stabilized Lipid Nanoparticles," *Langmuir*, vol. 20, no. 20, pp. 8839–8845, 2004, doi: 10.1021/la049505j.

[188] M. M. Wang *et al.*, "Elucidation of lipid nanoparticle surface structure in mRNA vaccines," *Sci. Rep.*, vol. 13, no. 1, pp. 1–8, 2023, doi: 10.1038/s41598-023-43898-x.

[189] L. J. Kricka, Ed., *Nonisotopic DNA probe techniques*. Academic Press, 1992.